Dissertation

submitted to the
Combined Faculties for the Natural Sciences and for Mathematics
of the Ruperto-Carola University of Heidelberg, Germany
for the degree of
Doctor of Natural Sciences

Put forward by
Diplom-Physikerin: Veronika Judith Mueller
born in Saarbrücken

Oral examination: July 11th, 2012

Nanoscale studies of membrane dynamics via STED – Fluorescence Correlation Spectroscopy

Referees: Prof. Dr. Dr. h.c. Stefan W. Hell
Prof. Dr. Rainer Fink

Zusammenfassung

Molekularen Dynamiken innerhalb der lebenden Zelle sind wegen der begrenzten räumlichen Auflösung der konventionellen Lichtmikroskopie oft nur schwer zu beobachten. Die erhöhte Auflösung der STED Nanoskopie gewährt uns dagegen neue Einblicke in die dynamischen Vorgänge in der Plasmamembran. In Kombination mit der hohen zeitlichen Auflösung der Fluoreszenz-Korrelations-Spektroskopie (FCS) können wir so die Diffusion von Lipiden und Proteinen auf kleinsten Längenskalen bestimmen und ihre dynamischen Eigenschaften charakterisieren.

Im ersten Teil der Arbeit vergleichen wir mit Hilfe von STED-FCS die Diffusionsdynamiken verschiedener Fluoreszenz-markierter Lipide und Proteine. Unsere Messungen in lebendenen Zellen zeigen, dass die Dynamik innerhalb der Plasmamembran verschiedenen Diffusionsgesetzen folgt. Diese können anhand der chemischen Struktur der Lipide in verschiedene Klassen unterteilt werden. Während Phosphoglycerolipide nur schwach innerhalb der Membran wechselwirken, gehen Sphingolipide vorübergehende Bindungen mit anderen Membranbestandteilen ein und werden so in ihrer freien Diffusion gehindert. Die Dynamik von Membranproteine dagegen ist durch das Zytoskelett der Zelle begrenzt. Wir unterlegen und erklären diese experimentellen Ergebnisse mit Hilfe von Monte Carlo Simulationen.

Im zweiten Teil der Arbeit erweitern wir den STED-FCS Aufbau um einen schnellen Strahlscanner mit dem der Laserstrahl die Probe abtasten kann. Dieses neuartige Verfahren ermöglicht uns nicht nur eine kalibrationsfreie Messung von langsam diffundierenden Membranproteinen, sondern erlaubt es uns auch, die inhomogene Verteilung der Diffusionsdynmaik direkt darzustellen.

Abstract

Molecular membrane dynamics in living cells are often obscured from the observer because of the limited spatial resolution of conventional far-field optical microscopy. The superior spatial resolution of stimulated emission depletion (STED) nanoscopy provides new insights into the dynamic processes within the plasma membrane. In combination with the high temporal resolution of fluorescence correlation spectroscopy (FCS), we record and characterize the diffusion of membrane constituents within nanoscale observation areas.

In the first part of the thesis, we compare STED-FCS data of various fluorescent lipid analogs and proteins in the plasma membrane of living cells. Our results reveal distinct modes of diffusion which can be differentiated according to the chemical structure of the molecules. Phosphoglycerolipids diffuse freely and only weakly interact with other membrane constituents. Sphingolipids exhibit a strong molecular confinement due to the formation of hydrogen bounds within the ceramide backbone or between large polar head groups. Transmembrane proteins corral in compartments built by the cellular cytoskeleton. We implement Monte-Carlo simulations to support and explain our experimental results.

In the second part of the thesis, we enhance the experimental STED-FCS setup by the integration of a fast scanning unit. This newly developed concept not only enables us to perform calibration-free measurements of slowly diffusing particles but also visualizes spatial diffusion heterogeneities along the scan trajectory.

Contents

We have to remember that
what we observe is not nature herself,
but nature exposed to our method of questioning.

Werner Heisenberg

Motivation

The cycle of life within a cell - how it emerges, evolves and maintains itself in ever-changing environments - is one of the most fascinating phenomena in natural science. While in physics the state and evolution of a system is entirely described by the prevalent interactions due to a set of fundamental forces, the complex processes within the living cell are difficult to predict from an individual consideration of the physical reactions of each cellular component. An isolated protein, for example, acts very differently in a model system than from within the natural entity of the cell. In order to understand the origins and mechanisms of any natural process, it is therefore essential to study them within their natural and undisturbed environment.

One of the best available methods to directly observe processes within a living cell is fluorescence microscopy. In fluorescence microscopy, the structure of interest is specifically labeled by a fluorescent dye and visualized by excitation and subsequent detection of the fluorescence signal. Being minimally invasive, fluorescence microscopy may be directly applied to image a living system and further allows to sensitively detect even single molecules. Yet, the spatial resolution of conventional fluorescence microscopy is fundamentally limited by diffraction. As expressed in the diffraction law by Ernst Abbe in 1873, two structures can only be resolved if they are separated by more than half the wavelength of the excitation light in use[1].

For nearly a century, the diffraction barrier was widely accepted to universally limit any kind of far-field light microscopy. It was not until 1994, that Stefan W. Hell and coworkers realized that the diffraction barrier is in fact not fundamental but can be broken by exploiting the physical properties of the fluorescent dye [2]. If we are able to effectively control the fluorescent state of the dye - switching it between a non-fluorescent off-state and an emitting on-state - we can discriminate two adjacent fluorophores by observing them sequentially in time. This basic principle of detecting the fluorescence signal only from a single emitting fluorophore, while keeping all surrounding fluorophores dark, gave rise to the development of a number of superresolution techniques which are generally divided in two major types [3]. While the first introduced concepts such as STED, RESOLFT and SSIM follow a deterministic illumination pattern to target a well-defined coordinate capable of emitting fluorescence [4, 5, 6], the stochastical methods such as PALM or STORM precisely localize the coordinate of a subset of randomly activated single fluorophores. Consecutive activation and localization of the complete set of fluorophores allows for the reconstruction

of the entire spatial distribution of fluorophores [7, 8, 9]. In recent years, these newly invented nanoscopy techniques have been widely applied to a variety of biological systems. With spatial resolutions down to 10-50 nm, these methods have answered fundamental biological questions ranging from the transport and exocytosis of synaptic vesicles to the elucidation of the three-dimensional composition of cellular structures such as focal-adhesions or chemical synapses in dendritic spines [10, 11, 12, 13]

The precise visualization of the cell down to the molecular level, however, only provides us with a snapshot of the complex interplay within a living system. For a complete understanding of dynamic cellular activities, it is equally important to record biological phenomena with a high spatial as well as temporal resolution. In stochastical superresolution concepts, the temporal resolution is governed by the switching kinetics of the fluorophores during the successive activation and localization cycles. Up to now, fast-switching probes in STORM microscopy allow image acquisition as fast as 1-2 images per second [14]. A STED nanoscope, in contrast, may be readily combined with conventional fast scanning microscope techniques. Collecting STED-images at video-rate and beyond has allowed for the precise tracking of synaptic vesicle movement along the axons of a living neuron as well as the visualization of the structural assembly of a colloidal-crystal [11, 15]. While video-rate imaging covers a wide range of dynamic applications, it however fails to report on fast kinetics in the millisecond range and below. In this work, we therefore employ fluorescence correlation spectroscopy to complement the high spatial resolution of STED with a microsecond temporal resolution. As recently developed, STED-FCS uniquely allows us to observe the heterogeneous diffusion characteristics of fluorescently labeled particles within the plasma membrane of the living cell [16]. Studying the nanoscale diffusion of various membrane lipids and proteins, we are able to identify the origins of the heterogeneous organization within the membrane and gain valuable insights into the complex interplay between specific lipids and proteins. Extending STED-FCS by scanning the observation area rapidly across the sample plane, not only improves the statistical accuracy and calibration of the experiment, but also provides us with additional spatial information elucidating the inhomogeneous distribution of membrane dynamics.

The first part of this thesis is concerned with the application of STED-FCS to record membrane dynamics on the nanoscale. After an introduction of the general organization of the plasma membrane and an overview over the currently available experimental techniques in **chapter** 1, we discuss the biological preparation and labeling procedures as well as an overview of the experimental setup in **chapter** 2. In **chapter** 3, we apply the concept of STED-FCS to measure and characterize the nanoscale diffusion dynamics of lipids and identify putative factors constraining the free diffusion within the plasma membrane. In **chapter** 4, we study the nanoscale dynamics of the most common types of membrane proteins and investigate the role of post-translational lipid-modification on their diffusion behavior. The implementation of a specific Monte-Carlo algorithm in **chapter** 5 allows us to compare the observed experimental results

to the underlying principles of diffusion and theoretical constraints.

The second part of this thesis extends the conventional STED-FCS experiment by the incorporation of a fast laser beam scanning unit. After a brief introduction in **chapter** 7, we discuss the experimental modifications of the microscope system and introduce the key steps in the required data processing and analysis in **chapter** 8. The newly developed concept of the scanning STED-FCS technique is characterized in **chapter** 9 and applied to visualize the spatial inhomogeneities of lipid dynamics within the model membranes as well as the plasma membrane of the living cell.

Part I.

STED-FCS reveals membrane dynamics at the nanoscale

1. Introduction

Over the last decade, the field of membrane research has engaged into a vivid discussion about the organization and function of the plasma membrane [17]. In this chapter, we present an overview of the plasma membrane and introduce the most commonly discussed models for membrane organization and dynamics. We further describe how the diffusion of molecules within the membrane can be measured using Fluorescence Correlation Spectroscopy (FCS) and explain the potential of stimulated emission depletion (STED) to directly access diffusion dynamics on small length scales beyond the diffraction limit.

1.1. The plasma membrane

The plasma membrane is one of the most important components of the living cell. It defines the outer boundary of the cell and separates the intracellular matrix from the extracellular environment. This distinct compartmentalization allows the cell to create and maintain a transmembrane gradient of for instance polar molecules or charged ions [18]. The plasma membrane can, however, not be merely pictured as a passive impermeable barrier but rather provides a unique platform for a variety of cellular functions and processes. The integration of specific proteins within the membrane for instance allows the formation of channels which actively control what enters and exits the cell. Membrane proteins further play a crucial role in the reception and transduction of intra- and extracellular signals and carry out numerous enzymatic activities which enable the cell to spatially confine chemical reactions in close proximity to the plasma membrane [19].

In order to fully understand the complex functionality of the plasma membrane, we have to carefully consider its molecular composition in closer detail. As shown in figure 1.1, the basic structure of the plasma membrane consists of a lipid bilayer containing a variety of different lipids and proteins [20]. The lipids within the membrane are in general classified into four different species: phosphoglycerides, sphingolipids, glycolipids and sterols [21].

As schematically described in figure 1.2, the chemical structure of phosphoglycerides is based on a glycerol compound which is esterified on one side to two lipophilic

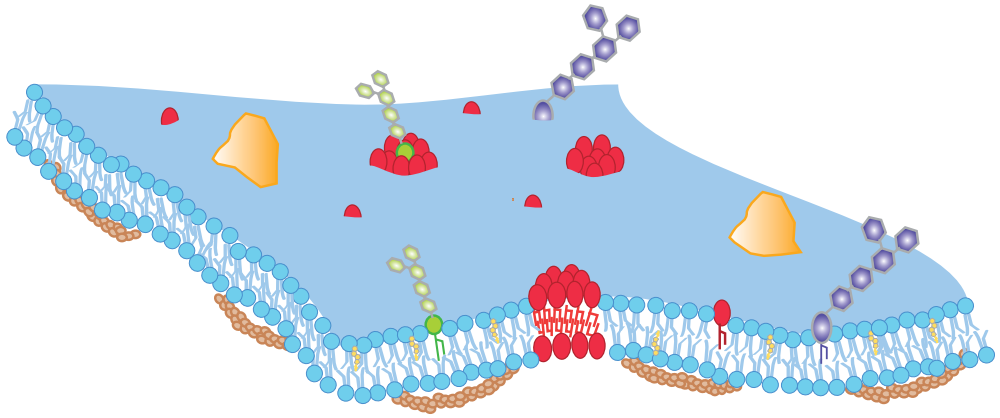

Figure 1.1.: Schematic overview of the plasma membrane separating the intracellular cytosol from the extracellular matrix: Formed by a lipid bilayer the plasma membrane contains a variety of different lipids and proteins. The fluid structure of the plasma membrane is further supported by the intracellular cytoskeleton of the cell.

fatty acid chains and at the other side to a phosphate molecule which carries a specific hydrophilic head group. Within the plasma membrane, the most abundant head groups are cholin and ethanolamine as found in phosphatidylcholine and phosphatidylethanolamine, respectively. In general, the hydrophilic head group determines the charge of the phosphoglyceride. At physiological pH the phosphate group of the lipid is deprotonated and therefore negatively charged. A positive charge in the head group as found in ethanolamine and choline thus leads to an overall neutral charge while a neutral molecule as for instance inositol results in a negatively charged lipid. Apart from their specific head group, phosphoglycerides are further characterized by their lipophilic hydrocarbon chains which can vary in length and degree of saturation. Typically, the length of the acyl chains is in the range of 12-26 carbon atoms and each chain can hold up to six double bounds [18].

Sphingolipids, the second major class of membrane lipids, are based on a ceramide backbone which is formed by a sphingosine molecule. This long-chain amino alcohol is esterified to an acyl chain and a polar head group as shown in figure 1.2. In this figure, we directly note that the ceramide backbone provides both a hydrogen donor in the hydroxyl-group as well as a hydrogen acceptor in the carboxyl-group whereas the previously discussed glycerol backbone only possess a single hydrogen acceptor (carboxyl-group)[22]. In contrast to phosphoglycerides, sphingolipids are typically found to carry longer and fully saturated fatty acid chains with 16-26 carbons. The most common sphingolipid within the plasma membrane is sphingomyelin with its characteristic choline head group. A further important group of sphingolipids are gangliosides such as GM1, GM2 and GM3. These gangliosides carry large polar head groups containing multiple carbohydrates. Because of these saccharidic head groups,

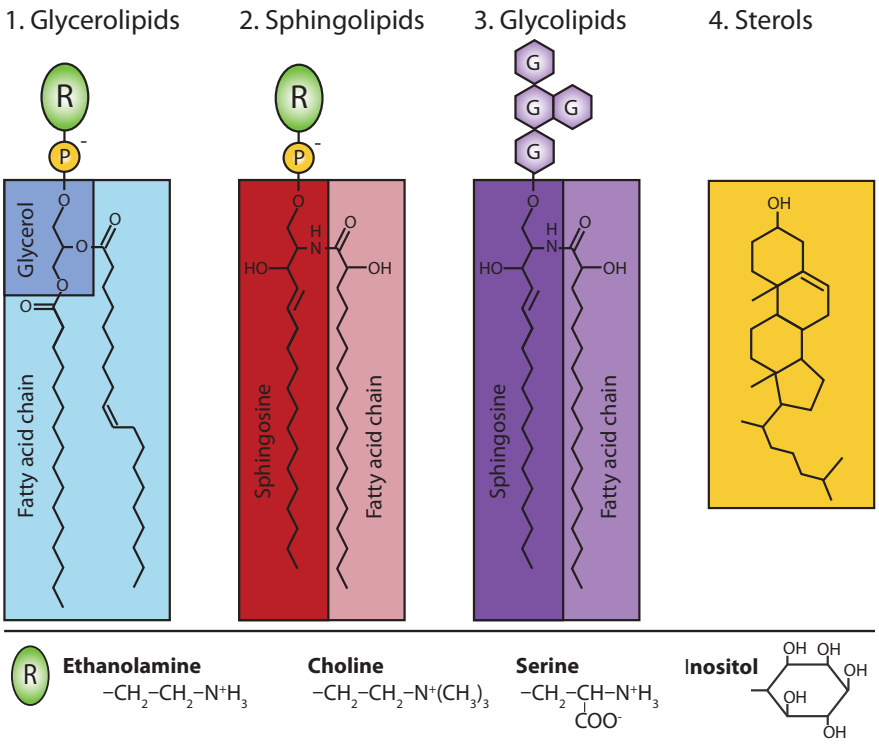

Figure 1.2.: Chemical structures of membrane lipids: (1) Glycerolipids are based on a glycerol backbone linking two often unsaturated fatty acid chains to a phosphatidic head group (R). (2) Sphingolipids are based on a sphingosine backbone linked to saturated fatty acid chains. (3) Glycolipids are based on either sphingosine (shown here) or glycerol backbones and are characterized by large saccharidic head groups. (4) Sterols are formed by multiple ring-structures with a characteristic planar geometry. At the lower bottom, the chemical structures of the most abundant head groups within the plasma membrane are shown.

gangliosides can also be classified into the third group of membrane lipids, the so-called glycolipids.

Glycolipids are either based on a glycerol or a ceramide structure but always feature a characteristic carbohydrate head group. The size of the head group varies from a single sugar residue to complex oligosaccharide. Glycolipids are exclusively found on the outer leaflet of the plasma membrane and are known to play a crucial role in cellular recognition and the immune response of the cell.

The fourth group of membrane lipids, the sterols, are formed by a rigid two-dimensional steroid nucleus of four fused hydrocarbon rings. Cholesterol is the most common sterol in the plasma membrane and typically accounts for approximately 20% of the membrane lipids. Because of its short and rigid structure, cholesterol is prone to intercalate

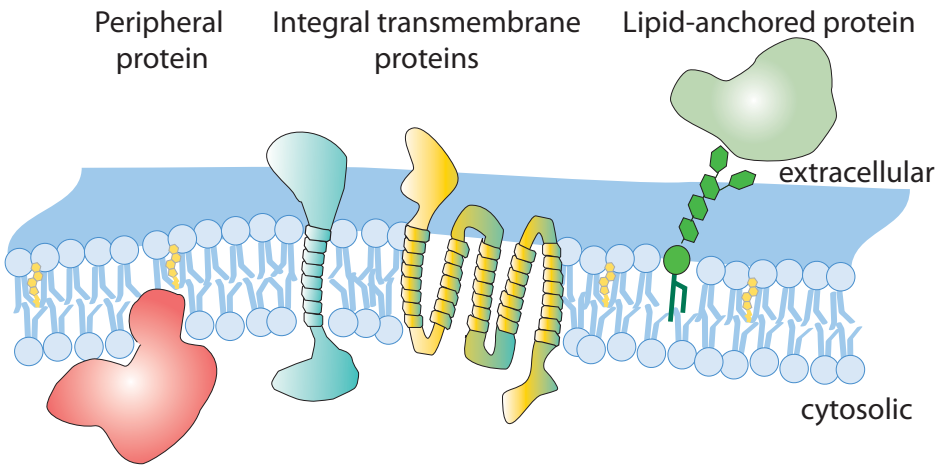

Figure 1.3.: Three major classes of membrane proteins (from left to right): Peripheral proteins are partly embedded within the plasma membrane, whereas integral transmembrane proteins fully span the membrane with a single or multiple helices. Lipid-anchored proteins are associated to the membrane by a lipid-anchor as for instance the GPI-anchor.

between the gaps between unsaturated phosphoglycerides and thus increases the rigidity of the plasma membrane. Cholesterol is further known to possess a high affinity to the ceramide structure of sphingolipids due to the formation of mutual hydrogen bounds.

Next to lipids, the second major constituents of the plasma membrane are proteins which are responsible for a majority of the membrane functions and processes [23]. As depicted in figure 1.3, one distinguishes peripheral, transmembrane and lipid-anchored proteins. While peripheral proteins are only partly embedded into a single leaflet of the membrane, transmembrane proteins fully span the membrane with a single or multiple hydrophobic helices. Examples for these transmembrane proteins are ion channels or transporters, receptors as well as membrane anchors which are attach to the extra- or intracellular matrix. The third class of membrane proteins, the lipid-linked proteins, are not integrated into the membrane but covalently bound to specific membrane lipids generally referred to as lipid anchors. One of the most common lipid anchors found exclusively in the outer leaflet of the plasma membrane is glycosylphosphatidylinositol (GPI) with its characteristic oligosaccharide based head group [19].

Finally, we note that the general structure of the plasma membrane is additionally stabilized by a complex meshwork, the cytoskeleton of the cell. Numerous membrane lipids and proteins are found to directly interact with for instance the actin filaments of the cell which run directly beneath the membrane. As the cytoskeleton is constantly polymerized and depolymerized, it is generally believed to play a crucial role in cell mobility and migration [20].

1.2. Membrane organization and dynamics

The structure and composition of the plasma membrane was well characterized early on using electron micrographs, mass spectroscopy and detergent solutions. Nevertheless, the organization and dynamics of the specific constituents within the membrane have proven to be exceptionally challenging to observe [24, 25].

In 1972, Singer and Nicolson proposed that the plasma membrane forms a two-dimensional liquid through which lipids and membrane proteins can diffuse freely and randomly according to the principles of Brownian motion [26]. In this so-called fluid mosaic model, the lipids within the membrane are considered to act as a passive solvent for membrane proteins and are therefore expected to be homogeneously distributed across the entire membrane. Surprisingly, first experiments in 1988, however, revealed a heterogeneous distribution of lipids in epithelia cells [27]. In these experiments, it was found that the apical membrane of epithelia cells is enriched in glycosphingolipids while phosphoglycerides were predominantly found in the basolateral membrane. The origin of this lateral asymmetry could only be explained by an intrinsic intermolecular affinity of sphingolipids and cholesterol, which leads to the formation of tightly packed clusters in the exoplasmic leaflet of the Golgi membrane. These domains were proposed to serve as sorting centers for proteins that are eventually targeted to the apical membrane [28]. A close investigation of the discovered membrane clusters showed that they remained insoluble upon detergent extraction, forming so-called detergent resistant membrane complexes, but only arose in the presence of cholesterol [28, 29]. Combining these observations finally led to the postulation of the "raft concept" assuming the preferential packing of sphingolipids and cholesterol to build lipid nanodomains [30]. These so-called lipid rafts are believed to float through the plasma membrane and to serve as a platform for specific proteins (see figure 1.4) [31]. As lipid rafts are proposed to assemble and disassemble dynamically, they are expected to play a crucial role in membrane trafficking and cell-signaling [32, 33, 34]. Soon after the proposal of the "raft concept", a vivid discussion arose around the existence and functionality of the lipid rafts [17, 24, 35, 36]. Considering that lipid rafts are predicted to be both extremely small (< 200 nm) and at the same time highly dynamic, conventional light microscopy techniques fail to visualize their formation or presence within the plasma membrane [33]. Hence, much of the debate in this rapidly emerging research field was due to the lack of suitable experimental methods to directly observe lipid rafts within the natural membrane of the living cell [31].

In parallel to the development of the "raft concept", single particle tracking techniques were used to record the trajectories of transmembrane proteins tagged with colloidal gold particles [37]. Statistical analysis of the recorded trajectories revealed that the observed proteins diffuse freely within a confined compartment of around 60 nm in

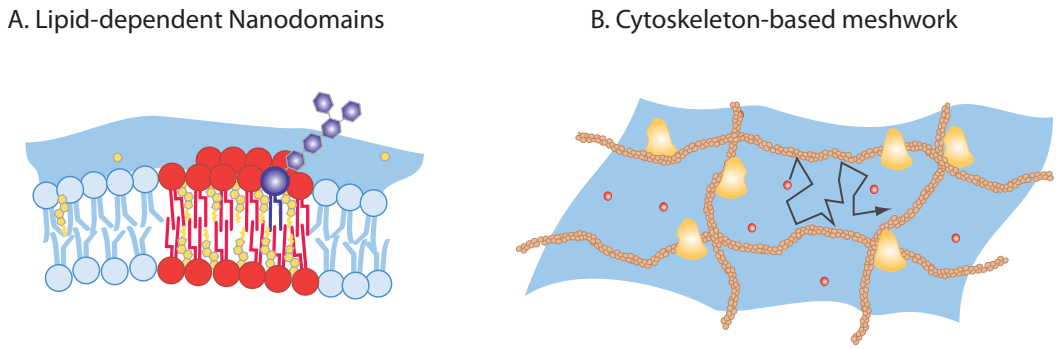

Figure 1.4.: Two models explain the heterogeneous organization of the plasma membrane: (A) Lipid-dependent nanodomains built nanosized platforms and are enriched in sphingolipids (red, purple) and cholesterol (yellow). (B) The cytoskeleton of the cell acts as a barrier for the otherwise free diffusion of lipids and proteins.

diameter. In the course of the observation, each proteins was reported to jump into an adjacent compartment after an average confinement time of about 2 ms. These observation gave rise to the model of hop diffusion assuming the actin-based cytoskeleton of the cell to act as a barrier for the otherwise free diffusion of proteins (see figure 1.4). In particular, the cytoplasmic fraction of transmembrane proteins is believed to collide and interact with the underlying cytoskeleton. Interestingly, subsequent single particle tracking experiments involving membrane lipids showed that phosphoglycerides tagged with colloid gold particle experience the same hop-like diffusion within the membrane [38, 39]. Even though these lipids were integrated into the outer leaflet of the plasma membrane, their diffusion appeared to be influenced indirectly by the intracellular cytoskeleton. It was therefore proposed that specific transmembrane proteins are anchored along the cytoskeleton similar to pickets in a fence. This dense meshwork of pickets forms not only a physical obstacle for transmembrane proteins but also induces hydrodynamic frictions which effectively slow down the diffusion of the surrounding lipids [40, 41, 42].

1.3. Experimental observation of membrane dynamics

In order to experimentally prove the existence of either lipid rafts or cytoskeleton-based barriers a wide range of different techniques have been applied to study the heterogeneity within the plasma membrane [43, 44].

The identification of raft associated lipids and proteins was initially based on the analysis of insoluble membrane complexes which are resistant to detergent extraction [45, 46]. Yet, detergent extraction soon proved to be unreliable as the structure of the membrane is disrupted by detergent treatment and the obtained results varied

considerably for different detergents and extraction protocols [47, 48]. Early attempts to visualize membrane partitioning by conventional light microscopy using fluorescent proteins or lipid analogs failed to consistently observe the heterogeneous organization of the plasma membrane [49, 50]. These experiments, however, confirmed the assumption that the size of both lipid rafts as well as cytoskeleton-induced compartments is on the order of 10-100 nm and can therefore not be resolved with diffraction-limited light microscopy techniques.

Exploiting the high sensitivity of single molecule techniques the dynamics and interactions of several membrane proteins were investigated. First results of fluorescence recovery after photobleaching (FRAP) or Förster resonance energy transfer (FRET) experiments did not show unambiguously that specific membrane proteins associate to raft-like nanodomains [51, 52]. Subsequent studies using homo-FRET indicated that GPI anchored proteins assemble to nanoscale cholesterol-mediated clusters [53]. These findings were supported by single particle tracking experiments which showed that quantum dot tagged GPI anchored proteins were integrated dynamically into GM1 enriched clusters [54].

Even though single particle techniques provide valuable evidence about lipid rafts, they also suffer from various experimental drawbacks. FRET experiments for instance only monitor the close interaction between acceptor and donor molecules and do not allow conclusions about long-range dynamics [25]. Single particle tracking methods, in contrast, usually rely on the use of bulky labels such as colloid gold particles and are further limited to a specific spatial or temporal regime [43]. An alternative single molecule approach is offered by Fluorescence Correlation Spectroscopy (FCS) which has recently been successfully applied to investigate membrane dynamics in model membranes as well as living cells [55, 56, 57].

1.3.1. Fluorescence correlation spectroscopy (FCS)

The fundamental principle of fluorescence correlation spectroscopy (FCS) is based on the analysis of fluctuations in a signal caused by local variations in the intrinsic properties of the system. While these fluctuations are an unintentional source of noise in a macroscopic system, they contain valuable information about the physical properties of a microscopic system [58]. First introduced by Magde and coworkers in 1972, FCS exploits the temporal fluctuations in fluorescence signals to deduce variations in the number of particles within the observation volume due to, for instance, diffusion or chemical reactions [59].

A conventional FCS experiment is depicted in figure 1.5. First, the lipid of interest is labeled with a fluorescent dye and introduced into the plasma membrane of a living cell via the formation of a BSA complex. An excitation laser is then focused onto

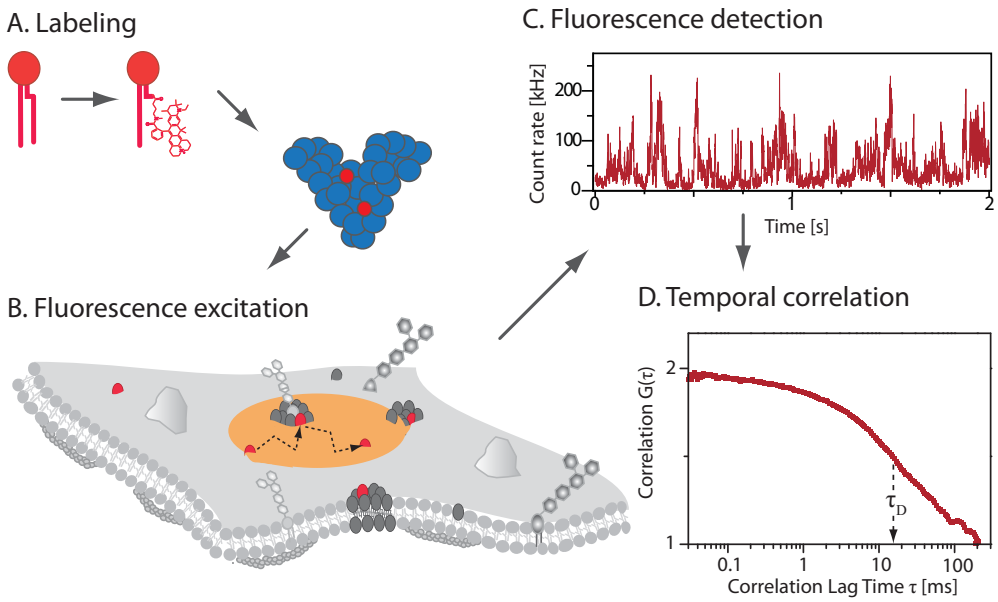

Figure 1.5.: A conventional FCS experiments to observe membrane dynamics: (A) The lipid of interest is labeled with a lipophilic dye and incorporated in the plasma membrane of a living cell via the formation of a BSA complex. (B) Fluorescent lipid analogs are illuminated with an excitation laser and the emitted fluorescence is recorded over time (C). (D) A temporal correlation of the intensity trace yields the correlation curve $G(\tau)$ and allows to derive the average number of particles within the observation area and the diffusion time τ_D.

the plasma membrane where it excites the fluorophores as they diffuse through the focus. Following the excitation, the emitted fluorescence is detected and recorded as a function of time. The obtained fluorescence intensity fluctuates around an average fluorescence intensity $\langle F \rangle$, which is directly proportional to the average number of particles N inside the observation volume [60, 61]. The fluctuations around the average value are often caused by the diffusion of the fluorescent particles through the observation area. When a particle, for example, enters the observation area, we observe a burst in the fluorescence intensity. While the amplitude of the burst is proportional to the molecular brightness of the particle, its width directly reflects the time the particle needs to traverse the observation volume. The average transient time is generally defined as the diffusion time $\tau_D = w_0^2/4D$, where w_0 denotes the lateral beam waist of the excitation laser at the focal spot and D refers to the particle's diffusion coefficient.

In order to assess the temporal fluctuations statistically, the measured fluorescence signal is correlated over time. Intuitively, the temporal correlation compares the fluorescence signal at time t to the signal at the delayed time $t + \tau$. For short lag times

($\tau < \tau_D$), a particle found in the observation volume at time t, is likely to still reside within the observation volume at the time $t + \tau$. Thus, the fluorescence intensity is predicted to be comparable at both times. For long lag times ($\tau > \tau_D$), the fluorescence intensity is on average not related to the signal at time t because the diffusion process for each particle is statistically independent from all the other particles. Consequently, the time scale over which the signal is correlated is directly related to the diffusion time τ_D.

A typical temporal autocorrelation curve as shown in figure 1.5 directly provides us with an estimation of τ_D given by the time at which the correlation has dropped to half its initial amplitude $G(0)$. We may also infer the the average number of particles N inside the observation volume which is inversely proportional to the initial correlation amplitude $G(0) \propto 1/N$.

Early attempts, to measure membrane dynamics using FCS were challenging due to various experimental constraints such as an efficient photon collection, stable focus positioning and specific labeling techniques [62]. Most of these systematic problems could be overcome with time and FCS was eventually successfully applied to study membrane dynamics in model membranes and living cells [63, 57, 64]. Implementing several technical variations of FCS further provided additional insight into the complexity of membrane organization. The simultaneous detection of two distinctly labeled species, for instance, was used to determine interaction between membrane components using fluorescence cross-correlation spectroscopy [65]. Two-focus FCS as well as scanning FCS techniques have further improved the experimental accuracy of the measured diffusion coefficients and extended the accessible temporal range by effectively reducing photo-physical artifacts [66, 67, 68, 69, 70].

1.3.2. FCS diffusion law

The previously discussed FCS techniques share the experimental drawback that the diffusion behavior of a particle is solely evaluated in terms of the observed transient times, but conceals putative constraints confining the free diffusion of a particle. If a particle is, for instance, repeatedly trapped within a nanodomain on its transit through the observation area, a conventional FCS experiment only detects an on average increase in the transient time.

In order to resolve the underlying diffusion modalities, it was therefore proposed to record the transient time for several sizes of the observation area in the range of $w_0 = 200 - 400$nm [71]. Plotting the transient time as a function of the observation area w_0^2 in the so-called FCS diffusion law indirectly allows us to infer the diffusion characteristics of a particle (see figure 1.6). For a freely diffusing species, the transient time of the particle directly corresponds to the diffusion time $\tau_D = w_0^2/4D$ and is thus

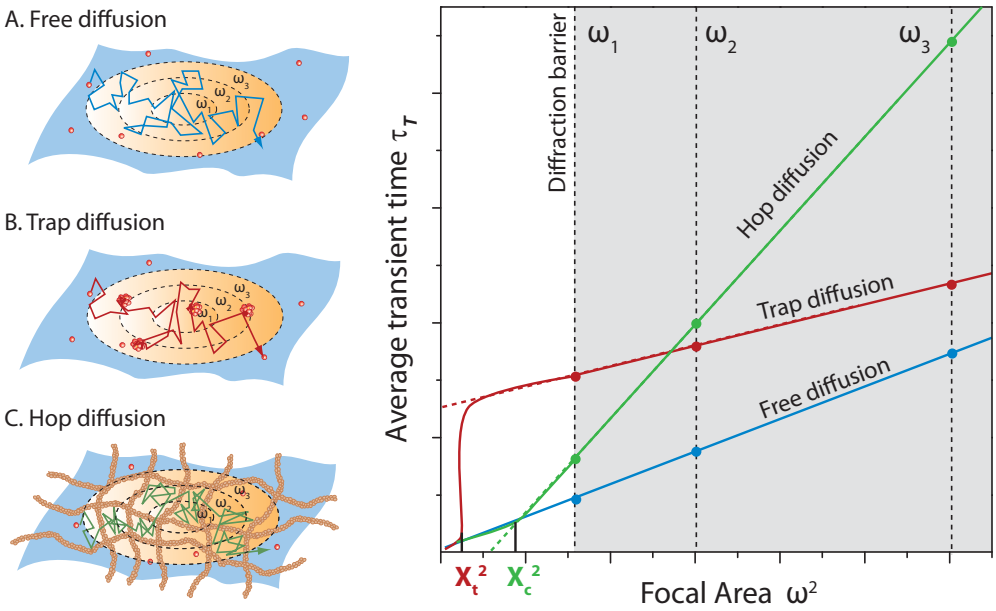

Figure 1.6.: FCS diffusion law: varying the size of the focal area ω, the average transient time is measured as a function of the focal area ω^2. (A) For a freely diffusing particle, the diffusion time decreases linearly with the size of the focal area (blue). (B) For a particle which is transiently trapped, the slope is less steep (red), whereas for a particle confined within the barriers of a meshwork, the slope is observed to be significantly steeper (green). In a conventional FCS experiment, the FCS diffusion laws are extrapolate along the dashed lines, yielding positive and negative intercepts with the y-axis for trap and hop diffusion, respectively. Note, that the confined particles are observed to diffuse freely if the size of the observation area is of the same range or smaller than the area of the average molecular traps (X_t^2) or meshwork compartments (X_c^2). (Figure adapted from [62]).

proportional to the observation area. The FCS diffusion law for free diffusion therefore yields a straight line through the origin. If a particle is, however, transiently trapped by the formation of lipid-dependent nanodomains, the transient time comprises both the diffusion time as well as a characteristic trap time t_T which defines the average time for which a particle is immobilized within a single nanodomain. Decreasing the observation area, the fraction of the transient time due to diffusion decreases linearly. The contribution of the trapping time, in contrast, remains constant. Overall, the decrease of the transient time as a function of the observation area is therefore less steep compared to the case of free diffusion as expressed in a reduced slope in the FCS diffusion law (see figure 1.6). Finally, the observation of a particle undergoing hop diffusion within compartments smaller than the observation area results in a steeper FCS diffusion law because each particle needs to cross less barriers on its passage through the decreasing observation area.

Extrapolating the diffusion law to observation areas below the diffraction barrier at around $w_0 = 200$nm, distinct dynamical differences are reflected by characteristic y-axis intercepts ($= 0$ for free, > 0 for trapped and < 0 for hop diffusion) In the past, the FCS diffusion law was applied to characterize different membrane proteins according to their diffusion dynamics [72]. In these experiments, the additional depletion of cholesterol from the plasma membrane as well as the disruption of the cytoskeleton confirmed the assumption that GPI anchored proteins are transiently trapped in cholesterol-induced lipid nanodomains while transmembrane proteins, such as the transferrin receptor, follow a hop-like diffusion within the barriers of the actin-based cytoskeleton.

1.4. Nanoscale dynamics beyond the diffraction limit

Despite the high potential of FCS to study membrane dynamics, the use of conventional diffraction-limited light microscopy restricts the accessible observation areas to be larger than 200nm in diameter. For the direct observation of molecular interactions on the nanoscale, we therefore need to increase the spatial resolution of our system.

In a conventional far-field light microscope, the incoming light is focused by the objective into the sample. Considering that light propagates as a wave, the focal spot is not infinitesimally small but spread out according to the laws of diffraction. In 1873, Ernst Abbe theoretically derived that the minimal size of the focal spot is universally limited to

$$d \approx \frac{\lambda}{2n\sin(\alpha)} = \frac{\lambda}{2NA}. \tag{1.1}$$

Here, λ denotes the wavelength, n the refractive index of the immersion medium and α the semi-aperture angle [1]. The latter two properties characterize the employed objective and are often combined in the numerical aperture $NA = n\sin(\alpha)$. For visible light with $\lambda \approx 500$ nm and a standard oil objective with a numerical aperture of $NA = 1.4$, Abbe's diffraction limit predicts that the minimal focal size is approximately half the wavelength of the light in use. Since two spatially adjacent features within a structure need to be separated by at least the minimal size of the focus to be resolved individually, the best achievable resolution of a conventional light microscope is therefore of the order of 200nm.

The diffraction barrier remains fundamentally true for all forms of light microscopy and cannot be circumvented by changing the applied wavelength, illumination pattern, or the design of the objective lenses. In the case of fluorescence light microscopy, for example, a fluorophore is excited within the focal spot by the absorption of an photon from the electronic ground state S_0 to the first excited state S_1. After a dye

specific lifetime, the excited fluorophore returns to the ground state via the spontaneous emission of a red-shifted photon (see figure 1.7). While the emitted fluorescent light may easily be filtered spectrally from the excitation light, two fluorophores which are separated by less than the minimal focus size will always be both excited and detected at the same time. Since the size of the focal spot cannot be decrease beyond the diffraction barrier, an individual recording of both fluorophores is only achieved if we can control the fluorescent signal of each individual fluorophore in a well defined manner. The key to superresolution must thus be concealed in the physical properties of the fluorescent dye.

The most fundamental physical approach to control the fluorescence of an excited dye molecule is stimulated emission. As depicted in the Jablonski diagram in figure 1.7, stimulated emission is induced by an incoming photon which de-excites the fluorophore by the emission of a second photon of the same wavelength. Since stimulated emission directly competes with the spontaneous fluorescent decay of the excited state, it can effectively be used to switch-off the fluorescence emission. Although the process of stimulated emission had been discovered already in the beginning of the 20th century [73], it was not until 1994 when Hell and Wichmann proposed to exploit the principle of stimulated emission depletion (STED) to break the diffraction barrier [2]. In the basic design of a STED microscope, the excitation laser beam is superimposed with a second laser beam inducing stimulated emission. The wavelength of the second so-called STED laser is deliberately chosen such that it is spectrally separated from the fluorescence signal but still efficiently depletes the excited state population (see figure 1.7).

By increasing the intensity of the superimposed STED laser, the fluorescence signal is gradually reduced until virtually all fluorescent molecules within the STED focus are switched-off. In order to selectively switch-off only fluorophores in the outer part of the focus, the intensity profile of the STED laser is spatially patterned to form a doughnut-like ring featuring a zero intensity right in the center of the focal spot. Even though all fluorescent molecules within the diffraction-limited excitation spot are flooded with excitation light, only those in the very center are able to fluorescently emit and contribute to the detected signal. Scanning this effectively confined focal spot across the sample plane, the fluorescent dye molecules are switched sequentially from a dark OFF-state in the outer parts of the focus to an emitting ON-state right upon entering the center of the doughnut. Two previously unresolved adjacent fluorophores are consequently resolved sequentially in time as the center of the doughnut moves from one to the other.

In STED nanoscopy, the achievable resolution is in principle governed by the size of the zero intensity center from where the remaining fluorescence originates. Since the minimal size of the STED doughnut is equally limited by diffraction, the resolution of the STED microscope can not be improve by decreasing the size of the doughnut.

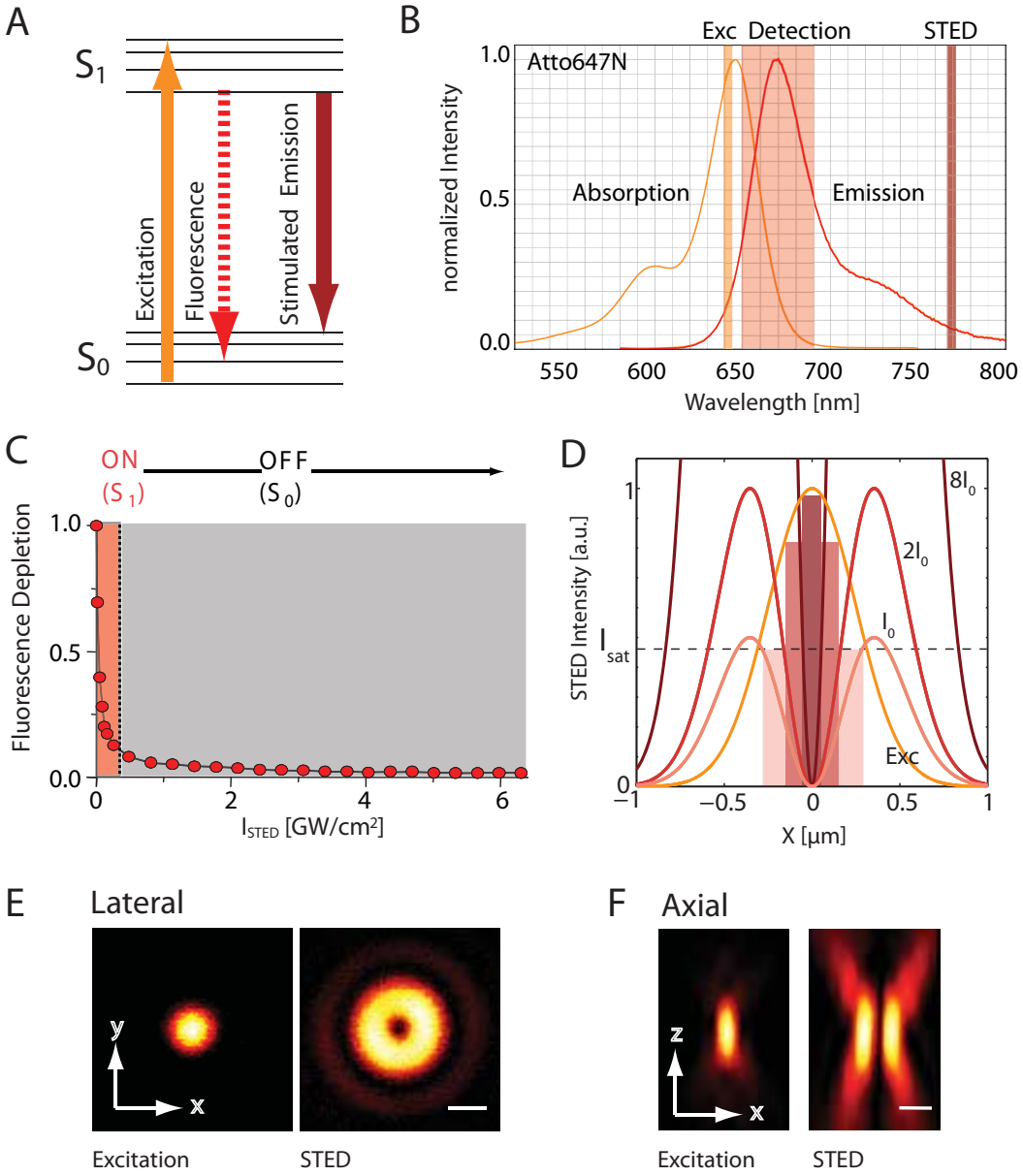

Figure 1.7.: The physical principle of STED microscopy: (A) Jablonski diagram of a fluorescent dye molecule which is excited from the electronic ground state S_0 to the first excited state S_1 by the absorption of an incident photon. The excited state decays by spontaneous emission of fluorescence or stimulated emission. (B) Spectrum of the fluorescence dye Atto647N showing the excitation and STED wavelengths as well as the detection window. (C) Normalized fluorescence depletion reveals the transition from the fluorescent ON- to the non-emitting OFF-state with increasing STED intensity. (D) Schematic representation of the decrease in the effective observation diameter as the STED intensity is increased. (E+F) Axial and lateral focal intensity distributions of the excitation and STED beam as measured in reflection of a colloidal gold particle ($d = 80nm$, scale bar= 250nm). The STED focal distribution exhibits a zero intensity within the center.

We rather need to tune the efficiency of the transition between the ON-OFF states. Considering the typically observed fluorescence depletion as a function of the STED intensity, the fluorescence decays rapidly and is effectively switched-off at intensities above a dye-specific saturation intensity I_s (see figure 1.7). Tuning the intensity of the STED beam, thus enables us to continuously confine the observation area from the confocal focal area down to the in principle infinitesimally small areas, as schematically depicted in figure 1.7. Theoretically, the obtained resolution scales with the STED intensity I_{STED} according to

$$d_{\mathrm{STED}} = \frac{d_{\mathrm{conf}}}{\sqrt{1 + I_{\mathrm{STED}}/I_s}}, \tag{1.2}$$

where d_{conf} corresponds to the diameter of the diffraction-limited confocal focal spot and I_s describes the saturation intensity which characterizes the dye specific depletion efficiency of the applied STED wavelength [74].

Altogether, STED nanoscopy provides us a unique tool to continuously tune the size of the observation area down to the nanoscale. At the same time, the concept of STED nanoscopy still conserves the optical properties of a fluorescence microscope and does not require post-acquisitional data procession. The STED principle can thus be easily transfered to any conventional microscope concept and technique. Especially the combination with FCS, renders the direct observation of diffusion within a nanoscale observation area possible and enables us to directly measure the FCS diffusion law for subdiffractional observation areas [75]. The first application of STED-FCS could successfully assess the diffusion dynamics of lipids within the plasma membrane of the living cell [16]. For the fluorescent lipid analogs under investigation, the experiments provided first evidence that the diffusion of sphingolipids is constrained by the formation of cholesterol-dependent nanodomains with an average size below (< 20nm) while the diffusion of phosphoglycerides was found to be free at all spatial observation scales.

2. Experimental materials and methods

In the following chapter, we introduce the experimental procedures used throughout the first part of the thesis. After a brief summary of the materials and most important preparation protocols, we describe the characteristic features of the experimental setup. A profound mathematical description of the applied analysis techniques at the end of the chapter is thought to guide the reader in the later discussion and interpretation of the experimental results.

2.1. Sample preparation

The key to observe biological phenomena within their natural and undisturbed environment lies in a careful preparation and treatment of the investigated system. This includes the cell culture and preparation, as well as appropriate labeling techniques which specifically allow us to study a particle or structure of interest.

2.1.1. Calibration samples

Especially in a FCS measurement, an accurate calibration of the observation volume is essential for the interpretation of the recorded diffusion times in terms of universal diffusion coefficients. In the following experiments, the calibration of the observation volume as a function of the applied STED intensity is performed using specific calibration samples, such as fluorescent beads or two-dimensional supported lipid bilayers.

Fluorescent beads: Imaging a sample of fluorescent beads allows us to directly determine the lateral resolution for each STED intensity. As described previously [74], we prepare a sample of fluorescent beads by immobilizing $20-40$ nm large crimson or nile red beads (Molecular Probes, Eugene, OR) on a cover glass which was previously coated with poly-L-lysine slide adhesive solution (0.1% w/v in water, Sigma-Aldrich,

Steinheim, Germany). The immobilized fluorescent beads are then embedded either in Mowiol or standard immersion oil and mounted on an standard object slide.

We than record the fluorescence images of the prepared sample for different STED intensities and calibrate the achieved resolution by measuring the average full-width-half maximum (FWHM) for multiple beads within a single image. Note, that the resolution of a STED nanoscope depends on the physical properties of the dye in use. Thus, the calibration of the system is best performed with the same dye used in the later experiment. Since crimson beads share the same spectral prperties as the fluorescence dyes Atto647N or KK114, they may be used for an accurate calibration of the system [76]. Nile red beads, in contrast, exhibit a significantly higher STED efficiency than most organic fluorophores, and are thus unsuited for the setup calibration.

Supported lipid bilayers: A more appropriate way to calibrate the experimental system directly employs the fluorophores used in the later experiment. In our standard calibration scheme, we therefore integrate fluorescently labeled lipid into a two-dimensional supported lipid bilayer (SLB).

The preparation of the SLB follows the protocol descipred in [77]. Briefly, we mix the phosphoglyceride DOPC (1,2-dioleoyl-sn-glycero-3-phosphocholine, Avanti Polar Lipids Inc., Alabaster, USA) with a fluorescent lipid analog (e.g. PE-Atto647N, see below) in organic solvents (Chloroform/MeOH 3:1). The final lipid concentration of the stock solution is 10 mg/ml containing $0.1 - 0.01$ mol% of the fluorescent lipid analog. Subsequently, 25μl of the solution are evaporated for 30 min under vacuum and rehydrated with $50\mu l$ buffer B solution (150 mM NaCl, 10 mM HEPES). The lipid solution is then resuspended by vigorous vortexing for at least 2 minutes and can by stored for several month at $-80°$C.

An aliquot of the stock solution (10μl) is diluted in 140μl of the buffer B solution and sonicated for 30 min at 35°C until the solution becomes transparent. The solution is then pipetted onto a standard cover glass previously cleaned by plasma-cleaning (Femto-RF, Diener Electronic, Nagold, Germany) or alternatively cleaning in piraña solution (1:2 mixture of hydrogenperoxid and sulfuric acid). The fusion of the liposome within the solution is induced by the addition of $CaCl_2$ to a final concentration of 3 mM. After an incubation time of 30 min, the sample is carefully rinsed and kept hydrated under buffer solution.

In order to calibrate the size of the observation area, we record the fluorescence intensity traces within the SLB and acquire the fluorescence correlation curves for increasing STED intensities I_{STED}. For a known diffusion coefficient D, the achieved diameter of the observation area is given by

$$\mathrm{FWHM}(\mathrm{I_{STED}}) = \sqrt{8\ln(2)\tau_{\mathrm{D}}(\mathrm{I_{STED}})\mathrm{D}}. \tag{2.1}$$

Plotting the FWHM as a function of the applied STED intensity, we can fit the experimental data to the theoretically expected resolution as given in equation 1.2. A corresponding data fit provides us with the saturation intensity I_s and enables us to calibrate the size of the observation area for arbitrary STED intensities.

2.1.2. Fluorescent dyes and lipid analogs

The following experiments are performed either with red or green excitation light. For experiments with a red excitation wavelength at 635 nm, we use the lipophilic organic dyes Atto647N (Atto-Tec, Siegen, Germany) and KK114. The fluorescence spectrum of Atto-647N, shown in figure 1.7, exhibits an excitation and emission maximum at 645 and 670 nm, respectively. Experiments with green excitation wavelength at 532 nm are carried out using either the hydrophilic organic dyes Atto-532 or Atto-565. For theses dyes, the emission maxima are around 532 and 565 nm and the excitation maxima are found at 553 and 585 nm (all Atto-Tec). Intracellular labeling is achieved using membrane permeable dyes such as, for example, TMR featuring an excitation and emission maximum at 554 and 585 nm (Covalys Biosciences, Witterswil, Switzerland).

The synthesis of the fluorescent lipid analogs is performed as described in [78, 79]. In general, all lipids are either labeled at the head group (i.e. the water phase) or at the water-lipid interface by replacing one of the native acyl chains by a shorter acyl chains carrying the fluorescent dye. The chemical structure of all fluorescent lipid analogs used throughout this thesis is presented in figure 2.1.

2.1.3. Cell preparation

Cell culture: The mammalian PtK2 cell line (potoroo kidney) is cultured in Dulbecco's Modified Eagle Medium (DMEM) supplemented with 5% fetal calf serum, 100 U/ml penicillin, 100μg/ml streptomycin (all Invitrogen) and 1 mM pyruvate (Sigma) at 37° C kept within a water-saturated atmosphere of 5% CO_2 in air. Previous to the experiments, cells are seeded on standard glass coverslips (d=10-18 mm, no. 1 thickness) to a confluence of about 80% and grown at 37°C for 24 hours.

The human HeLa cell line is grown in Glutamax (high glucose, Invitrogen) supplemented with 10% fetal bovine serum, 100 U/ml penicillin, 100μg/ml streptomycin and 1 mM sodium pyruvate. Like the PtK2 cells, HeLa cells are seeded on standard glass coverslips to a confluence of about 80% one day prior to the experiments.

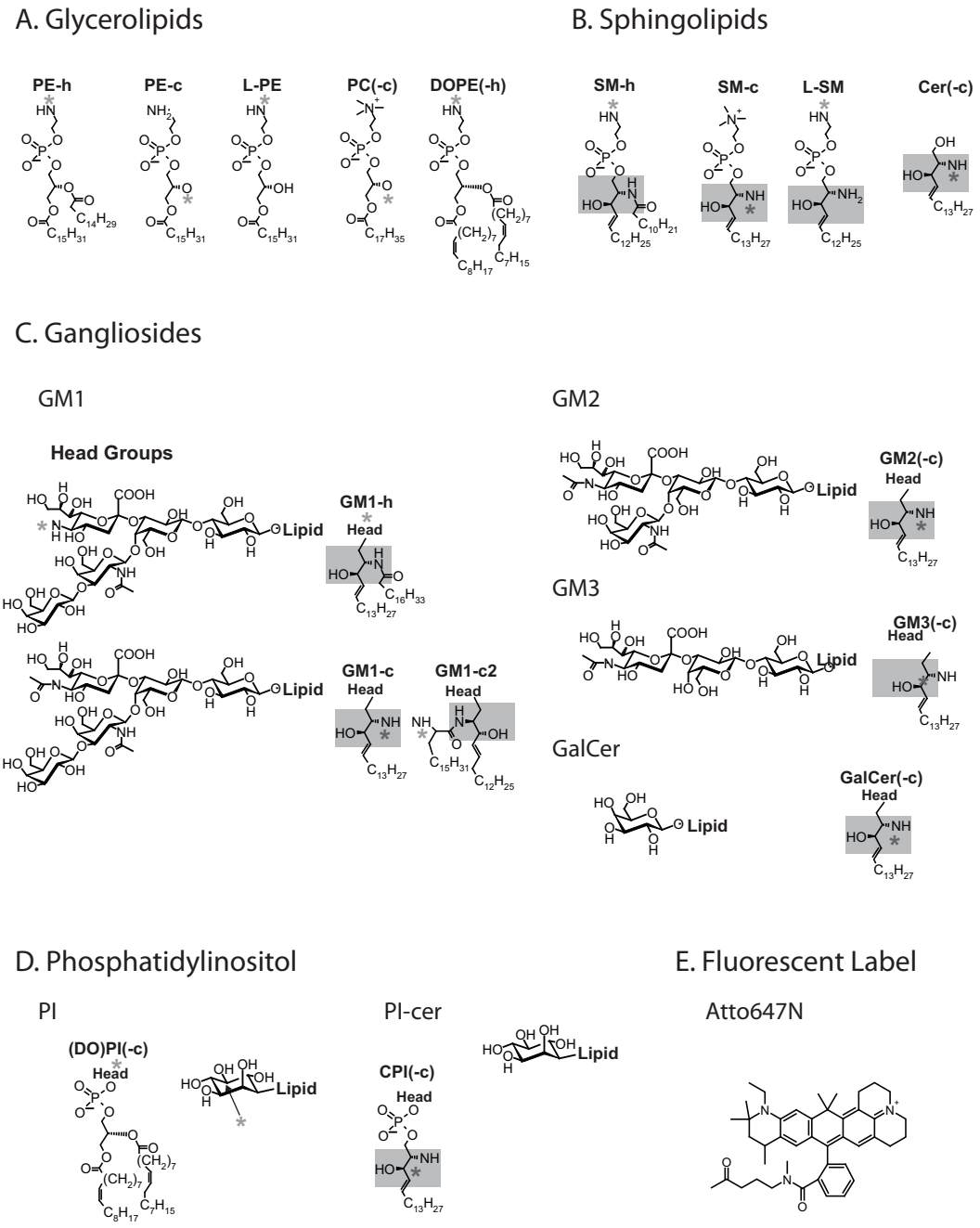

Figure 2.1.: Chemical structure of the fluorescent lipid analogues studied throughout the experiments. The asterisk (*) denotes the position of the fluorescent label, as for example Atto-647N.

Cell transfection: In order to study the diffusion of membrane proteins, the proteins of interests are genetically expressed as fusion proteins combining the protein with a SNAP or ACP-tag protein. The construction of the plasmids encoding the fusion protein is performed according to standard protocols as described in [80]. Twenty-four hours previous to the experiment, PtK2 cells are transfected with the endotoxin-free DNA via Nanofectin following conventional transfection procedures (PAA, Pasching, Austria).

Fluorescent labeling of lipids: Lipid labeling is achieved by the incorporation of fluorescent lipid analogs into the plasma membrane of the living cells. The passive incorporation of the lipids is facilitated via the formation of a Bovine Serum Albumin (BSA) complex of the fluorescent lipid analog with BSA as described in [78] and schematically depicted previously in figure 1.5.

Briefly, the BSA complex is prepared by drying 100 nmol of the lipid stock solution under a stream of nitrogen. The dried lipids are then dissolved in 20μl of absolute ethanol and subsequently diluted in 1 ml of defatted BSA solution ($10-4$ M defatted BSA in DMEM without phenol-red buffered with 10 mM HEPES). The suspension is vigorously vortexed to ensure that the fluorescent lipid analogs are effectively integrated into the lipophilic pockets of th BSA molecule. Adding 9 ml HDMEM (HEPES + DMEM = HDMEM) results in a final concentration of $10-20\mu$M BSA and 0.2% (v:v) ethanol depending on the fluorescent lipid analog.

The BSA-lipid-stock solution is then diluted in HDMEM to a final concentration of $5-500$ nM, varying for the individual fluorescent lipid analogs. Previous to the fluorescent labeling, the cells are washed in warm HDMEM and incubated with the diluted BSA-lipid solution for 30 min on ice (≈ 4°C). Afterwards, cells are briefly washed in cold HDMEM and mounted into a microscope chamber. Note, that labeling with sphingomyelin based fluorescent lipid analogs requires additional incubation at 37°C for 4 min in warm HDMEM.

Fluorescent labeling of membrane proteins: ACP and SNAP tags are used to label previously genetically expressed fusion proteins with organic dyes such as Atto-647N, Atto-565 as well as the membrane permeable dyes TMR or SiR650.

In a Snap-tag based labeling procedure, PtK2 cells are incubated for 15 min at 37°C in DMEM supplemented with 1μM of Atto-565 or TMR-star (Atto-Tech and Covalys Bioscience). Upon incubation, cells are washed for 15 min in DMEM. For an intracellular staining with TMR, cells are additionally washed for at least 15 min to ensure effective depletion of unbound intracellular TMR.

In an ACP-tag based labeling procedure, PtK2 cells were incubated for 30 min at 37°C in DMEM supplemented with 5mM CoenzymA-Atto647N (AttoTec), 5 mM $MgCl_2$ (Fluka) and 1 mM ACP synthase (Covalys). Cells were then carefully washed in DMEM and directly mounted into the microscopy chamber.

2.1.4. Drug treatment

In order to evaluate the structural influences of the plasma membrane on the diffusion dynamics of membrane lipids and proteins, we altered the physiological composition of the plasma membrane by either depleting the cholesterol contents of the cell or partially disrupting the underlying cytoskeleton.

Cholesterol depletion: In order to deplete the cholesterol contents from the plasma membrane, cells are incubated in HDMEM supplemented with 1 U/ml cholesterol oxidase (COase, streptomyces spec., Sigma aldrich, St.Louis, USA) from a freshly prepared stock solution of 34 U/ml in 50 mM KH_2PO_4 (pH 7.5) for 30 min under cell culture conditions.

While COase treatment results in an effective oxidation of cholesterol to cholestenon, a virtual extraction of the cholesterol from the membrane is achieved by treating the cells with 10 mM of β-cyclodextrin (β-CD, Sigma) in HDMEM for 30 min under cell culture conditions. Subsequently to COase or β-CD treatment, cells are washed and labeled according to the previously described labeling procedures. Note, that cholesterol depletion also effects the structure of the actin-based cytoskeleton, as shown in figure 2.2.

Alternatively, the cholesterol contents of the membrane can be reduced by a partial inhibition of the sterol synthesis by a long-term treatment with 5 μM Zaragoic Acid A (Sigma-Aldrich) for 48 h at 37°C in serum staved HDMEM.

Actin-based cytoskeleton: An effective disruption of the actin-based cytoskeleton was achieved by treating the cells with 1μM Latrunculin B (Sigma-Aldrich) for 5-30 min at 37°C under culture conditions. Latrunculin B is known to bind actin monomers and thus prevents the polymerization of actin-filaments. Figure 2.2 illustrates the gradual degradation of the actin network until the complete disruption after 30 minutes.

Alternative treatment with 1-10 μM Cytochalasin (Calbiochem, Merck) for 30 min at 37° C under culture conditions, depletes the actin filaments by directly inhibiting the actin polymerization process. The actin-based cytoskeleton can further be stabilized and enhanced by treating the cells with 0.4 μM Jasplakinolide (Calbiochem) for 5 min

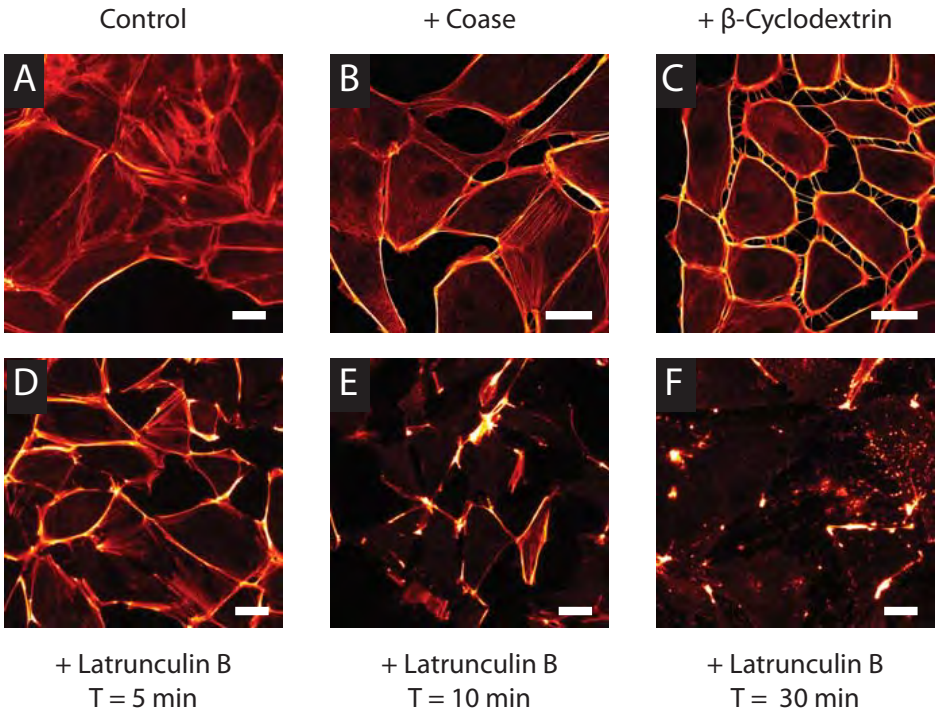

Figure 2.2.: Influences of drug treatment on the physiological structure of the actin-based cytoskeleton: Compared to the control measurement (A), cholesterol depletion with cholesterol oxidase (B) or β-cyclodextrin (C) induce a rearrangement of the actin filaments and general structure of the cells. (D-F) Upon treatment with Latrunculin B, the actin-based meshwork is depolymerized leading to a complete disruption of the meshwork after 30 minutes. (PtK2-cells stained with phalloidin-Oregon-Green488 (Invitrogen), scale bar 50 μm.)

at 37° C under culture conditions. We note, however, that Jasplankinolide is found to bind and stabilize actin filaments in vitro, but may induce an opposite disruption of the filaments in in-vivo experiments [81].

Tubulin-based cytoskeleton: Treatment with 15 μM Nocodazol (Calbiochem) for 3h at 37°C under culture conditions allows for the destruction of tubulin-filaments by an effective inhibition of the polymerization process. Note, that the effect of Nocodazol treatment is fully reversible by washing and a subsequent recovery period of 30 min at 37°C.

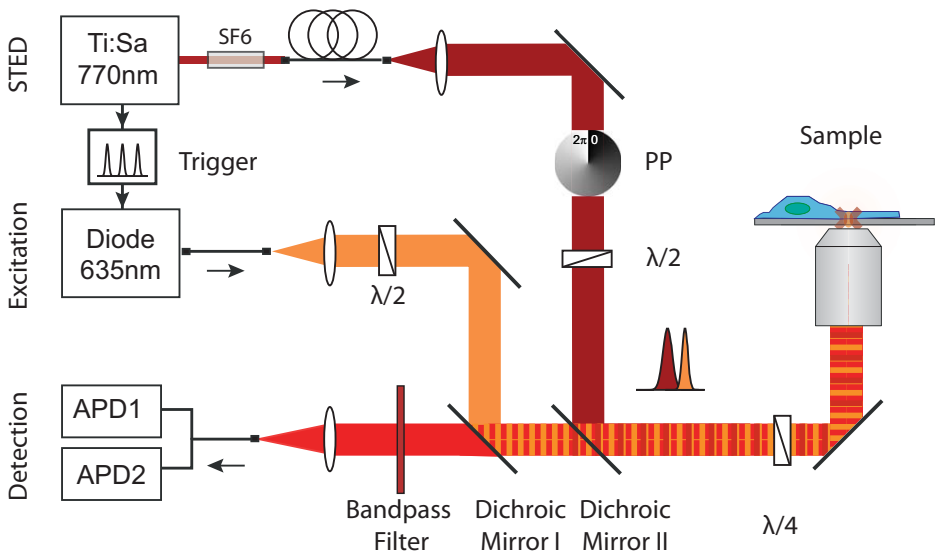

Figure 2.3.: Overview of the experimental setup: The excitation (orange) and STED (dark red) laser beams are overlaid using two dichroic mirrors and focused into the sample. The emitted fluorescence (red) from the sample is filtered using a bandpass filter and detected onto two avalanche photon detectors (APD). The polimeric phase plate (PP) induces a clockwise 2π-phase shift across the STED beam which generates the doughnut shaped focal intensity distribution in the focal plane. Note, that the circular polarization of both laser beams is maintained by a combination of $\lambda/2$ and $\lambda/4$ waveplates (PMS= Polarization maintaining single-mode fiber, SF6= SF6 glass rod).

2.2. Experimental setup

The STED nanoscope used throughout this part of the thesis is based on a custom-built microscope system. In the following we briefly describe the main features of the experimental setup illustrated in figure 2.3.

The confocal unit of the STED nanoscope consists of an excitation and detection beam path. For the excitation of red fluorescence, a fiber-coupled pulsed laser diode generates the excitation light with a wavelength of $\lambda_{exc} = 635$nm and a pulse length of 80 ps (LDH-P-635, PicoQuant, Berlin, Germany). After the fiber, the excitation beam is expanded and focused into the sample using an oil immersion objective (HCX-PLAPO 100x, NA = 1.4, Leica Microsystems). The emitted fluorescence within the sample plane is collected by the same objective lens and separated from the excitation light by a custom built dichroic mirror (AMS Technologies, Munich, Germany). In the following detection unit, the fluorescence is filtered via a 675/40 bandpass filter and focused onto a multi-mode fiber splitter (Fiber Optic Network Technology, Sur-

rey, Canada). The aperture of the fiber acts like a confocal pinhole covering 78% of the back-projected Airy disk. The 50:50 split fluorescence signal is detected by two single-photon counting modules (APD, SPCM-AQR-13-FC, Perkin Elmer Optoelectronics, Fremont, CA). The detected fluorescence counts are either recorded as a function of time or space using a time-correlated single photon counting device (SPC-150, Becker&Hickl, Berlin, Germany) or directly correlated by a hardware correlator (Flex02-01D, Correlator.com, NJ, USA).

In order to increase the spatial resolution of the system beyond the diffraction barrier, the confocal microscope is extended by the integration of a STED laser beam. For the depletion of red fluorescence, the STED laser is provided by a Titanium:Sapphire laser system (Ti:Sa, MaiTai, Spectra-Physics, Mountain View, USA) operating at $\lambda_{\mathrm{STED}} = 770$nm with a repetition rate of 80 MHz. The fs-pulses are first stretched to a pulse length of approximately 250-350 ps by a SF6 glass rod of 50 cm and a 120 m long polarization maintaining single-mode fiber (PMS, OZ Optics, Ontario, CA). After the fiber, the STED beam is expanded and passes trough a polymeric phase plate (RPC Photonics, Rochester, NY) which induces a helical phase ramp of $\exp(i\phi)$ with $0 \leq \phi \leq 2\pi$ across the beam diameter. This phase shift gives rise to the doughnut-shaped focal intensity distribution featuring a central zero intensity as shown in figure 1.7. The STED beam is then spatially overlaid onto the excitation beam by a dichroic mirror (AHF Analysentechnik, Tübingen, Germany) and focused into the sample. To ensure an efficient depletion of the fluorescence, it is crucial to synchronize the timing of the excitation and STED laser pulses. In our experimental setup, the temporal synchronization is achieved by triggering the pulses of the excitation laser using the trigger signal from an internal photodiode inside the STED laser. The final delay between both pulses is adjusted by a home-built electronic delay unit which allows us to adjust the delay manually with a resolution of 25 ps. Note, that the circular polarization of the STED and excitation laser light in the focal plane is maintained by a combination of a $\lambda/2$ and $\lambda/4$ retardation plate in both beam paths (B.Halle, Berlin, Germany).

In order to precisely position the laser foci within the sample, we can either scan the beam across the focus plane or move the sample in respect to the laser beam. In our experimental system, the sample is fixed on a custom build translation stage which allows to coarsely position the sample in all three dimensions. An additional beam scanning mirror system is employed to precisely translate the laser in the lateral direction (PSH 10/2, Piezosystem Jena, Jena, Germany). The accurate axial positioning is performed by moving the objective lens using an axial piezo positioning system (MIPOS 250, Piezosystem Jena).

All measurements observing the green fluorescence of the organic dyes Atto-532, Atto-565 and TMR were performed at a second experimental setup. While the general designs of both setups are identical, the second setup employs different excitation

and STED wavelength. The excitation laser is provided by a pulsed laser diode with a wavelength of $\lambda = 532$nm and a pulse length of 80 ps (LDH-P-FA-530XL, PicoQuant). The STED laser light with a wavelength between $\lambda_{\mathrm{STED}} = 600 - 660$nm is generated by an optical parametric oscillator (OPO, APE, Berlin, Germany) pumped with a Titanium:Sapphire laser system (Ti:Sa, MaiTai, Spectra Physics) at $\lambda_{\mathrm{pump}} = 839$nm and 80 MHz repetition rate. All laser lines are separated using custom-build dichroic mirrors and the emitted fluorescence is detected via a 680/20 bandpass filter (AHF Analysentechnik).

2.3. Statistical data analysis

During the last years, several statistical analysis methods have been developed in order to analyze either temporal or amplitude fluctuations of a fluorescence signal [82]. Although this work focuses on the evaluation of temporal fluctuations, we note that the analysis of amplitude fluctuations can be elegantly used to deduce the molecular brightness and average particle number of the fluorescent species as established in recent advanced analysis methods such as fluorescence intensity distribution analysis (FIDA), photon counting histograms (PCH) or cumulant analysis [83, 84, 85].

Mathematically, the temporal correlation of the fluorescence signal $F(t)$ is given by the normalized autocorrelation function $G(\tau)$ which is given at the delay time τ as

$$G(\tau) = \frac{\langle \delta F(t) \delta F(t+\tau) \rangle}{\langle F \rangle^2}, \tag{2.2}$$

where $\delta F(t) = F(t) - \langle F \rangle$ describes the fluorescence fluctuations around the average fluorescence signal $\langle F \rangle$ at time t [59]. A typical FCS curve as shown in figure 1.5 allows us to estimate the average number of particles which is inversely proportional to the correlation amplitude $G(0)$ as well as the diffusion time, approximately given by the time at which the correlation amplitude has dropped to half of its initial amplitude. An accurate determination of both variables, however, requires a carefully derivation of an mathematical model which theoretically describes the correlation curve.

If we assume that the observed fluctuations in the fluorescence signal are caused by characteristic variations in the concentration of the fluorescent molecules due to either diffusion within the observation volume or chemical processes such as triplet state formation, the correlation function can be written as

$$G(\tau) = \frac{1}{N} G_D(\tau) \cdot G_T(\tau) \cdot G_K(\tau). \tag{2.3}$$

Here, N denotes the average number of particles in the observation volume and $G_D(\tau)$ and $G_T(\tau)$ characterize the contributions to the correlation due to translational diffusion or triplet state formation. The additional kinetic term $G_K(\tau)$ includes for instance

conformational changes or chemical binding processes which induce a change in the fluorescent brightness of the molecule [86].

For a freely diffusing single species, the analytical description of the correlation term due to diffusion $G_D(\tau)$ is derived in appendix 10 and given by

$$G_D(\tau) = \frac{1}{1+\frac{\tau}{\tau_D}} \left(\frac{1}{1+(\frac{w_r}{w_z})^2 \frac{\tau}{\tau_D}} \right)^{1/2}, \tag{2.4}$$

where the diffusion time $\tau_D = \frac{w_r^2}{4D}$ describes the time a particle needs to transverse the observation volume in the xy-plane [86]. Note, that the second term of the equation corresponds to the axial movement and can be omitted in the case of a strictly two-dimensional diffusion.

The contribution in the correlation due to triplet state population and depopulation $G_T(\tau)$ are determined by the equilibrium fraction of fluorescent molecules in the triplet state T_1 as well as the triplet time τ_T according to [87]

$$G_T(\tau) = \frac{T_1}{1-T_1} \exp\left(\frac{\tau}{\tau_T}\right). \tag{2.5}$$

Note, that the triplet state characteristics are dye specific and depend on the excitation intensities applied. Since they are however independent of the shape and size of the observation volume, the triplet state amplitude and time can be determined in a confocal measurement and fixed for later STED recordings with smaller observation areas. At typical excitation powers used in our experiments, Atto-647N features an average triplet amplitude of 10% with a triplet time around $\tau_T = 5\mu s$.

In correspondence to the triplet term, the correlation due to additional kinetics are expressed by

$$G_T(\tau) = K \exp\left(\frac{\tau}{\tau_K}\right), \tag{2.6}$$

where K denotes the amplitude and τ_K the characteristic conversion time of the kinetic process. Especially in cell measurements, we identify the presents of an additional kinetic process with an amplitude of $K = 0.05 - 0.1$ and a characteristic time of $\tau_K = 50 - 150\mu s$. Possible explanations for this kinetic term are either an additional dark state of the fluorophore or conformational fluctuations of the dye-lipid system altering the molecular brightness of the dye.

Although the analytical model of the correlation function can be easily extended to the situation of multiple diffusing species, we emphasize that the analysis is prone to artifacts and requires a careful consideration of the experimental situation. The derivation of the diffusion based correlation as outlined in appendix 10 is for instance only

valid for a Gaussian intensity distribution of the excitation spot. A deviation in the focal shape due to optical aberrations directly yields to an inaccurate determination of the diffusion coefficient [88]. Since the observation volume in STED-FCS measurements is best approximated with a Lorentzian illumination profile, the assumption of a Gaussian illumination profile slightly affects the observed diffusion coefficients [89]. Furthermore, FCS experiments inside a living system are challenged by the accurate positioning of the focal spot within the membrane. A slight misplacement of the two dimensional membrane in the axial direction or an oblique passage of the laser beam through the membrane, for instance, directly deviate the effective observation area and lead to an artificial increase of the measured diffusion times [90].

Even more importantly, we emphasis that the theoretical model may only be applied, if it accurately reflects the underlaying diffusion modalities of the system. Considering that the discussed theoretical model was derived assuming free Brownian diffusion, it fails to accurately describe correlation curves measured in systems where the diffusion is, for instance, constrained by impermeable obstacles or transient binding processes to mobile or immobile complexes. In the following, we therefore present two approaches, that can be used to account for anomalous diffusional effects.

Anomalous diffusion: Unspecified deviations from free Brownian diffusion may be generally analyzed using the model of anomalous subdiffusion [55]. In contrast to the case of free diffusion, the mean square displacement $\langle \delta r^2 \rangle$ for anomalous diffusion is not proportional to the elapsed time but follows a power law according to $\langle \delta r^2 \rangle = 4Dt^\alpha$. Here, D denotes the diffusion coefficient, while the anomalous diffusion exponent α provides a measure for the anomaly of the diffusional process: For $\alpha = 1$, the diffusion converges to the case of free Brownian diffusion, whereas smaller $\alpha < 1$ characterize the occurrence of external constraints resulting in an anomalous subdiffusion.

For a two-dimensional system such as the plasma membrane, the correlation function for anomalous diffusion is derived from the non linear time dependence of the mean square displacement yielding [55]

$$G_D(\tau) = \frac{1}{1 + \left(\frac{\tau}{\tau_T}\right)^\alpha} \quad \text{with} \quad \tau_\mathrm{T} = \frac{\mathrm{d}^2}{8 \ln(2) \mathrm{D}_\mathrm{app}}. \tag{2.7}$$

Here, the in average observed transient time τ_T of the constrained particle defines the apparent diffusion coefficient D_app which denotes the diffusion coefficient for a freely diffusing particle yielding the same transient time as the constrained particle.

In the case of free Brownian, $D_\mathrm{app} = D$ is constant for varying focal sizes and $\tau_T = \tau_D$ scales linearly with the focal area d^2. In the case of anomalous diffusion, the observed degree of anomaly, usually referred to as $1/\alpha$, depends on the observation size. If the

spatial and temporal dimension of the process constraining the diffusion are negligible compared to the size of the focal area and transient time, the particle appears to diffuse freely with an in average slightly larger diffusion time τ_D and $\alpha = 1$. As soon as the dimensions of the focal area and transient time are in the order of the constraining dimensions as for instance the trap size or time, the anomalous character of the diffusion becomes more apparent and α decreases. Thus, the apparent diffusion coefficient $D_{\text{app}} \propto 1/\tau_T \propto 1/\tau_D^{1/\alpha}$ decreases as a function of the observation size.

We note that in the analysis of STED-FCS experiments the invalid assumption of a Gaussian illumination profile might introduce an artifact in the determination of the anomaly. This artifact can however be derived from measurements in a free diffusing model membrane. Here, we find that the anomaly for small focus sizes are significantly smaller than the anomaly observed in the case of a constrained diffusion within the plasma membrane (e.g $\alpha = 0.9$ in SLB and $\alpha = 0.7$ in constrained cell measurements).

Transient binding: The second approach to quantitatively assess anomalous diffusion is based on the binding kinetics expected for a freely diffusing particle that attaches transiently to an immobile or slowly moving interaction center.

Such reactions are in general characterized by the transition rates of the binding process. Precisely, the effective encounter rate k_{on} defines the probability with which a particle is bound to an interaction center whereas the dissociation rate k_{off} determines the average time for which a particle remains attached to the interaction point as $\tau_{\text{trap}} = 1/k_{\text{off}}$. If this trapping time τ_{trap} is much longer than the average diffusion time $\tau_{D\text{free}}$ of a freely diffusing particle the diffusion is reaction-dominated and the theoretical correlation function is described as

$$G_D(\tau) = (1 - B)\frac{1}{1 + \frac{\tau}{\tau_{D\text{free}}}} + B \exp\left(-k_{\text{off}}\tau\right). \tag{2.8}$$

Here, the amplitude $B = k_{\text{off}}/(k_{\text{off}} + k_{\text{on}})$ reflects the average fraction of particles bound to interaction centers [91].

In comparison to the anomalous diffusion model, the model of transient binding can uniquely be applied for diffusion constrained by the formation of transient confinement centers. It, however, allows a more quantitative characterization of the underlying kinetic processes than the determination of the anomaly, which neither resolves the fraction of trapped molecules nor the trap duration.

3. Membrane dynamics of lipids

The plasma membrane of the living cell shows a remarkable diversity of different lipid species. Although the specific composition of lipids within the membrane has long been determined, surprisingly little is known about the impact of the different lipid species on cellular processes and functions.

Considering the remarkably high fluidity of the plasma membrane, the study of lipid dynamics certainly is an important key towards a comprehension of lipid functionality. In this chapter, we discuss, how the high spatial and temporal resolution of STED-FCS can be used to directly access lipid dynamics within the plasma membrane. Comparing the dynamical characteristics for a variety of different lipids further allows us to identify features in the chemical structure that essentially effect the diffusion modalities. Finally, we investigate, in how far lipid dynamics are influenced by the cholesterol content of the plasma membrane or the underlying cytoskeleton meshwork.

3.1. Nanoscale diffusion of membrane lipids

First, we study the diffusional characteristics of two distinct lipids: the phosphoglycerolipid phosphatidylethanolamine (PE) and the sphingolipid sphingomyelin (SM). For both lipids, a fluorescent lipid analog is synthesized and incorporated into the plasma membrane of a living PtK2 cell.

Recording the confocal correlation curves as depicted in figure 3.1, we find that the obtained correlation curves are comparable for both lipid species. The inflection points of both curves provide a rough estimate of the transient time τ_T, and is slightly shifted towards longer delay times for SM compared to the PE measurement. This minor differences are confirmed by fitting the data to the model of anomalous diffusion in equation 2.7. The retrieved transient time for SM is of the order of $\tau_T \approx 30$ms and thus significantly longer than the transient time of PE which is determined to be $\tau_T \approx 20$ms. The fit further provides us with an estimation of the degree of anomaly $1/\alpha$. Since $1/\alpha$ is close to one for both recordings, the confocal recordings provide no indication for anomalous diffusion but suggest that both lipids diffuse freely with a slightly decreased mobility for SM.

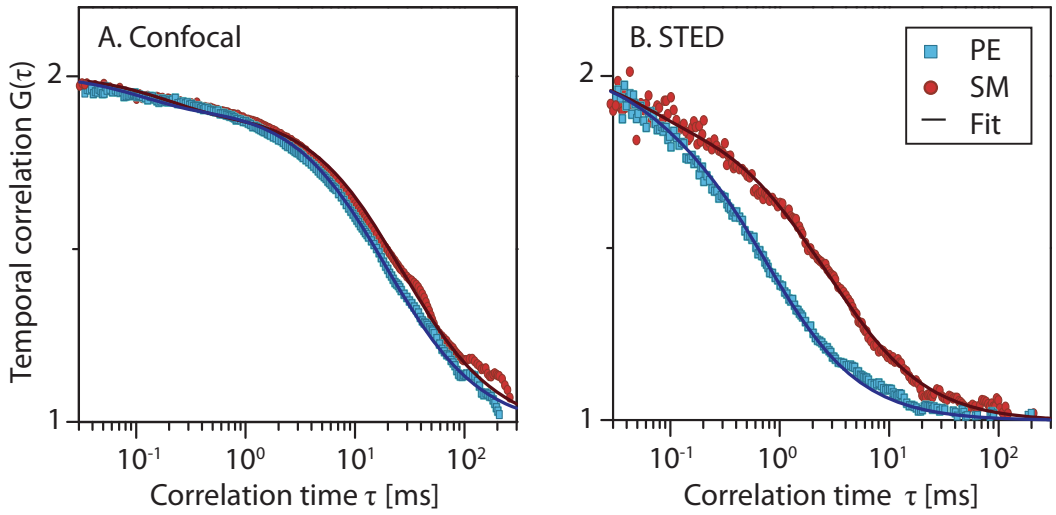

Figure 3.1.: Typical FCS recordings for PE (blue) and SM (red): (A) The normalized correlation curve of the confocal measurement are comparable for both lipids. (B) A STED recording with a nanoscale observation area of 40 nm reveals distinct qualitative differences in the diffusion between both lipids.

We repeat the experiment using STED to confine the observation area down to a diameter of 40 nm. In comparison to the confocal recording, the correlation curves of the STED recording in figure 3.1 indicate a distinct difference between the diffusion characteristics of PE and SM. While the correlation function of PE can still be accurately fit assuming a free diffusing species $1/\alpha \approx 1$, the fit to the correlation curve of SM results in an increase of the anomaly $1/\alpha \approx 1.4$, as well as significantly slower transient time $\tau_T \approx 2.5$ms compared to PE for which $\tau_T \approx 1$ms.

The application of STED thus allows to directly resolve differences in the diffusion through a nanoscale observation area beyond the diffraction limit. The general application of the theoretical model for anomalous diffusion does however fail to identify the underlying principle constraining the diffusion and does not reveal if the diffusion is for instance hindered by the formation of lipid-dependent nanodomains or the barriers of cytoskeleton-based meshwork.

3.2. Exploring the origins of anomalous diffusion

In order to gain additional insights on the mechanism constraining the diffusion dynamics, we record the correlation curves for different sizes of the observation area. Increasing the STED intensity, we tune the observation area and determine the transient time and anomaly for several observation diameters in the range between 250

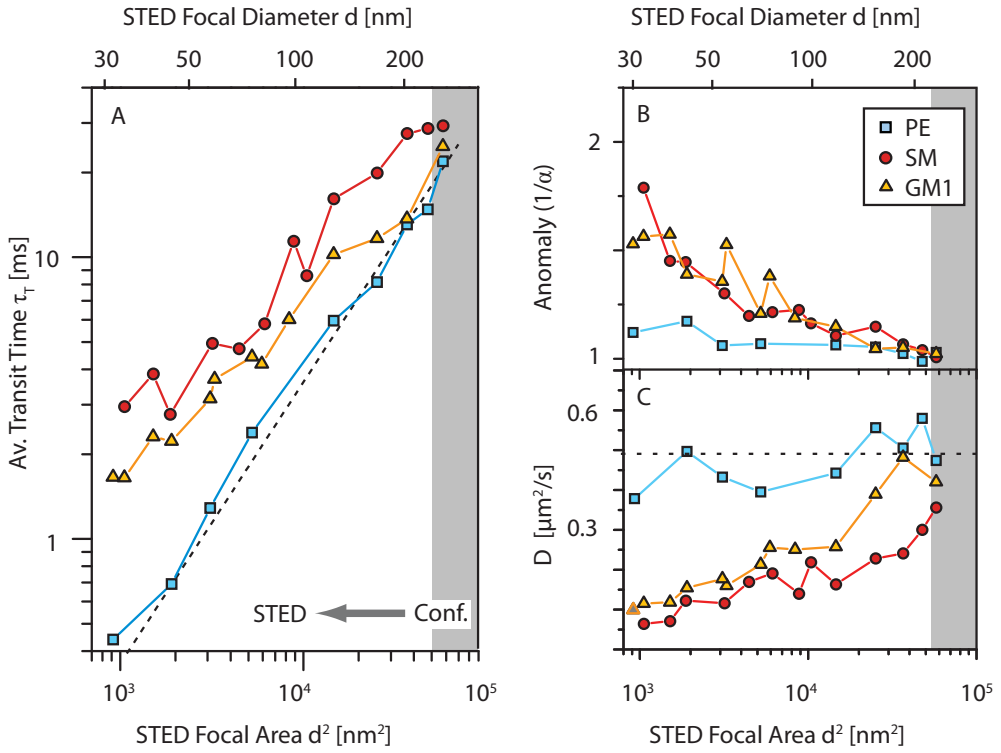

Figure 3.2.: FCS Diffusion law for PE (blue), SM (red) and GM1 (yellow): (A) The average transient time τ_T is plotted as a function of the focal area d^2. It follows a linear dependence for PE, in contrast to SM and GM1 (see dotted line). (B) At the same time, the anomaly $1/\alpha$ remains close to 1 for PE, but increases with decreasing focal area for SM and GM1. (C) The apparent diffusion coefficient D_{app} reflects the dependence of the transient time on the observation area and is observed to remain constant for PE, but decreases for smaller observation areas in the case of SM and GM1.

nm to 40 nm. In figure 3.2, the transient time and anomaly are plotted as a function of the observation area for PE, SM and a ganglioside GM1.

The dependence of the transient as a function of the observation area, known as the FCS diffusion law, qualitatively reflects the diffusion characteristics of a particle, as discussed previously in section 1.3.2. In the case of PE, the transient time decreases linearly with the focal area as it is expected for a freely diffusing particle. The diffusion law for SM and GM1, in contrast, follows a non-linear dependency: For small focus areas, the apparent diffusion is significantly slower than expected for a freely diffusing particle. This increase in the transient time can be explained by transient arrests of the particle during the diffusion pathway. In such a trapping event, the particle is effectively confined or slowed down for a characteristic trapping time τ_{trap} which is independent of the observation area. While the occurring trap events merely slow

down the diffusion observed in large observation areas, the transient time for small focus sizes is predominately determined by the trapping events. The prevalence of trapped diffusion does not only increase the transient time but also results in an increase of the anomaly $1/\alpha$ as shown in figure 3.2.

Calculating the apparent diffusion coefficient $D_{\mathrm{app}} = d^2/(8\ln(2)\,\tau_T)$ from the observed transient time as shown in figure 3.2, the linear dependence for PE is reflected in a constant value of D_{app} for all observation areas. The apparent diffusion coefficients of SM and GM1, in contrast, decrease for decreasing observation areas. The degree of confinement as a combination of trap time and amplitude can be determined as the relative decrease of the diffusion coefficient at a certain focal diameter compared to the confocal measurement. In the following, the ratio $D_{\mathrm{STED}}/D_{\mathrm{Confocal}}$ is therefore used to quantitatively evaluate and compare the diffusion characteristics of different lipids.

At small focal areas, we can further assume the diffusion of the lipids to be dominated by transient binding events. Thus, we may apply the model of transient binding to describe the recorded correlation curves. Fitting the data, this analysis yields an accurate description of the recorded data for SM and GM1 with an observed encounter rates of $k_{\mathrm{on}} = 30{-}100\mathrm{s}^{-1}$ as well as dissociation rates of $k_{\mathrm{on}} = 50{-}100\mathrm{s}^{-1}$. Interpreting the results, we derive a quantitative estimation of the trap time $\tau_{\mathrm{trap}} = k_{\mathrm{off}}^{-1} = 10 - 20\mathrm{ms}$. We note, that the analysis assuming transient binding events is uniquely valid for reaction-dominated processes and can therefore only be applied for recordings in small focus areas for which the trap duration is much larger than the time that the particle diffuses freely within the focus area. This condition is sufficiently fulfilled for focus sizes around 50 nm, for which the diffusion time of a freely diffusing particle $\tau_D \approx 1 - 1.5\mathrm{ms}$ is significantly smaller than the trap time $\tau_{\mathrm{trap}} = 10\mathrm{ms}$.

3.2.1. Effects of molecular structure

In order to fully understand the molecular interaction responsible for the observed constrained lipid dynamics, we investigate the diffusion characteristics for a variety of different lipids.

As discussed in the previous section, STED-FCS provides us with a valuable differentiation between free and constrained diffusion which can be quantified not only in terms of the anomaly $1/\alpha$ but also in terms of the ratio of the apparent diffusion coefficients $D_{\mathrm{STED}}/D_{\mathrm{Confocal}}$. While for a freely diffusing particle the apparent diffusion coefficient is constant and the ratio is observed to be one, an anomalous diffusion is characterized by significantly smaller ratios $D_{\mathrm{STED}}/D_{\mathrm{Confocal}} << 1$. In the following we thus evaluate the molecular characteristics responsible for anomalous diffusion by plotting

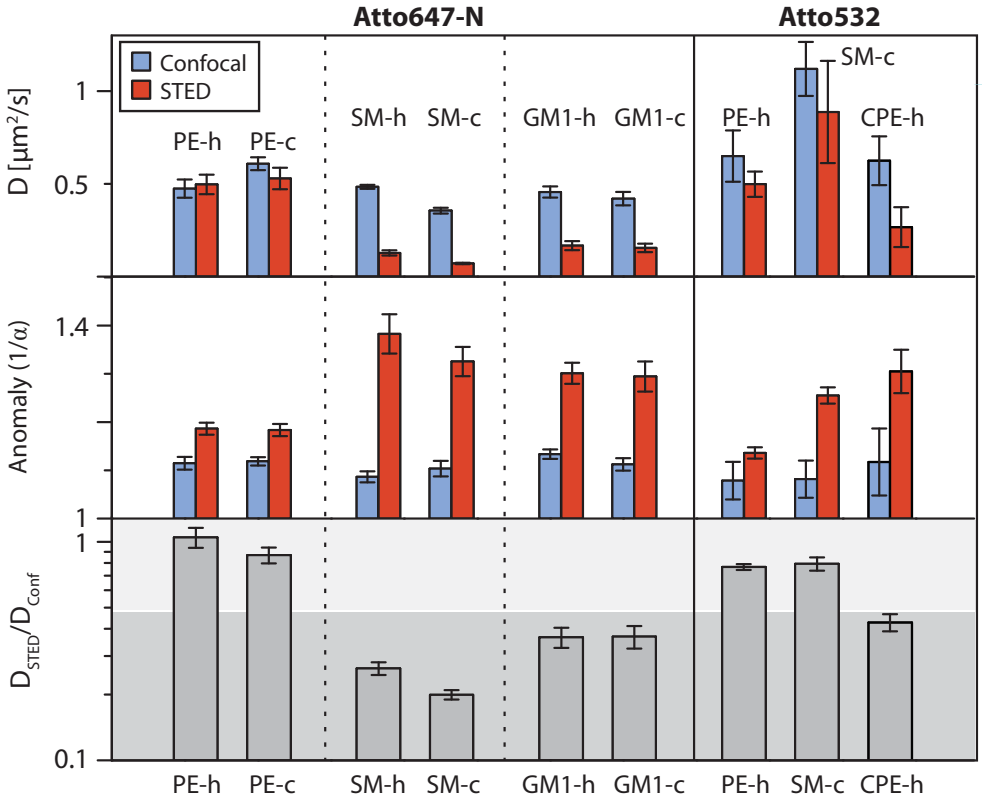

Figure 3.3.: Influence of the fluorescence labeling on diffusion dynamics: For the lipophilic dye Atto-647N, the diffusion dynamics of all lipids remain nearly unaltered for labeling positions at the head group (-h) or acyl chain (-c). For the polar dye Atto-532, no anomalous diffusion is observed especially for the chain labeled lipids, indicating an improper incorporation of the fluorescent lipid analog within the membrane.

the recorded diffusion coefficents and anomalies for a confocal and STED recording, as well as the ratio of the apparent diffusion coefficients for a series of different lipids.

First, we ensure that the fluorescent dye does not alter the diffusion properties of the fluorescent lipid analog. As depicted in figure 3.3, the diffusion of PE, SM and GM1 remains unchanged when we change the label position of the lipophilic dye Atto-647N labeling either the headgroup (-h) or replacing the acyl chain (-c). Yet, the labeling position is crucial for lipids labeled with polar hydrophilic dyes. For the polar dye Atto-532, we, for instance, find that all lipids diffuse freely. Since the diffusion time is significantly decreased for those lipids labeled at the acyl chain we conclude that acyl labeled hydrophilic lipids are not successfully incorporated into the lipophilic phase of the membrane but only loosely bound to the the membrane surface.

Next, we investigate the influence of the acyl chains on the diffusion dynamics by

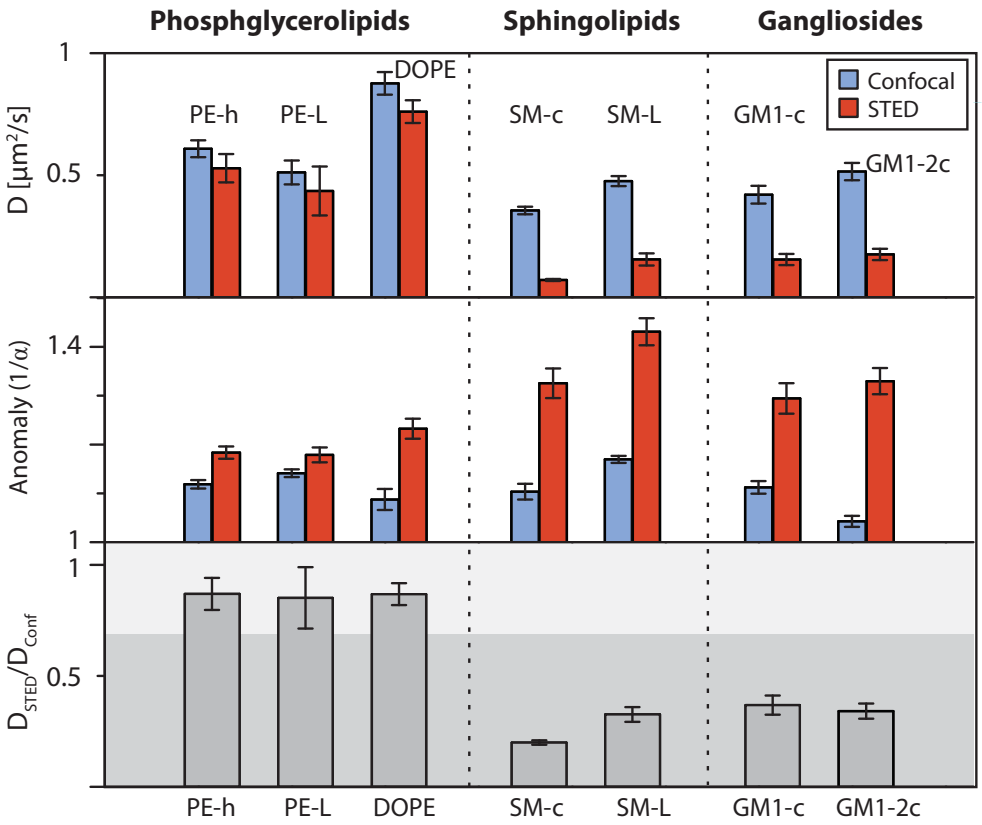

Figure 3.4.: Influence of the number and saturation degree of the acyl chains on the diffusion dynamics: The diffusion remains unaltered if the number of acyl chaines is decreased (lyso derivate, carrying one acyl chain (-L)) or increased ((GM1-c2) carrying two acyl chaines). Furthermore, the diffusion is not affected by an increase in the saturation degree (PE → DOPE).

varying the number and saturation degree of the acyl chains in the fluorescent lipid analog. As shown in figure 3.4, the lyso derivates (-L) of PE, SM and GM1 which only carry a single acyl chain show no significant alteration in the diffusion compared to the conventional lipids carrying two acyl chains. The diffusion is further not affected by the addition of an acyl chains as it was tested for a GM1 derivate (-c2) carrying the dye in addition to the two native acyl chains. Next, we evaluate the influence of the saturation degree of the fatty acids by comparing the diffusion of the unsaturated DOPE with the diffusion of the saturated PE. Even though the diffusion was observed to be faster for DOPE, the degree in anomaly was not affected. These observations suggest that anomalous diffusion is not induced by differences in the number or saturation degree of the acyl chains.

We therefore study the impact of the lipophilic backbone on the diffusion dynamics by comparing the diffusion properties of the glycerol-based phosphoglycerolipids

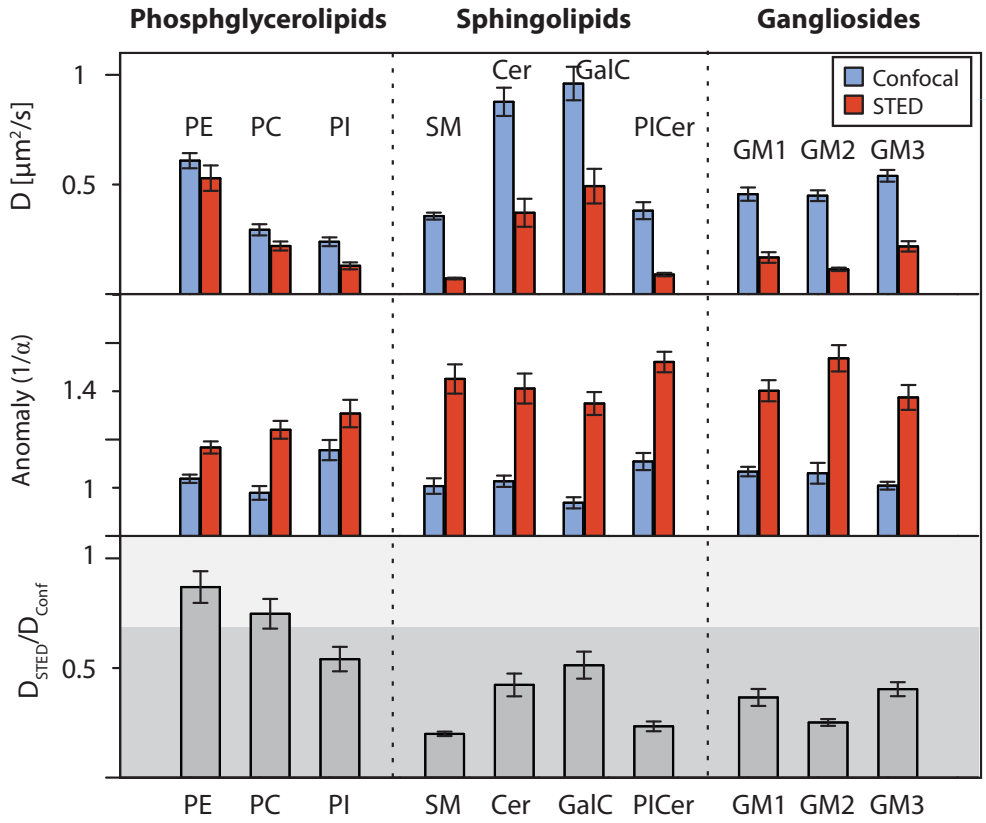

Figure 3.5.: Influence of lipophilic backbone on the diffusion dynamics of the lipids: The diffusion of the glycerol-based phosphoglycerolipids is rather free whereas the ceramide lipophilic backbone of sphingolipids and gangliosides induces anomalous confined diffusion. Large polar head groups are found to constrain the diffusion of phosphoglycerolipids (PI), but loosen the constrains for sphingolipids (GM1-3, GalCer, PI-Cer).

PE, phosphatidylcholin (PC), and phosphatidylinositol (PI) to those observed for the ceramide-based sphingolipids SM, ceramide (Cer), galactosylceramide (GalCer), GM1, GM2 and GM3. The phosphoglycerolipids, PE and PC diffuse freely whereas the diffusion is significantly constrained for PI carrying a large polar inositol-based head group as presented in figure 3.5. In the case of sphingolipids in contrast, we observe constraint and anomalous diffusion for all studied lipids. Comparing the constrained diffusion in more detail, we note that the degree of trapping for Cer and especially GalCer is slightly decreased compared to SM. Among the gangliosides the confinement was slightly stronger for GM2 than GM1 and GM3. In comparison to phosphoglycerolipids, an additional head group does not induce anomalous diffusion, but rather weakens the degree of confinement.

To evaluate the effects of the lipophilic backbone in more detail, we synthesize an

artificial lipid ceramide-phosphatidylinositol (CPI). CPI is identical to PI but based on a ceramide backbone. Interestingly, the degree of anomaly for CPI is significantly increased compared to PI. Quantitatively, the anomaly is in the range of the observed anomaly for GalCer carrying a galactosyl- instead of the inositol-based head group.

These findings confirm that molecular trapping is dominant for ceramide-based sphingolipids. In contrast to the glycerol backbone, the ceramide structure provides both a hydrogen-donor as well as a hydrogen-acceptor. The ceramide structure thus facilitates the formation of hydrogen bonds to endogenous membrane components, as for instance proteins or other lipids. Moreover, we find an additional effect based on to interactions of large polar head groups. Since trapping is increased for glycerol-based phosphoglycerolipids carrying a large polar head groups, but decreased for ceramide-based sphingolipids, we suggest that head group-induced trapping follows a supplementary mechanism independent of the trapping mechanism due to the ceramide structure of the lipid. For tightly trapped sphingolipids large head groups increase the intermolecular distances and thus loosen the confinement strength whereas the additional head group-induced interactions confine free diffusing phosphoglycerolipids.

3.2.2. Cholesterol dependence

As cholesterol is known to play a crucial role in the formation of lipid-dependent nanodomains, we study the dependence of the diffusion properties on the cholesterol contents within the plasma membrane.

First, we deplete cholesterol from the plasma membrane by treating the cells with cholesterol oxidase (COase) for 30 minutes. Measuring the diffusion of SM as shown in figure 3.6, we find that SM diffuse faster upon COase treatment. Furthermore, a comparison of the FCS diffusion law before and after the treatment reveals that especially the transient times at small observation areas are decreased. Overall, the FCS diffusion law approaches the linear dependence expected for a freely diffusing particle such as PE, indicating that cholesterol depletion weakens the molecular trapping of SM.

We repeat the experiment for the the previously studied fluorescent lipid analogs, and compare the effect of cholesterol depletion on the diffusion coefficients as well as the ratio $D_{\mathrm{ratio}} = D_{\mathrm{STED}}/D_{\mathrm{Confocal}}$ in figure 3.6. Here, we also calculate the effect of cholesterol depletion given by the recovery fraction

$$R = \frac{D^*_{\mathrm{ratio}} - D_{\mathrm{ratio}}}{D^*_{\mathrm{ratio}}}, \tag{3.1}$$

where D_{ratio} and D^*_{ratio} are measured before and after COase treatment, respectively.

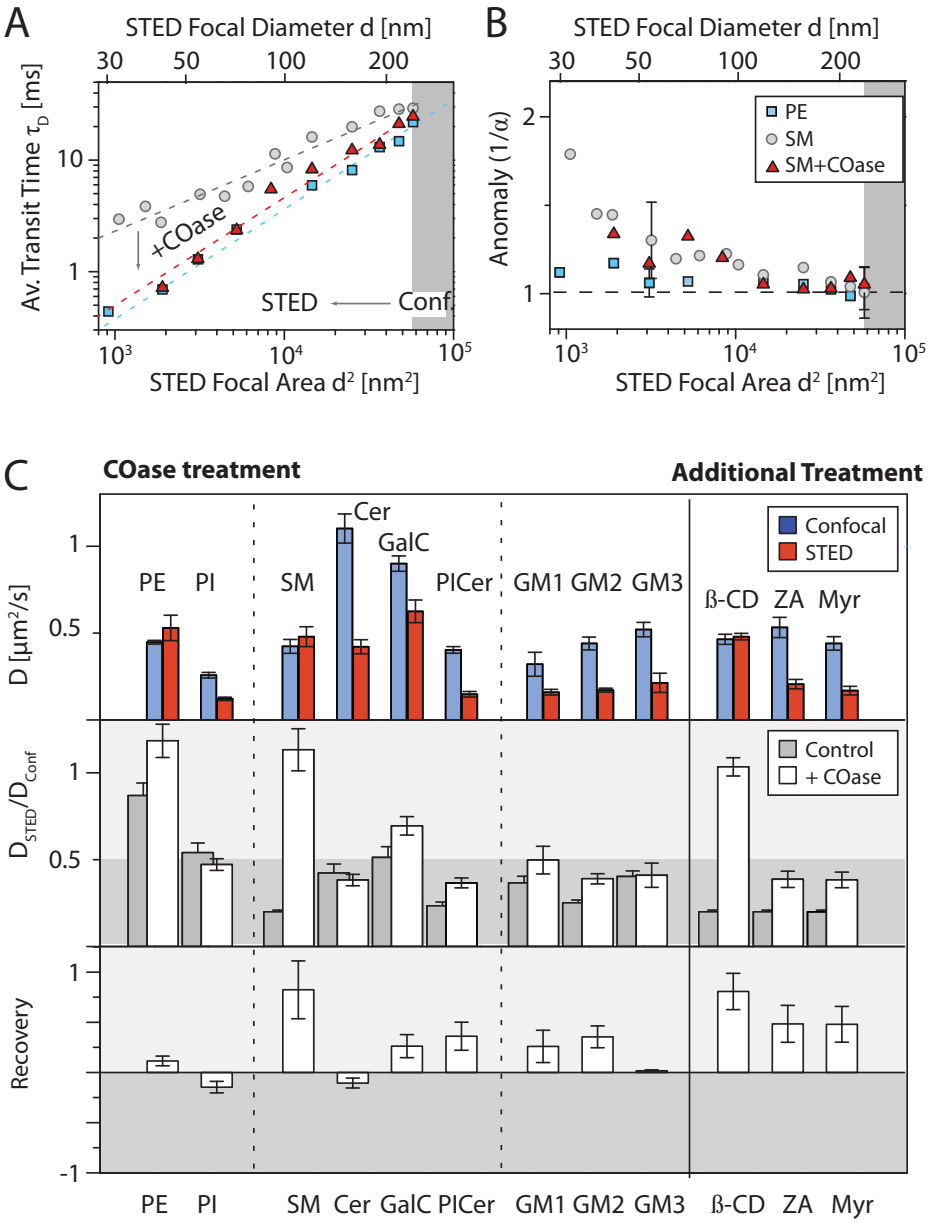

Figure 3.6.: Influence of COase treatment: (A) The average transient time for SM decreases (control: grey, +COase: red) and approaches the transient times recorded for the freely diffusing PE (blue). (C) At the same time, the anomaly remains unchanged ($1/\alpha > 1$). (C) COase treatment has no effect on the diffusion of phosphoglycerolipids, but decreases the extend of trapping observed for sphingolipids and gangliosides. The effect is less pronounced for those lipids carrying large polar head groups. The results for COase treatment are confirmed using alternative depletion protocols (β-CD, ZA, Myr).

For phosphoglycerolipids, on the one hand, no effect is observed after treatment with COase. This indicates that the free diffusion of lipids with a glycerol-based lipophilic backbone is hardly influenced by cholesterol depletion. Furthermore, the weak anomaly induced by large polar head groups, as observed for PI, is independent of the COase treatment.

For sphingolipids, on the other hand, cholesterol depletion significantly effects the diffusion characteristics. While the effect is especially pronounced for SM recovering almost free diffusion, trapping is less strongly reduced for GalCer and CPI, both carrying polar head groups. Similarly, the effect of cholesterol depletion is weaker for head group labeled SM-c and SM-l compared to the acyl chain labeled SM-c. We further note, that the diffusion of the gangliosides GM1-3 is only slightly effected by cholesterol depletion.

In conclusion, cholesterol depletion by COase treatment releases anomalous diffusion for ceramide-based lipids. Since the extend of the release is less distinct for those lipids carrying polar head group, the results confirm the assumption that anomalous diffusion is caused by two distinct mechanisms. While trapping induced by hydrogen bounds of the ceramide-based lipophilic backbone, as observed for SM, is highly dependent on cholesterol, only a weak effect is observed for a head group-induced confinement, such as GalCer, CPI and GM1-3.

Since COase treatment catalyzes the oxidation of cholesterol, but leaves the oxidized cholestenon within the bilayer, we repeat the experiment using alternative depletion techniques. First, we study the effects of β-cyclodextrin (β-CD), which directly extracts cholesterol from the membrane. In accordance to the results obtained for COase induced cholesterol depletion, treatment with β-CD releases the trapping observed for SM as shown in figure 3.6. Since β-CD, however, significantly alters the physiological structure of the cell (see figure 2.2), we repeat the experiment using Zaragozic acid (ZA), which depletes cholesterol by an inhibition of the sterol synthesis. As shown in figure 3.6, ZA decreases the extent of anomalous diffusion for SM, but has hardly any impact on the trapping observed for GM1. These results confirm the observations upon COase treatment. The recorded differences in the recovery degree between alternative depletion methods, might be explained by differences in the depletion efficiency which is difficult to assess quantitatively.

3.2.3. Cytoskeleton dependence

The plasma membrane of the cell is supported by the intracellular cytoskeleton which not only stabilizes the membrane but is also responsible for intracellular transport and cell mobility [19]. In the following, we therefore study, if a modification of the cytoskeleton affects the diffusion characteristics of lipids.

First, we focus on the impact of the actin-based cytoskeleton by treating the cells with Latrunculin B, which is known to inhibit the polymerization of the actin filaments and thus leads to a successively deconstruction of the actin-based network. Measuring the diffusion dynamics for SM, as shown in figure 3.7, we find that the nonlinear dependence of the transient times on the size of the observation area gradually approaches the linear dependence observed for PE. Increasing the incubation time of Latrunculin B from 5-30 minutes, the constrained diffusion of SM is successively released as indicated by the increase of the apparent diffusion coefficient and simultaneous decrease of the anomaly $1/\alpha$ shown in figure 3.7.

We repeat the measurement for the phosphoglycerolipids PE and PI, the sphingolipids SM-c, CPI and the ganglioside GM1. Comparing the obtained apparent diffusion coefficients for a confocal and STED recording in figure 3.7, we observe a partial recovery of free diffusion for SM with a slightly larger effect for the chain labeled SM-c compared to the head group labeled derivate SM-h. The diffusion of PI and CPI is hardly affected by the actin-based cytoskeleton. The confined diffusion of GM1 even appears to be further enhanced upon Latrunculin B treatment.

In order to confirm the observed effects, we alternatively treat the cells with Cytochalasin D. In analogy to the effect of Latrunculin B, Cytochalasin D induces a deconstruction of the actin filaments by inhibiting the polymerization process. After an incubation time of 30 minutes, the confinement of SM is partly released as observed during the Latrunculin B measurement. Next, the cells are treated with Jasplakinolide (Jaspl) which is known to stabilize or disrupt the actin filaments depending on the used concentration and intracellular environment [81]. Under the present experimental conditions, the recovery of the confined diffusion dynamics due to Jasplakinolide treatment is less pronounced for SM than in the in the previous experiments.

Finally, we evaluate the impact of the tubulin-based cytoskeleton by treating the cells with Nocodazol. Nocodazol is known to interfere with the polymerization of the tubulin-based network. As shown in figure 3.7, the deconstruction of the tubulin network only slightly releases the anomalous diffusion of SM. A recovery period of 24 hours after the treatment with Nocodazol allows to reverse the observed effect.

3.3. Discussion

Extending the observable range of lipid dynamics in the plasma membrane beyond the diffraction limit, STED-FCS reveals constrained diffusion of fluorescent lipid analogs at the nanoscale. The constrained diffusion is caused by the formation of short-lived, often cholesterol-assisted molecular complexes. Within theses complexes, lipids are

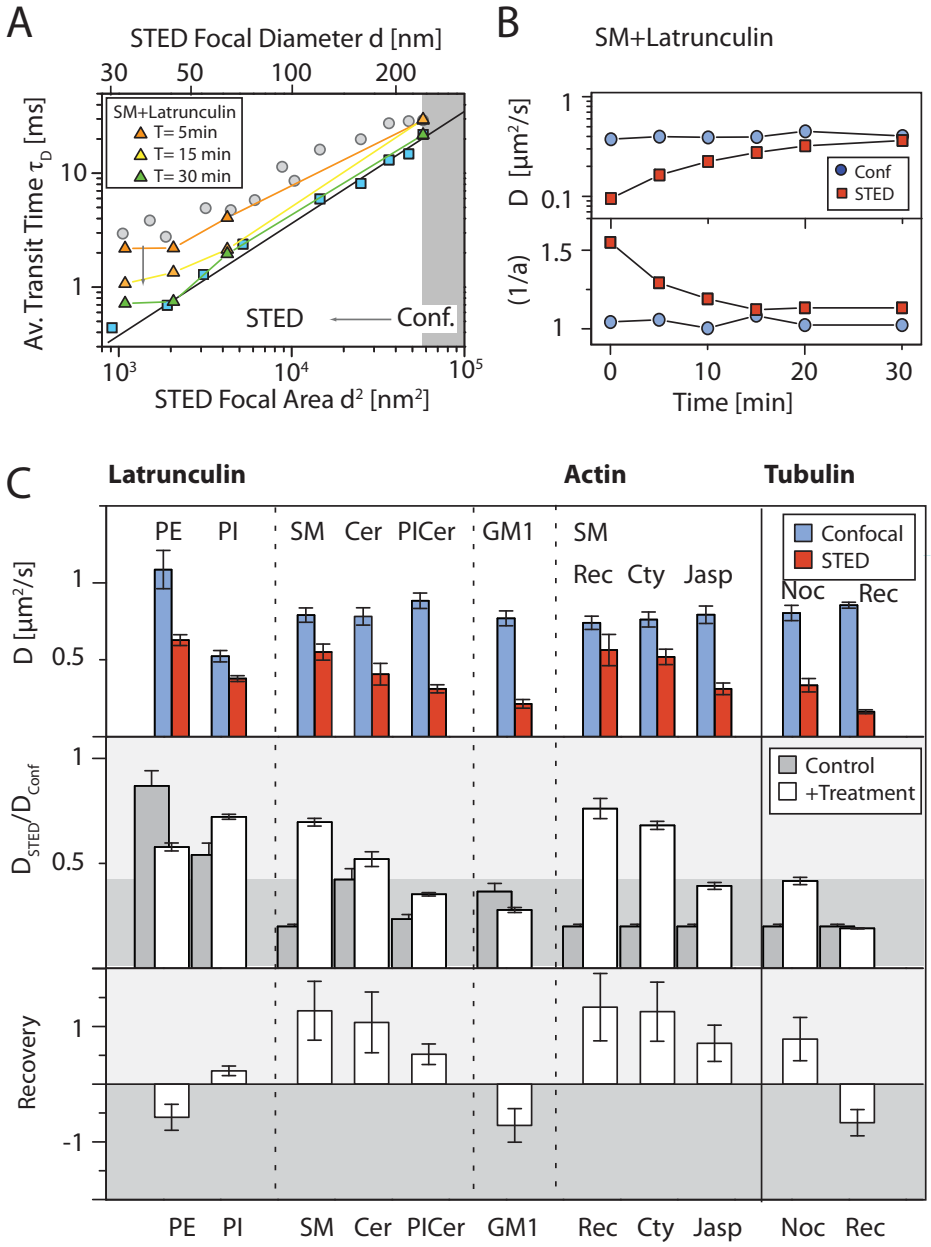

Figure 3.7.: Influence of the actin- and tubulin-based cytoskeleton on lipid dynamics: (A) Treating the cells with Latrunculin B, the average transient times observed for SM approach the free diffusion of PE as the incubation time is increased. (B) For an exemplary STED recording ($d = 40$nm), this effect is reflected in a gradual decrease of the anomaly $1/\alpha$ as well as an increase of the apparent diffusion coefficient with increasing incubation time. (C) While the diffusion dynamics of phosphoglycero- and sphingolipids carrying large polar head groups is less affected by Latrunculin treatment, the profound effect for SM is confirmed by alternative treatments with Cytochalasin D and Jasplakinolide. Partial disruption of the tubulin-based meshwork by Nocodazol treatment only slightly effects the diffusion dynamics of SM.

transiently slowed down or bound to immobile or comparably slowly moving binding partners.

The strength of the observed trapping is correlated to the chemical structure of the lipid: A ceramide-based lipidic backbone close to the lipid-water interface as well as large polar head groups lead to a confinement of the diffusion. Since both structures provide characteristic hydrogen donors and acceptors, we assume that the observed transient binding is induced by hydrogen bonding. Depleting the cholesterol from the membrane, we observe distinct differences between the molecular trapping due to both structures. The hydrogen-bounds formed by the ceramide moiety of the lipid, on the one hand, are close to the lipid water interface and are therefore stabilized by the presence of cholesterol. The hydrogen-bonding interactions of the large polar head groups, on the other hand, are situated within the water-water interface of the membrane and proved to be independent of the cholesterol contents within the cell membrane. Depending on the size and number of hydroxyl-groups in the head group, the molecular trapping mechanism was dominated by either ceramide- or head group induced interactions: large head groups, for instance, destabilize cholesterol dependent molecular trapping, but introduce additional confinement for glycerol-based lipids.

Furthermore, we observed subtle differences in the cholesterol affinity of different SM analogs: for SM-c with its large phosphocholine head group, we found that the confinement strength is larger than for SM-h and SM-L carrying smaller phosphatidylethanolamine head group. This findings are in line with previous experiments in model membranes which reported a higher cholesterol affinity of SM-c compared to SM-h and SM-L [92]. Accordingly, in our experiments, the diffusion of the ceramide analog carrying a single hydroxyl-head group appears to be less confined and independent on cholesterol depletion. This observation might explain the distinct biophysical characteristics of ceramide which was previously reported to significantly rearrange lateral organization of lipids in model membranes and to induce ceramide-enriched domains excluding cholesterol [93, 94].

Quantitatively, we find that the observed molecular complexes are characterized by transient binding events with on and off-rates in the range of (1/10ms). Assuming a free diffusion coefficient of $D = 0.4 - 0.6\mu^2/\mathrm{s}$, trapping events are observed approximately every 200-300 nm. During the trapping duration of $\approx$ 10ms, the lipids are either immobilized or move slowly with diffusion coefficients of $D < 0.01\mu^2\mathrm{m/s}$ in a confined area with sizes $< 20nm$). Possible binding partners for such a transient binding must therefore be immobile or move comparatively slowly as in the case of, for instance, cytoskeleton anchored proteins. A transient association to those proteins would further explain the observed dependence of the diffusion of SM on the actin-based cytoskeleton. The molecular specificities of the lipids may also indicate a nanoscopic molecular connectivity between lipids and proteins which may play an important role in a variety of cellular processes. Cellular growth, for example, has

been reported to be modulated by the binding of GM3 to the epidermal growth factor receptor [95, 96, 97].

Comparing our experimental findings to the concept of lipid rafts, our STED-FCS experiments support the idea of a formation of nanoscale membrane complexes by molecular interaction of specific membrane lipids. As it is proposed in the lipid raft model [30], our experiments indicate that those nanodomains are enriched in sphingolipids and that their formation is cholesterol assisted. Since the constrained diffusion of GM1 is, however, observed to be much less dependent on cholesterol, we assume that the molecular interactions of GM1 differ from those constraining the diffusion of SM. These additional cholesterol-independent molecular binding is assumed to be caused by head group interactions to other membrane constituents and might not be sufficiently explained within the lipid raft model. In the lipid raft model, the molecular interactions are often compared to the tight molecular packing of sphingolipids and cholesterol to the liquid-ordered phases in model membranes [25, 32, 44]. Even though the order parameter of the plasma membrane is substantially different from those observed in model systems, it is important to note that the fluorescent analogs used in our experiments is not enter the liquid ordered phase of model membranes. We are therefore not able to detect or rule out the existence of highly ordered nanodomains. Altogether, we, however, support that specific lipids interact according to the lipid raft hypothesis by the formation of 'fluctuating nanoscale assemblies of sphingolipid, cholesterol and proteins that can be stabilize to coalescence, forming platforms that function in membrane signaling and trafficking' [44]. We note, however, that the lipid raft concept does not provide a complete picture of the lipid diffusion which is further constrained by additional interactions. It further remains to be shown whether these nanoscale assemblies can be stabilized into densely packed domains as they are observed in the liquid- ordered phase of model membrane systems.

According to the proposed model of meshwork-based confinement, the cytoskeleton of the cell is assumed to act as a barrier for the free diffusion of lipids and proteins. Such a hop-like diffusion was previously reported for unsaturated lipids tagged with colloidal gold beads. The compartment size was determined to vary between 40 and 250 nm in diameter [98]. As discussed in section 1.3.2 a hop like diffusion results in a steep decrease of the FCS diffusion law for observation areas larger than the compartment size. Such an exponential like decrease is not observed for any of the investigated lipids. We note, however, that there is a possibility that hopping events through compartments with diameters larger than 250 nm are not accurately probed for with the nanoscale observation areas of our STED FCS measurements (< 250nm), but so far previous FCS measurement with larger focal areas could not collect any evidence for hop-like diffusion either [72].

4. Membrane dynamics of proteins

Proteins are apart from lipids the most abundant constituents within the plasma membrane. As they often comprise more than 50% of the membrane's molecular weight it is not surprising that they are commonly believed to be responsible for a majority of the functional processes associated to the membrane [23]. While receptor proteins for example play a key role in the transduction of extra- or intracellular signals, other important types of membrane proteins serve as ion channels and transporters or carry out a variety of enzymatic reactions. [19].

Even though the divers functionality of membrane proteins has been well characterized in the past, their diffusion dynamics and interaction with the surrounding lipids remains unclear [99]. In the following section, we will therefore study the diffusion dynamics of several representative examples of membrane proteins and explore how their dynamics are influenced by the lipid composition and structure of the membrane. Genetic mutations of the protein sequence further enable us to consider the role of palmitoylation, a post-translational lipid modification, on the dynamic behavior of an exemplary transmembrane protein.

4.1. Nanoscale diffusion of membrane proteins

In order to understand the diffusion dynamics of proteins within the plasma membrane, we study the diffusion behavior of four different proteins: a glycosylphosphatidylinositol (GPI) anchored protein, a single- and a multi-spanning transmembrane protein (LAT and MAL), as well as a receptor protein, the transferrin receptor (TfRc). These proteins are not only characterized by very distinct membrane topologies as shown in a schematic drawing in figure 4.1, they are also known for their specific partitioning into the raft-like liquid-ordered phases of model membrane systems [69]. Similar to the GPI-anchor, which is probably the best studied class of raft markers, the transmembrane proteins LAT and MAL are found to have a high affinity to the raft phase in model membranes. The transferrin receptor, in contrast, is strongly excluded from the raft-like liquid ordered phase and therefore generally referred to as a non-raft-marker.

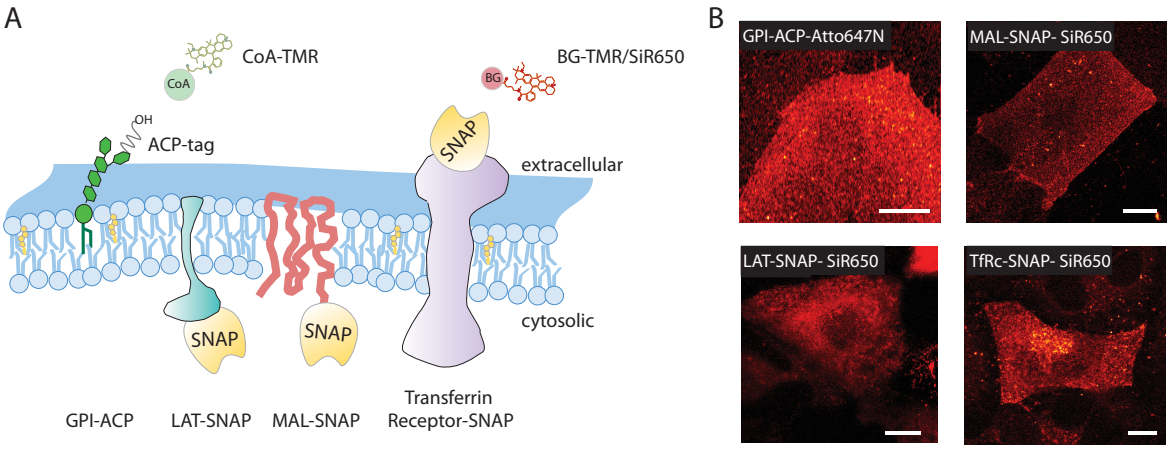

Figure 4.1.: Overview of genetically expressed fusion proteins and their membrane topology (A, from left to right): GPI-anchor fused to ACP-tag, single-spanning and multi-spanning transmembrane protein fused to SNAP-tag (LAT, MAL) and the transferrin receptor (TfRc) fused to SNAP-tag. Tags are labeled with CoA-TMR/Atto647N or BG/TMR/SiR650. (B) Corresponding protein staining in PtK2 cells (scale bar 10μm).

A specific fluorescent labeling was achieved by employing an advanced tag labeling technology. As described in [100], each protein is genetically encoded and expressed as a fusion protein which combines the protein of interest with an SNAP or ACP-tag protein. While the SNAP tag covalently binds to fluorescently labeled benzylguanine derivatives (BG), labeling of the ACP-tag relies on a enzyme-catalyzed reaction of Coenzyme A derivatives (CoA) in the present of the phosphopantetheinyl transferase AcpS. In dependence on the position of the tag structure, membrane permeable dyes such as TMR or SiR650 are used to label the cytosolic fraction of a transmembrane protein (see figure 4.1).

First, we determine the diffusion dynamics of the labeled proteins by recording the fluorescence intensity traces for various observation areas. Correlating the fluorescence intensity traces over time, we obtain the corresponding temporal correlations. These correlation curves are adequately described using the theoretical model for anomalous diffusion in equation 2.7 and directly provide us with the average transient time τ_T and the anomaly $1/\alpha$. Note, that for those proteins which are intracellularly labeled using membrane permeable dyes, the correlation curves are only be accurately fit if a second diffusive component is included into the theoretical model. This second component is characterized by short transient times of the order of $2\mu s$ and can be ascribed to the fast diffusion of unbound dye molecules within the cytosol. Although an additional washing procedure upon labeling decreases the contributions of the unbound dye molecules, it was rarely observed to decrease below an average fraction of ap-

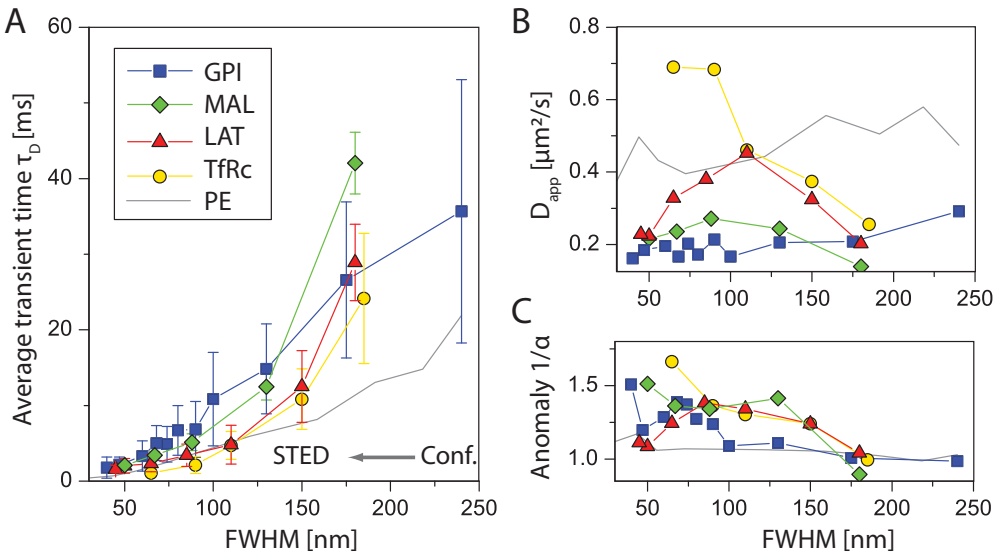

Figure 4.2.: Diffusion dynamics of membrane proteins in comparison to a freely diffusing lipid (PE, solid grey line): (A) While the average transient time shows the characteristic decay expected for a trap-like confinement for GPI (blue squares), the transmembrane proteins MAL, LAT and TfRc exhibit a steep initial decay ascribed to a meshwork-based confinement(green diamonds, red triangles, and yellow circles). (B+C) The apparent diffusion coefficient and anomaly $1/\alpha$ confirm the observed constrained diffusion and reveal further distinctions within the meshwork-based confinement of MAL, LAT and TfRc at small observation sizes.

proximately 30%. In the following experiments, we therefore determine the amplitude and diffusion time of the unbound fast diffusing component from a confocal recording. Considering the diffusion time of a freely diffusing molecule to decrease linearly with the observation area, the confocal results are used to fix the secondary fast component in the subsequent fits of the STED recordings.

In figure 4.2, the recorded average transient time τ_T and anomaly $1/\alpha$ are plotted as a function of the diameter of the observation area. We further use the average transient time τ_T to derive the apparent diffusion coefficient $D_{\text{app}} = \text{FWHM}^2/(8\ln(2)\tau_{\text{T}})$ for each observation area. In comparison to the previously discussed results for a freely diffusing lipid (PE, grey solid line), we observe that the confocal transient times are consistently longer for all proteins yielding approximately 1.5 - 4 times higher apparent diffusion coefficients. Among the studied proteins, the multi-spanning transmembrane protein MAL diffuses slower than the single-spanning LAT as well as the TfRc.

Next to the absolute differences in the transient time, the recorded decay of the transient time as a function of the observation size further reveals significant differences between the dynamics of the proteins and the freely diffusing lipid. On the one hand,

the GPI-anchored protein features a slow decay of the transient time for observation areas FWHM> 100 nm. The integral proteins (MAL, LAT and TFRc), on the other hand, are characterized by a step initial decrease of the transient time for large observation areas. At the same time, the anomaly $1/\alpha$ of all proteins increases for decreasing observation areas, indicating an increased extent of anomalous diffusion within small observation area. In combination with the non-linear decay of the transient time, we conclude that the investigated proteins do not diffuse freely within the membrane but are constrained on small length scales.

4.2. Exploring the origins of anomalous diffusion

In order to identify the underlying principles constraining the diffusion of these membrane proteins, the recorded transient times are analyzed in more detail. Since in the previous representation the differences in the observed transient times as a function of the observation size are especially difficult to resolve for small observation areas, we evaluate the characteristics of the apparent diffusion coefficient with regard to the diameter of the observation area as presented in figure 4.2.

In comparison to the constant apparent diffusion coefficient expected for the freely diffusing lipid (PE, solid gray line), the apparent diffusion coefficient for the GPI-anchored protein decreases with decreasing observation diameter. Such a decrease of the apparent diffusion coefficient was previously ascribed to an anomalous diffusion in the presence of transient molecular trapping. We note, however, that for GPI the decrease is less steep than the previously observed decrease of SM or GM1. For small observation areas FWHM$\leq$100 nm the apparent diffusion coefficient even converges against a constant value of $D_{\text{app}} \approx 0.17\mu^2/s$ indicating the observation of an in average unconstrained diffusion at small length scales. In comparison to SM and GPI, these observations suggest that the extend of transient binding for GPI is less pronounced due to either reduced trap frequencies or times.

Concerning the transmembrane proteins LAT, MAL and the TfRc, the apparent diffusion coefficients initially increase with decreasing observation diameter. Such a decrease of the diffusion coefficients is generally expected if the diffusion of the particle is constrained by semipermeable barriers of a regular meshwork. Decreasing the observation area, each particle needs to traverse less and less barriers on its passage through the observation area. As soon as the size of the observation area is of the order of the mean compartment size within the meshwork, the diffusion dynamics in average reflect the particle's free diffusion within the compartments as for instance observed for the TfRc in observation areas smaller than FWHM $\ll$ 100nm. In the case of the raft-associated proteins MAL and LAT, however, the apparent diffusion coefficients decrease for small observation areas and finally approach the values reported for the

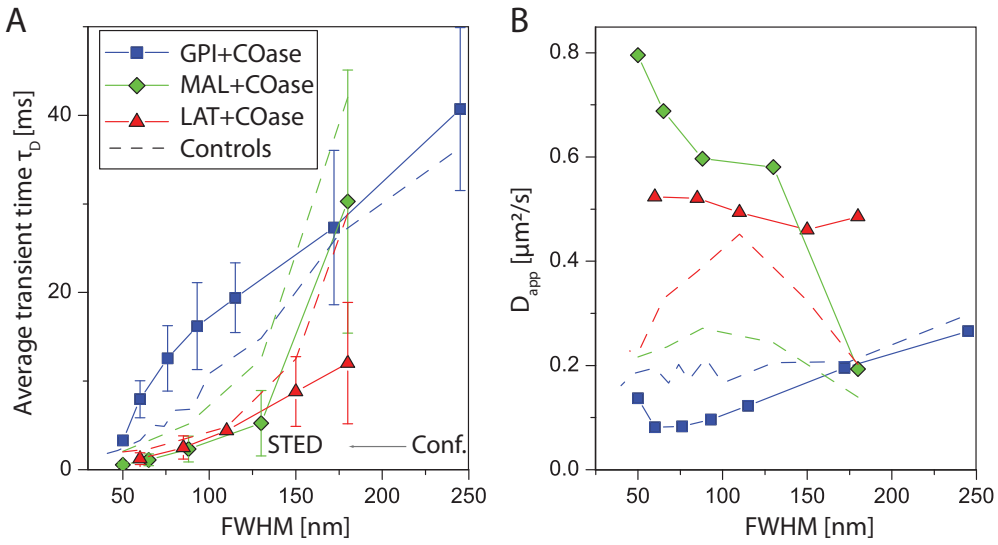

Figure 4.3.: Dependence of the diffusion dynamics on cholesterol depletion: (A) In comparison to a control experiment (dashed lines), the average transient times as a function of the observation area show distinct differences in the diffusion behavior of MAL and LAT upon cholesterol depletion (green diamonds, red triangles) while the characteristics of GPI remain unaltered (blue squares) (B) The apparent diffusion coefficients as a function of the observation size confirms these findings.

diffusion of the GPI-anchored protein. If we consider that such a decay of the apparent diffusion coefficient is typically associated with a trap-like confinement of the diffusion, these findings suggest that the diffusion of transmembrane proteins with a high raft affinity is effectively constrained by a combination of semipermeable barriers within an underlying meshwork as well as the formation of transient molecular binding events within trap-like nanodomains.

4.2.1. Cholesterol dependence

Since cholesterol was shown to significantly influence the diffusion of trap-like confined lipids in the previous section, we study the dependence of the diffusional properties on the cholesterol contents within the plasma membrane.

As described in section 2.1.4, we deplete the cholesterol from the plasma membrane by treating the cells with cholesterol oxidase (COase). Measuring the diffusion of the membrane proteins, we determine the diffusion characterisics presented in figure 4.3. The GPI-anchored protein diffuses slower upon cholesterol depletion, but conserves its overall diffusion dynamics as reflected in the unaltered characteristic decay of the apparent diffusion. Considering that the chemical structure of the lipid GPI-anchor

is based on a glycerol lipid backbone, these results indicate that the reported confinement of the GPI anchored protein is, in contrast to the molecular confinement of ceramide-based sphingolipids, independent of cholesterol. The observed confinement is rather comparable to the previously described molecular interactions due to hydrogen bonding between large polar head groups.

The diffusion dynamics of the studied transmembrane proteins MAL and LAT, are significantly increased upon cholesterol depletion. In addition to the faster diffusion, we note that the late decrease of the apparent diffusion coefficient is reversed for both proteins. This observation confirms our previous interpretation that the late decay in the apparent diffusion coefficient is caused by an additional trap-like confinement. Since the confinement appears to be facilitated by cholesterol we conclude that the diffusion of proteins with a high raft-affinity is confined by cholesterol mediated transient molecular interactions. Moreover, the additional hop-like confinement within the barriers of a meshwork is weakend upon COase treatment as indicated by a decrease of the steep initial slope for LAT. Since the cholesterol contents within the plasma membrane is unlikely to influence the structure of the underlying cytoskeleton, the observation may be attributed to a secondary side effect of COase which is known to partially alter the actin-based cytoskeleton as discussed in more detail in section 2.1.4.

4.2.2. Cytoskeleton dependence

As the interpretation of the diffusion behavior for the transmembrane proteins implies that the diffusion is confined within the barriers of a meshwork, we study in how far a deconstruction of the actin-based cytoskeleton influences the observed confinement.

As described in section 2.1.4, treating the cells with Latrunculin B inhibits the continuous polymerization of the actin filaments and eventually results in an effective degradation of the actin-based cytoskeleton. Recording the average transient times before and after Latrunculin B treatment, we deduce the apparent diffusion coefficients as presented in figure 4.4. In comparison to the control measurement (dashed line), we note, that the constrained diffusion of the GPI anchor remains unchanged upon Latrunculin treatment. The diffusion characteristics of the transmembrane proteins LAT and MAL are slightly affected by actin depletion as indicated by a minor increase of the apparent diffusion coefficient for large observation areas.

Following these results, the transmembrane protein specific confinement within the barriers of an underlying meshwork is weakened upon cytoskeleton disruption. We note that the characteristic initial increase of the apparent diffusion coefficient is not fully reversed. The incomplete release of the constrained diffusion may be due to the

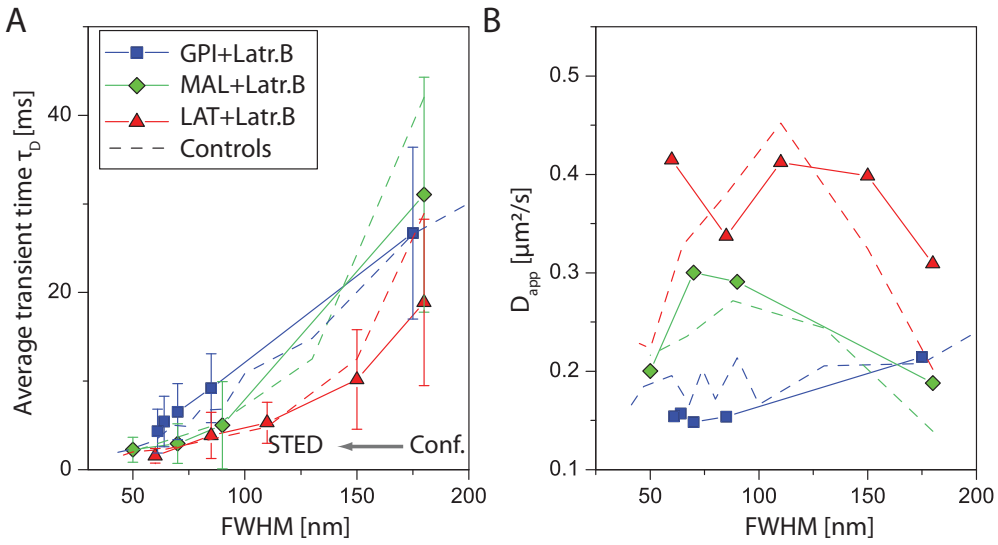

Figure 4.4.: Influence on the diffusion dynamics upon disruption of the actin-based cytoskeleton by Latrunculin B treatment: (A) In comparison to a control experiment (dashed lines), the average transient time as a function of the observation area shows distinct differences in the diffusion behavior of MAL and LAT upon Latrunculin B treatment (green diamonds, red triangles) while the characteristics of GPI remain unaltered (blue squares) (B) The apparent diffusion coefficients as a function of the observation size confirm these findings.

fragmentary disruption of the actin-based meshwork. Moreover, the diffusion might be additionally confined by remaining cytoskeleton components such as for instance tubulin, spectrin or the intermediate filament vimentin.

4.3. The role of post-translational palmitoylation

Post-translational modifications of membrane proteins are known to serve as an important tool to rapidly adapt the structure, targeting and functionality of specific proteins [101, 102].

A wide class of post-translational modifications includes the acylation of proteins with specific lipids, typically referred to as protein lipidation. Among the protein lipidations, the intracellular addition of a lipid anchor, such as the GPI anchor, is probably the most prominent example. These lipid-anchored proteins are often found to be further acylated to long saturated fatty acids such as palmitate (C16:0). In this specific palmitoylation process, a long palmitate chain is linked to the specific protein via S-acylation of a cystein residue as schematically depicted in figure 4.5. Similar

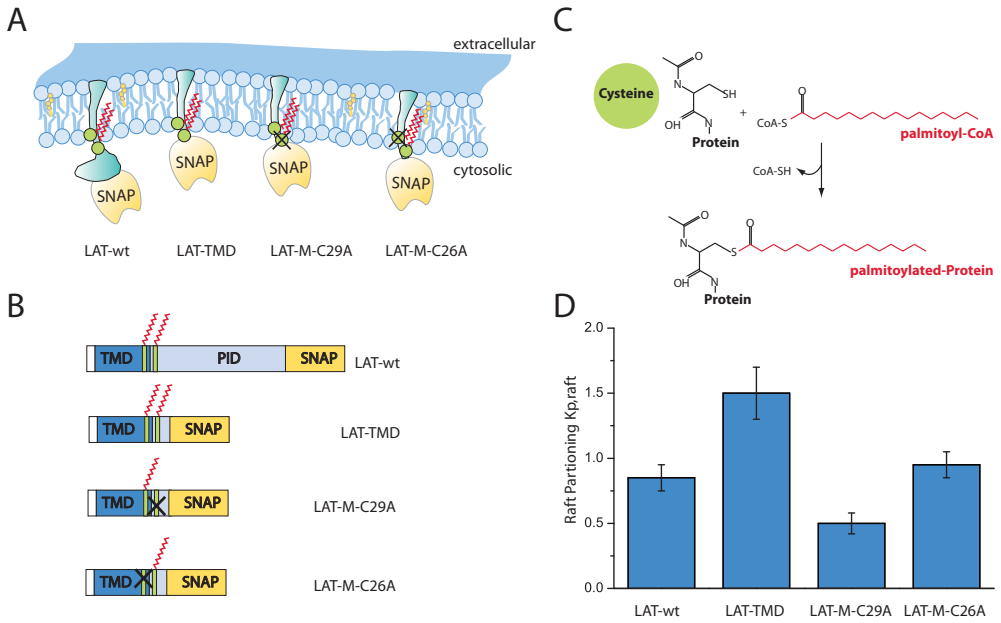

Figure 4.5.: Overview of studied LAT constructs: (A) Membrane topology of the wildtype LAT-wt, the truncated LAT-TMD and the cysteine mutations LAT-C29A and LAT-C26A. (B) Schematic representation of the constructs highlighting the palmitoylated cysteines (C26 and C29) (B, green lines) (C) Chemical reaction of palmitoylation via a cysteine residue of a protein. (D) Raft partitioning coefficient for LAT constructs (adapted from [103]).

to the stabilizing function of the lipid GPI-anchor, the additional palmitate-chain is described to target the linked proteins towards the plasma membrane and facilitate the stable integration therein. For small lipid anchored proteins, such as the members of the Src or Ras family, the additional stabilization of the palmitate-chain is well characterized and has further proven to be essential for the proper functionality of the proteins [104].

Similar to the post-translational modification of lipid-anchored proteins, even transmembrane proteins are frequently observed to be palmitoylated. Since these proteins are however intrinsically embedded within the membrane, the primary reason for palmitoylation remains unclear [105]. So far, first experiments suggest that an additionally attached palmitate-chain may alter the raft affinity of the transmembrane proteins, and is thus believed to potentially play a crucial role in the regulation of raft association [103]. In this context, it is especially important to emphasize that, in contrast, to the permanent attachment of a lipid anchor, the palmitoylation reaction is reversible and further found to be enzymatically controlled. The dynamic variation of the raft affinity for specific transmembrane proteins is therefore believed to regulate and initiate a variety of cellular processes, as for instance, in cell trafficking or

signaling processes [105].

Considering that a modification in the raft affinity of a protein generally goes along with an alteration of the specific lipid-protein interactions, the observed dynamic variation of the raft affinity raises the question in how far a post-translational lipid modification of a transmembrane protein leads to an alteration of its dynamical properties within the membrane. In the following section, we therefore vary the palmitoylation degree of a protein by genetic mutations in the primary structure of the protein. In particular, we study four different constructs of the single-spanning transmembrane protein LAT, which are schematically depicted in figure 4.5. Starting with the previously described wildtype LAT-wt, we crop the cytosolic fraction of the protein yielding the truncated LAT-TMD, which only comprises a short ectodomain, the transmembrane domain (TMD) and a truncated fraction of the cytosolic protein interaction domain (PID). To specifically address the degree of palmitoylation we further perform two individual point mutations of the principle palmitoylation sites in the LAT-wt. As presented in figure 4.5, the first palmitoylation site is associated to a cysteine residue within the TMD of the protein (C26), whereas the second cysteine is found in the truncated cytosolic domain in close vicinity to the plasma membrane (C29). Both cysteine residues are individually replaced by alanine resulting in two palmitoylation deficient mutants (LAT-C26A and LAT-C29A).

For all investigated LAT constructs, the raft affinity has been previously studied and quantified in terms of the raft partitioning coefficient

$$K_{p,\mathrm{raft}} = \frac{I_{\mathrm{raft}}}{I_{\mathrm{non-raft}}}. \tag{4.1}$$

Here, $K_{p,\mathrm{raft}}$ compares the average fluorescent intensity I of the tagged protein measured in the raft and non-raft phase of a phase-separated giant plasma membrane vesicles (GPMVs) [106]. As adapted form [103] in figure 4.5, the LAT-wt and truncated LAT-TMD both exhibit a strong raft affinity while the affinity is significantly decreased for the palmitoylation deficient mutants with an effective reverse of the raft association observed for the Lat-C26A mutant.

Figure 4.6 shows the measured diffusion dynamics for all LAT constructs. In comparison to the LAT-wt, we observe an overall decrease of the diffusion time for all mutants indicating a faster diffusion of the truncated LAT constructs. Calculating the apparent diffusion coefficient as a function of the observation size, the initial steep increase of the apparent diffusion coefficient is found to be less pronounced for the truncated LAT-TMD as compared to the LAT-wt. Since the initial increase was previously ascribed to a hop-like confined diffusion, this observation implies a slight decrease in of the confinement within the cytoskeleton meshwork. Regarding the palmitoylation deficient mutants, we note that a mutation of the cytosolic palmitoylation site (LAT-C29A) does not significantly alter the diffusion behavior of the mutant. The mutation

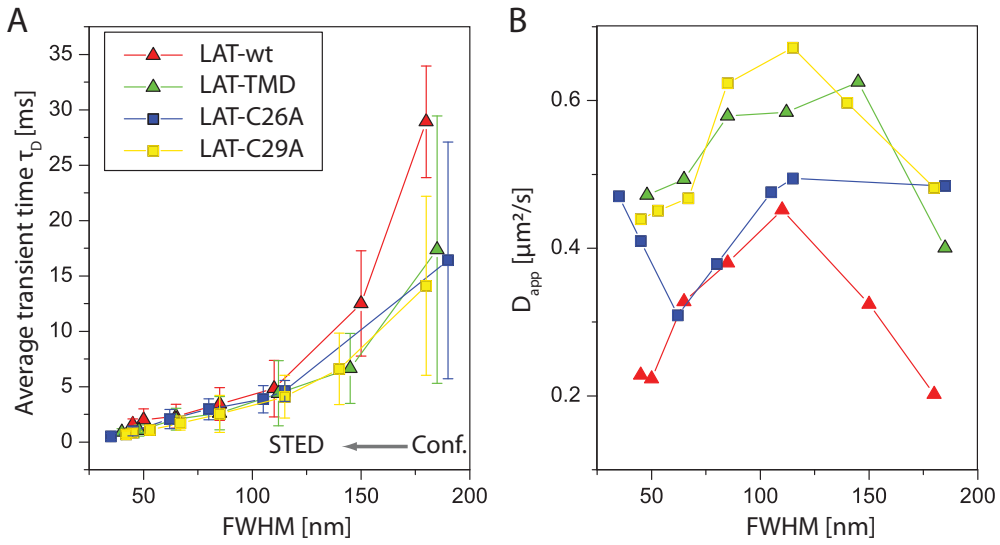

Figure 4.6.: Diffusion dynamics for genetically mutated LAT constructs: (A) In comparison to a wildtype (LAT-wt, red diamonds), the average transient time as a function of the observation area is significantly decreased for the truncated LAT mutants. (B) The apparent diffusion coefficients as a function of the observation size reveals no difference in the diffusion dynamics of the truncated LAT-TMD (green) and the LAT-C29A mutant (yellow), but implies that the constraints for the LAT-C29A mutant is weakened (blue).

of the cysteine residue in the transmembrane domain, in contrast, reveals a significant alteration of the diffusion dynamics and results in an approximately constant apparent diffusion coefficient. We note, however, that the measurements of the palmitoylation deficient mutants are experimentally challenged because of an increased fluorescent background. The increased background signal is mainly attributed to an intracellular fraction of the labeled LAT mutants which are not correctly targeted into the plasma membrane but remain bound in intracellular membranes of for instance the Golgi apparatus. Decreasing the signal to noise ratio the fluorescence background signal results in a wide variation of the experimentally determined transient times throughout the experiments, and thus impedes the quantification of the exact course of the apparent diffusion coefficient from the presented data set.

We therefore conclude that the truncated LAT mutants are observed to diffuse faster than the LAT-wt carrying a large cytosolic protein interaction domain. Upon truncation, the confinement of the diffusion is not significantly altered. For the palmitoylation deficient mutants, a point mutation of the cytosolic palmitoylation site does not affect the diffusion dynamics, whereas a similar mutation of the palmitoylation site within the transmembrane domain, appears to significantly influence the observed diffusion behavior and reduces the effects of both hop-like and domain-like diffusion constrains.

These observations are in line with the described differences in the partitioning behavior of the studied mutants which predict that the raft affinity is essentially reversed for LAT-C26A in comparison to the remaining LAT constructs.

4.4. Discussion

Observing the diffusion dynamics of membrane proteins, STED-FCS reveals constrained diffusion for GPI-anchored proteins as well as single or multi-spanning transmembrane proteins. Assessing the underlying diffusional constrains, we observe distinct differences within the different types of proteins.

On the one hand, the diffusion of the GPI-anchored protein is constrained by a transient association to mobile nanodomains which are assembled and disassembled dynamically and significantly reduce the mobility of the protein. Since the observed confinement is neither affected by cholesterol nor the actin-based cytoskeleton, we suggest that the molecular interactions are induced by specific hydrogen bounds between the oligosaccharidic head group of the GPI molecule and the surrounding membrane constituents. These observations are in line with the previously observed cholesterol-independent confinement of lipids carrying large polar head groups.

The transmembrane proteins, on the other hand, are found to corral within the semipermeable barriers of an underlying meshwork. For membrane proteins with high raft affinities, an additional molecular confinement of the diffusion is found to dominate the meshwork-constrained diffusion at the nanoscale. Upon actin- and cholesterol depletion both constrains are reduced indicating the fundamental importance of cholesterol and the actin-based cytoskeleton on the diffusion behavior of these transmembrane proteins. Genetically introduced mutations of the palmitoylation sites within the single-spanning transmembrane protein LAT, finally provide us with primarily evidence indicating that palmitoylation within the transmembrane domain not only alters the raft affinity of the protein but also effects its diffusion dynamics.

Throughout this section, the interpretation of the diffusion dynamics is based on a relative evaluation of the transient time and the apparent diffusion coefficient as a function of the observation area or size. In order to relate these qualitative observation to a quantitative determination of the underlying temporal and spatial scales of the constrains, we need to assess the effects of different confinement times or sizes on the observed transient times. In the following section, we therefore implement a specific Monte Carlo simulation to discuss the underlying constraints of the diffusion dynamics in more detail.

5. Simulations relate STED-FCS results to theoretical models of diffusion

In a typical STED-FCS experiment, we measure the transient time of a labeled particle for various observation areas. As shown in the previous sections, the dependence of the transient time as a function of the observation area allows us to differentiate the diffusion characteristics of different lipids and membrane proteins and provides us with valuable insights into the fundamental principles underlying the observed diffusion. Studying the influence of the chemical structure, cholesterol and the cytoskeleton structure on the diffusion dynamics, we are able to relate the observed diffusion dynamics to specific interactions between lipids, proteins and the cytoskeleton-based meshwork.

In order to confirm our qualitative observations, we perform a set of Monte Carlo simulations for different diffusion modalities and compare the results with our experiments. A systematic screening of the simulation parameters further allows us to quantify the confinement strength and estimate the size of putative lipid-dependent nanodomains or a compartment within the cytoskeleton.

5.1. Monte-Carlo algorithm

In the following Monte Carlo simulations, N particles are randomly placed in a simulation area of radius R as shown in figure 5.1. If not stated otherwise N is of the order of $N = 100$ particles and R is chosen to be at least three times larger than the largest focal area and typically of the order of $R = 3\mu$m. Over the course of the simulation time $T = 100s$, each particle is assumed to perform a stepwise random walk independently of the remaining particles. Starting from the initial random coordinates (x_0, y_0), the trajectory of the particle is calculated by determining the jump distance and direction to the next trajectory point at each time step $dt = 1 - 10\mu$s. For an unconstrained diffusing particle the jump distance $(\Delta x_n, \Delta y_n)$ at each step is given by

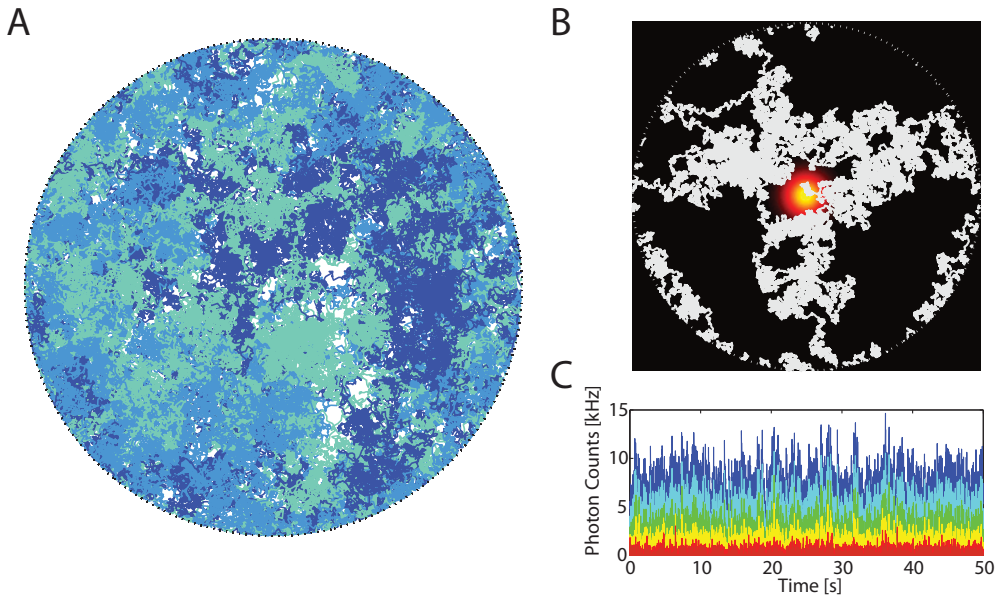

Figure 5.1.: Simulation principle: (A) We simulate the trajectories for N=3 particles within a simulation box of radius $R = 3\mu$m. (B) For each trajectory point the number of detected photons is calculated assuming a Gaussian illumination profile of the observation area. (C) Varying the size of the observation area, the number of detected photons is then used to determine the fluorescence intensity traces over time.

a set of two normally distributed random variables centered around 0 with a standard deviation of

$$\sigma_x = \sigma_y = \sqrt{2Ddt}, \tag{5.1}$$

where D denotes the diffusion coefficient of the particle. As soon as a particle leaves the simulation area, a new particle is randomly placed on the outer radius of the simulation area (see figure 5.1).

The simulated trajectories for each particle are then used to deduce the fluorescence intensity recorded during a STED-FCS experiment. At each time step dt, we first calculate the number of absorbed photons per particle $n_{\text{abs}} = I(x, y)\sigma_{\text{abs}}dt$, given by the absorption cross section σ_{abs} as well as the excitation intensity at each trajectory point (x, y). For a dye-specific fluorescence quantum yield q_f, the number of emitted photons is then derived according to $n_{\text{em}} = q_f n_{\text{abs}}$. Since the final detection process follows a Poisson distribution, the number of detected photons is given by a random number obtained from a Poisson distribution around the average number of detected photons $n_{det} = \beta q_D n_{\text{em}}$, where β denotes the detection efficiency and q_D the detector's quantum yield. In the following, we assume that the average number of detected

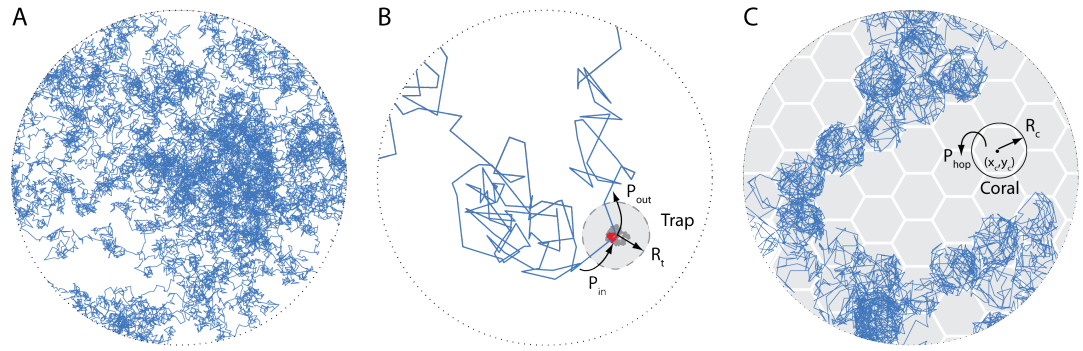

Figure 5.2.: Simulated models of diffusion: (A) Free diffusion. (B) Trap diffusion: A freely diffusing particle transiently binds to a trap center of radius R_t and follows the free slow diffusion of the trap center (gray). While the probability P_{on} determines the binding affinity, the probability P_{off} defines when the particle is released from the trap. (C) Hop diffusion: A particle diffuses freely within the boundaries of a compartment of radius R_c. Each time it reaches a barrier the probability P_{hop} determines whether the particles can cross the barrier or is reflected back into the compartment. The centers of the compartments are arranged within a periodic hexagonal lattice.

photons is of the order of $n_{det} = 10^5$ photons per second and that the observation volume is accurately described by a Gaussian intensity profile

$$I(x, y) = I_0 \exp\left(\frac{-2(x^2 + y^2)}{\omega_0}\right). \tag{5.2}$$

Here, I_0 corresponds to the excitation intensity at the center of the illumination profile while $\omega_0 = \sqrt{2 \ln 2}\,\mathrm{FWHM}$ denotes the beam waist of the focal spot as shown in figure 5.1. The obtained fluorescence intensity traces are finally correlated using a multiple-tau-correlator and the resulting correlation curves are fit with the previously described model of anomalous diffusion 2.7.

In order to simulate the effects of hindered diffusion, we study two different models of potential constraints as shown in figure 5.2: The particles are considered to be either transiently bound to a nanodomain or to corral within the barriers of a regular meshwork.

In the case that the particle is transiently trapped within a nanodomain, we assume M trap centers to be randomly distributed within the simulation area at the beginning of the experiment. Each trap center then diffuses freely with a diffusion coefficient D_{trap}, which is determined to be much smaller than the diffusion coefficient of the

freely diffusing particle. The trap centers are further associated to a trap area of radius R_t. As soon as a freely diffusing particle approaches the trap center closer than the trap radius R_t, a random number X is drawn and compared to the probability of transient binding P_{on}. If $X < P_{on}$ the particle is enclosed inside the trap while the particle is reflected back towards the previous trajectory point if $X > P_{on}$. In the case that a transient trap is formed, the trapped particle joins the diffusion of the trap center. At each subsequent time step dt, a random number then determines for a given probability P_{off} if the particle is released from the trap and resumes the free Brownian motion.

In the case of meshwork-based constrained diffusion, we assume that each particle diffuses freely within a circular barrier of radius R_c. When the particle reaches the border of the compartment, it traverses the barrier with a given probability P_{hop}. The particle then either jumps into an adjacent compartment or is reflected back towards the last trajectory point. We note that the compartments are organized in a hexagonal lattice as shown in figure 5.2. In order to avoid artifacts due to the position of the barriers within the focal area, the center coordinates of the initial compartment (xc, yc) for each particle are placed randomly within the simulation box. Consequently, the arrangement of the barriers within the observation area is unique for each particle.

5.2. Computational realisation

The Monte Carlo simulations are implemented in C and integrated via *mex*-functions in standard MATLAB routines.

In order to reduce the computational cost, each simulated trajectory is used to compute the fluorescence intensities for various beam sizes at a time. The sampling statistics is further increased by sequentially placing the focus on an equally spaced grid in the inner part of the simulation area and deducing the intensity trace at each grid point. This allows us to sample up to 36 intensity traces from one trajectory and proved especially useful in the case of constrained diffusion with fixed or slowly diffusing obstacles.

5.3. Simulation results

5.3.1. Free diffusion

First, we simulate the trajectories for freely diffusing particles and deduce the correlation curves for different observation areas. Figure 5.3 presents the simulation results

of five individual simulation runs (solid lines) as well as the average correlation curve (open circles) and the corresponding fit using the theoretical model of anomalous diffusion (black line, see caption for further details on simulation parameters).

As expected, the amplitude of the observed correlation increases for decreasing observation areas ([red,blue] $\rightarrow$ FWHM= $[25, 250\text{nm}]$) . At the same time, the apparent transient time decreases linearly with the observation area yielding a constant apparent diffusion coefficient $D = \text{FWHM}^2/(2\ln(2)\tau_\text{D})$. The observed anomaly $1/\alpha$ is of the order of 1, but slightly decreases from 1 to 0.98 for large observation areas. This slight decrease in the anomaly can be ascribed to an insufficient simulation time which leads to an inaccurate deviation of the correlation curve for large lag times and large focus areas.

Yet, the obtained simulation results are in agreement with the experimental results for phosphatidylethanolamine (PE) in PtK2 cells. For small observation areas, the experimentally determined transient times are slightly longer as reflected in the slight decrease of the apparent diffusion coefficient. Since the anomaly of the experimental measurements is also observed to increase for small observation areas, the deviation of the experimental data to the simulation results might be explained by a weak hindrance of the diffusion for PE within the plasma membrane.

5.3.2. Trapped diffusion

Next, we study the effect of a nanoscale confinement on the diffusion of a particle. First, we assume that each particle diffuses freely within the simulation area until it approaches the center of the trap within a radius of $R_t = 10nm$. The particle then transiently binds to the trap and follows the diffusion of the trap center. In the following simulation steps, the off-probability (P_off) determines if the particle is released from the trap. Note, that in a first approximation, we assume that each particle is trapped every time it passes a trap ($P_\text{on} = 1$).

In our simulations, we first study the extend of trapping observed for different trap densities and off-probabilities. As shown in figure 5.4 the fraction of trapped particles as well as the number of trapping events per second depend on both the trap density as well as the off-probability. The trap time during which a particle remains bound to a trap center, in contrast, is only determined by the off-probability. In more detail, we find that the dependence of the trap time on the off-probability is accurately described by

$$t_\text{trap} = A\,\frac{1 - P_\text{off}}{P_\text{off}} + dt, \tag{5.3}$$

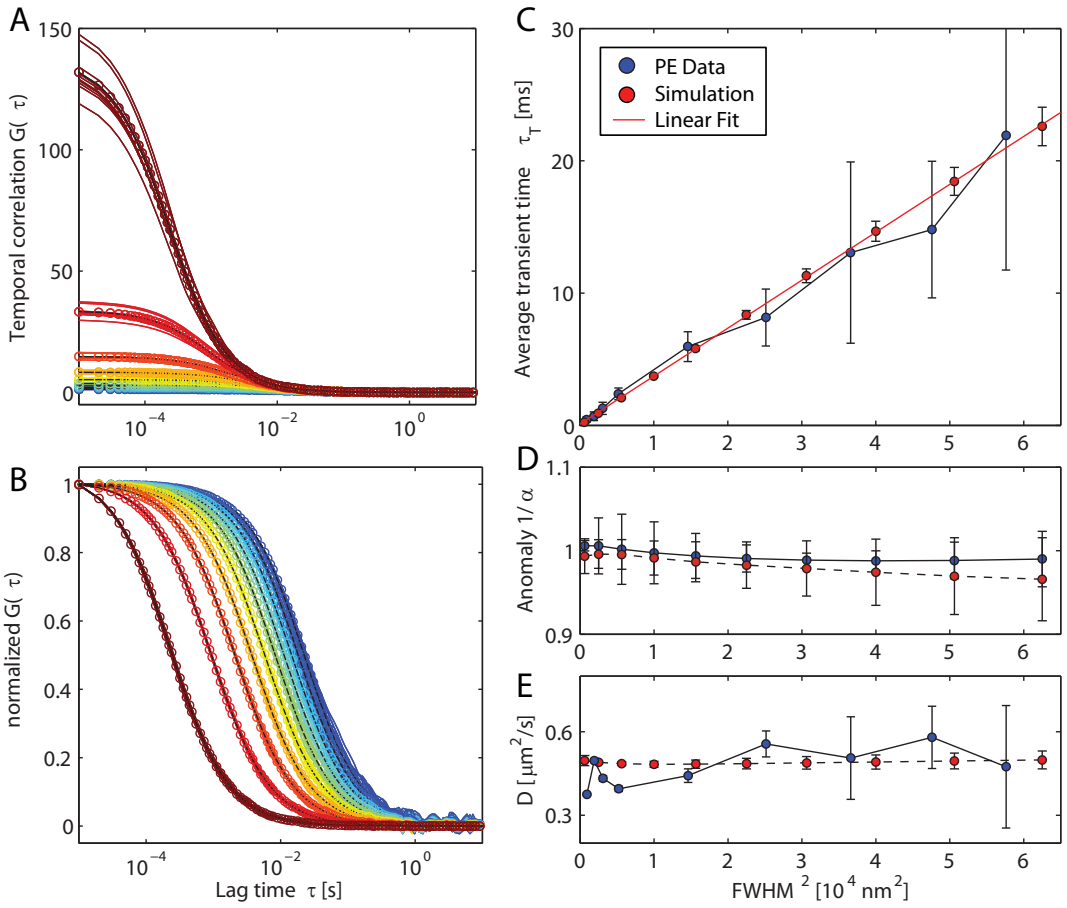

Figure 5.3.: Free Diffusion: (A+B) Simulated correlation curves of a freely diffusing particle for different observation areas in the range of FWHM= $[25, 250$ nm] (open circle: average of 5 individual simulation runs (solid colored lines)). The fit of the correlation curves (solid black line) provides the average transient time (C), the anomaly $1/\alpha$ (D) and allows us to calculate the apparent diffusion coefficient D. The fit results are compared to the previously described experimental results of PE in cells (blue dots). Simulation parameters: $T = 100$s, $N = 100$, $D = 0.7\mu\text{m}^2/\text{s}$, $R_{\text{sim}} = 2\mu$m.

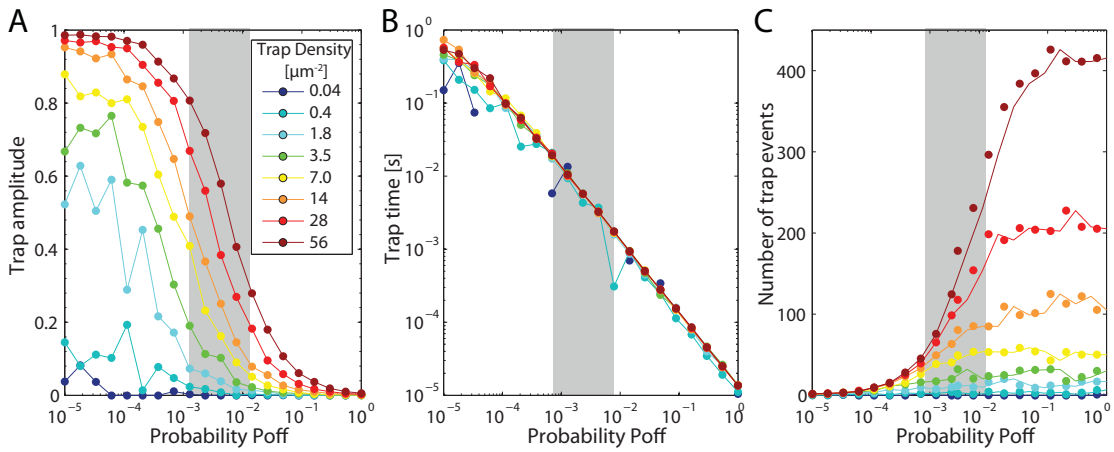

Figure 5.4.: Confinement Strength: The fraction of trapped particles (A), average trap time (B) and number of trap events (C) are shown in dependence on the off-probability for various trap densities in the range of 0.04 - 56 traps per μm^2.

and converges against the unit of the time step $dt = 10^{-5}$ for $P_{\text{off}} = 1$ [71]. The variable A can be determined by fitting the simulated trap times for a given trap density of $\rho_t = 60\mu m^{-2}$ as presented in figure 5.5 (solid black line, $A = 1.41$, $R^2 = 0.99$).

If we now correlate the simulated intensity traces for different off-probabilities, we observe that the obtained correlation curves are shifted towards longer lag times τ with decreasing off probability (see figure 5.5). Fitting the obtained correlation curves, this shift results in an increase of the determined transient times for decreasing off-probabilities. At the same time, we note that especially for small observation areas, the shape of the correlation curve deviates significantly from the shape expected for a freely diffusing single species. This deviation leads to an increase of the anomaly $1/\alpha$ for FWHM$< 150nm$ and $P_{\text{off}} < 0.02$.

In order to explain these observations, we consider the average transient time τ_T to be given as a combination of the particle's diffusion time τ_D and the average time τ_{trap} during which the particle is trapped on its passage through the observation area. Assuming that the particle is trapped n times within the observation area, the average transient time is given by

$$\tau_T = \tau_D + n\tau_{\text{trap}}. \tag{5.4}$$

Since the diffusion times through a confocal observation area are of the order of 20ms, we expect the transient times to be significantly increased for off-probabilities $P_{\text{off}} \approx 0.01$ and average trap times in the ms range of $\tau_{\text{trap}} \approx 10ms$. The previous simulation of free diffusion proved that the diffusion time τ_D decreases linearly with the observation area. The trap time τ_{trap}, in contrast, is independent from the size of the observation area and we therefore expect the transient times to be dominated by

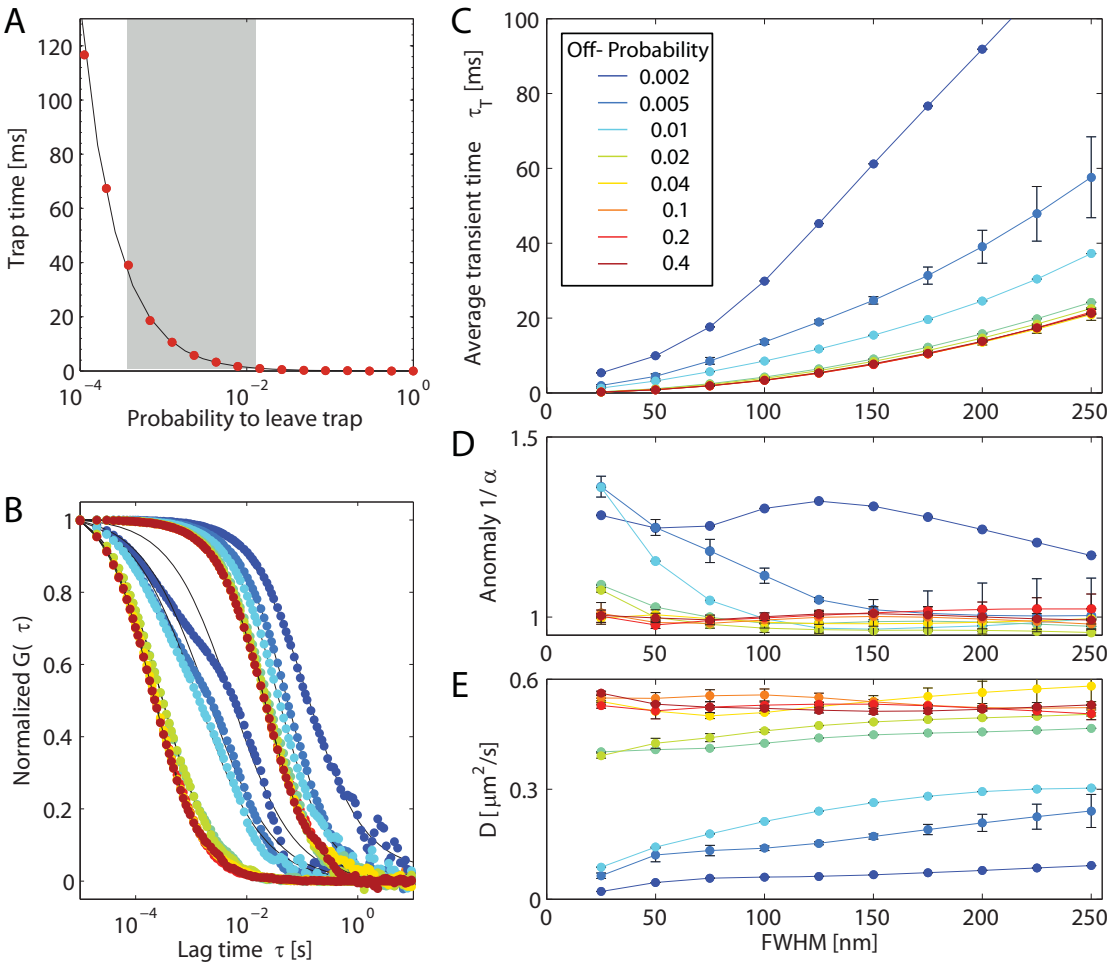

Figure 5.5.: Trap Diffusion: (A) Trap time as a function of the probability for a trapped particle to leave the trap (red dots) + fit to theoretical model (black solid line). (B) Simulated correlation curves for a particle trapped with decreasing off-probabilities for a confocal and nanoscale observation area (open circle: average of 3 individual simulation runs). The fit of the correlation curves (solid black line) yields the average tranisent time (C), the anomaly $1/\alpha$ (D) and allows us to calculate the apparent diffusion coefficient D (E). Simulation parameters: $T = 100$s, $N = 100$, $D = 0.7\mu\text{m}^2/\text{s}$, $R_{\text{sim}} = 2\mu\text{m}$, $\rho_t = 60\mu m^{-2}$.

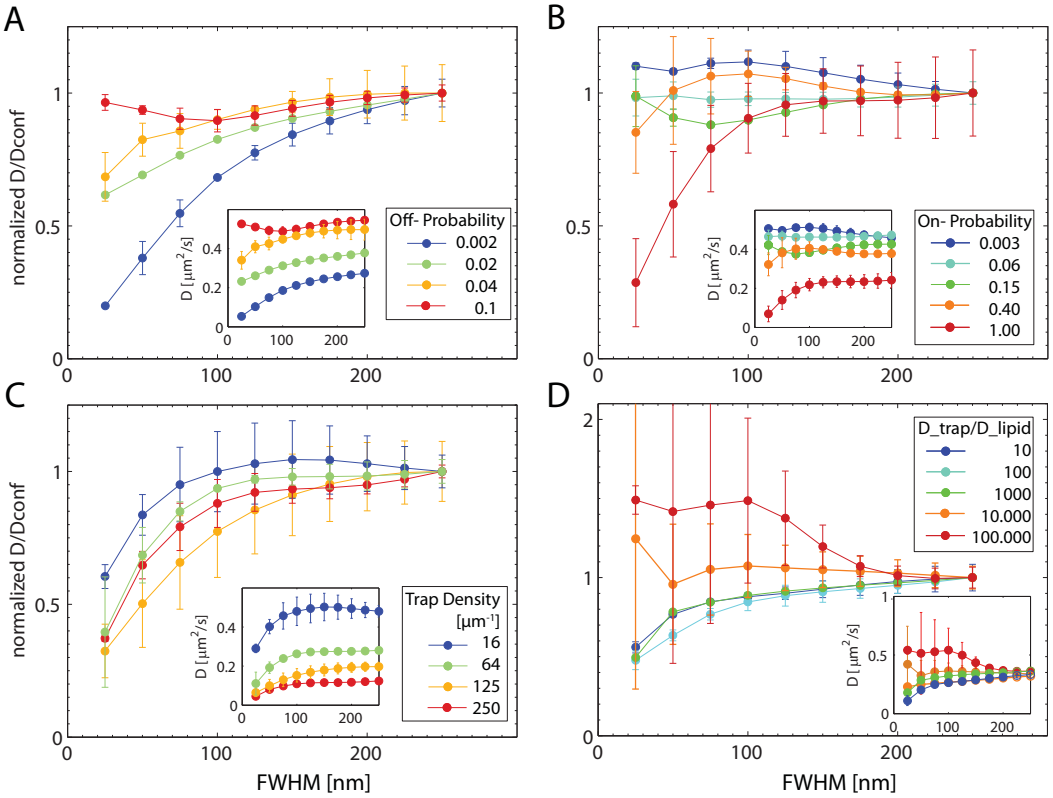

Figure 5.6.: Dependence of the normalized diffusion coefficient on the off-probability (A), the on-probability (B), trap density (C) and diffusion coefficient of the trap center (D). See insets for absolute diffusion coefficients. Simulation parameters if not stated otherwise: $T = 100$s, $N = 100$, $D = 0.7\mu$m^2/s, $R_{\text{sim}} = 2\mu$m, $P_{\text{on}} = 1$, $P_{\text{off}} = 0.01$, $\rho_t = 60\mu m^{-2}$, $D_{\text{trap}}/D_{\text{lipid}} = 1000$.

the trap time τ_{trap} for small observation areas. This disproportional increase of the transient time leads to an effective decrease of the apparent diffusion coefficient as it is observed for FWHM$<$ 100nm. Moreover, the predominance of the trapped fraction directly explains the reported increase in the anomaly for small observation sizes.

In the following, we evaluate in how far the obtained simulation results are affected by a variation of the simulation parameters. As previously discussed a decrease in the off-probability prolongs the trap time and therefore increases the extend of trapping. This effect is reflected by a significant decrease of the apparent diffusion coefficient for smaller off-probabilities as seen in the inset in figure 5.6. Furthermore, we observe that the bend of the normalized apparent diffusion coefficient D(FWHM)/D(Conf) is slightly shifted for small off-probabilities. This observation indicates that for small off-probabilities the long trap times predominate the free diffusion of the particle already within a large observation areas around FWHM$\approx$ 200nm. Similarly, we observe that

decreasing the on-probability results in a reduction of the trap extend as well a shift of the bend observed in the curve of the normalized diffusion coefficient. An increase of the trap density for a given off-probability, in contrast, merely results in an increase of the trap extend but leaves the overall dependency of the normalized apparent diffusion coefficient unaltered.

Finally, we study the impact of the additional diffusion of the trap center on the diffusion dynamics of the trapped particle. If the diffusion of the trap center is 10-1000 times slower than the diffusion of the freely diffusing particle, the additional movement is negligible during the comparable short trap times of 10ms. If the diffusion of the trap center is however more than 10.000 times slower than the free diffusion, the movement of the trap center is negligible during the complete simulation time of $T = 100$s. Thus the distribution of the trap centers within the observation area can be considered to be fixed in the course of a simulation run. The observed diffusion dynamics differ significantly between subsequent simulation runs. Consequently, the determined normalized diffusion coefficients are characterized by large standard deviations. Especially for small observation areas, we observe a rapid increase of the normalized diffusion coefficient which is explained by simulation runs with no or only few traps in the center of the observation area. In the course of a simulation run, a moderate diffusion of the trap center ($D_{\text{trap}}/D_{\text{lipid}} \approx 1000$) therefore ensures an in average uniform trap distribution within the observation area without altering the diffusion dynamics of the particle.

5.3.3. Hop diffusion

In the following simulations, the particles are considered to diffuse freely within a regular meshwork of compartments with radius R_c. Every time a particle reaches the barrier of a compartment the probability P_{hop} determines if the particle can cross the barrier or is reflected back into the compartment.

Comparing the average time τ_{hop} for which a particle is confined within a compartment to the time a freely diffusing particle would in average need to diffuse through the compartment area we can quantify the strength of the confinement S according to [107]

$$S = \frac{\tau_{\text{hop}}}{\tau_{\text{free}}} = A \frac{\Delta x}{R_c} \frac{1 - P_{\text{hop}}}{P_{\text{hop}}} + B. \tag{5.5}$$

Here, $\tau_{\text{free}} = (2R_c)^2/4D$ corresponds to the time which a freely diffusing particle needs in average to traverse an area of radius R_c while Δx denotes the average jump distance of the particle at each simulation step dt. The variables A and B can be determined by a fit of the simulated confinement strength and their value is found to depend on

the definition of τ_{free}. For a given compartment radius of $R_c = 80$ nm, the simulated confinement strength for increasing hop-probabilities is in well agreement with the theoretical model (see figure 5.7, $A = 13$, $B = 0.5$, $R^2 = 0.97$).

Correlating the simulated intensity traces for varying off-probabilities, we observe that the correlation curves for large observation areas with FWHM$>>$ R_c are shifted towards longer lag times τ whereas the correlation curves for small observation areas with FWHM$<<$ R_c are hardly influenced by the meshwork-constrained diffusion. This observation is confirmed by plotting the obtained fit results as a function of the diameter of the observation area. As shown in figure 5.7, the fit results can be divided in three different regimes. For large observation area FWHM$>>$ R_c, the simulated transient times decrease linearly with the observation area, yielding a constant apparent diffusion coefficient. In combination with the observed anomaly of $1/\alpha \approx 1$, the constant diffusion coefficient therefore suggests that the measured diffusion represents an average of the confined diffusion across multiple compartment and resembles the diffusion of a freely diffusing particle with an reduced apparent diffusion coefficient. As the observation size is decreased ($2R_c >>$FWHM$>>$ R_c), the apparent diffusion coefficient increases rapidly, since the particle traverses less and less barriers on its passage through the observation area. At the same time, the anomaly of the diffusion increases and reaches its maximal value around FWHM$=$ R_c. For observation areas smaller than the compartment size FWHM$<<$ R_c, the apparent diffusion coefficient finally approaches the apparent diffusion coefficient for a freely diffusing particle within the compartment.

Varying the size of the compartment R_c for a given hop-probability $P_{\text{hop}} = 0.01$, the same diffusion characteristics are observed within the three different regimes (see figure 5.8). Since the confinement strength S of the diffusion, however, scales with the compartment radius according to equation 5.3, the effect is less pronounced for large R_c. In figure 5.9, we therefore compare the apparent diffusion coefficients simulated for various compartment sizes R_c while keeping the confinement strength $S \propto A/R_c + B$ constant. In this representation, we observe that the rapid increase of the apparent diffusion coefficient for decreasing observation areas always begins in the range of FWHM$\approx$ $2R_c$ (gray area). If we decrease the hop-probability, the increase of the diffusion coefficient occurs around the same size of observation area, but is found to be less steep for small hop-probabilities.

5.4. Discussion

The implemented Monte Carlo algorithm simulates the diffusion of a fluorescent particle and derives the recorded fluorescence signal from an observation area of variable size. Correlating the fluorescence intensity traces, we determine the average transient

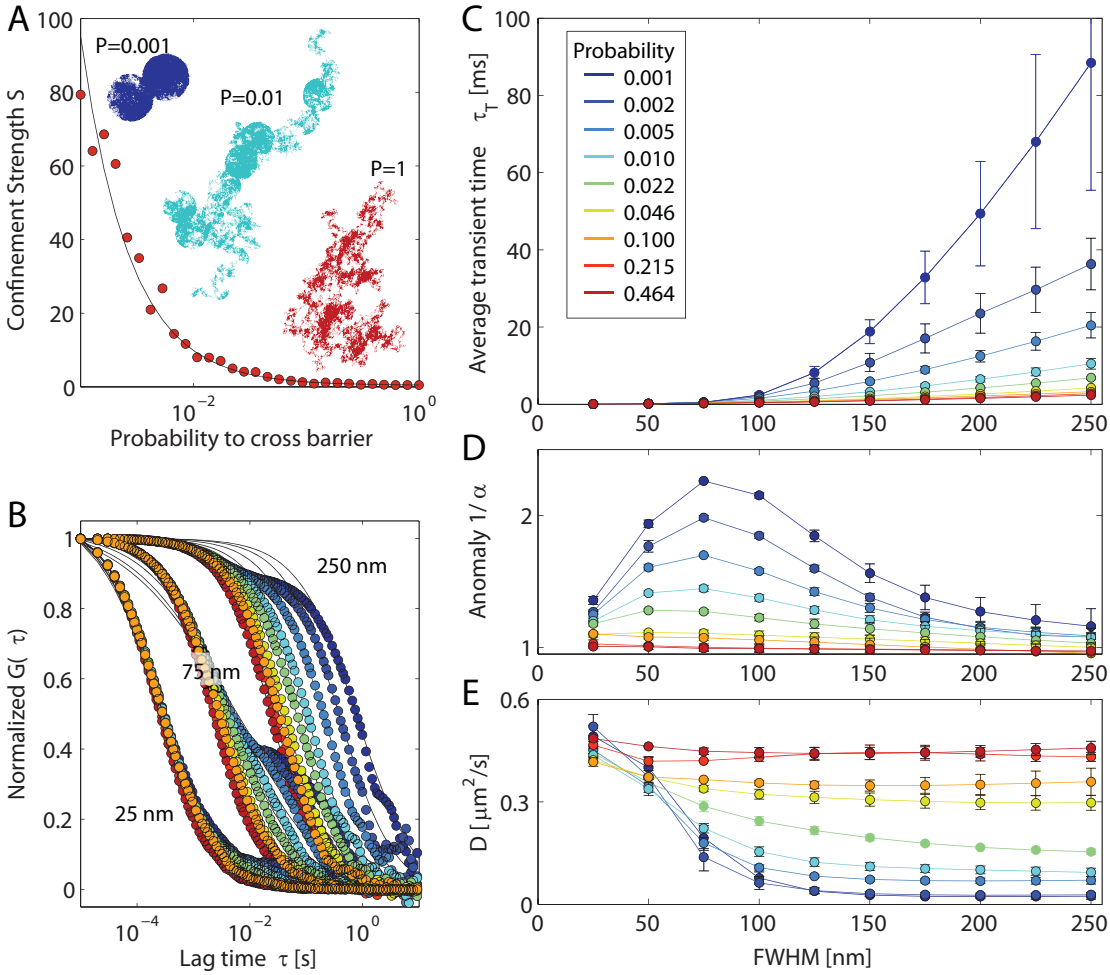

Figure 5.7.: Hop diffusion for varying hop probabilities and $R_c = 80$nm. (A) Confinement strength as a function of the probability to cross the barrier of a compartment (red dots) and fit to theoretical model (black solid line). (B) Simulated correlation curves for increasing hop-probabilities and three different sizes of the observation FWHM (open circle: average of 3 individual simulation runs). The fit of the correlation curves (solid black line) yields the average transient time (C), the anomaly $1/\alpha$ (D) and allows us to calculate the apparent diffusion coefficient D (E). Simulation parameters: $T = 100$s, $N = 100$, $D = 0.7\mu\text{m}^2/\text{s}$, $R_c = 80\mu$m, $R_{\text{sim}} = 2\mu$m.

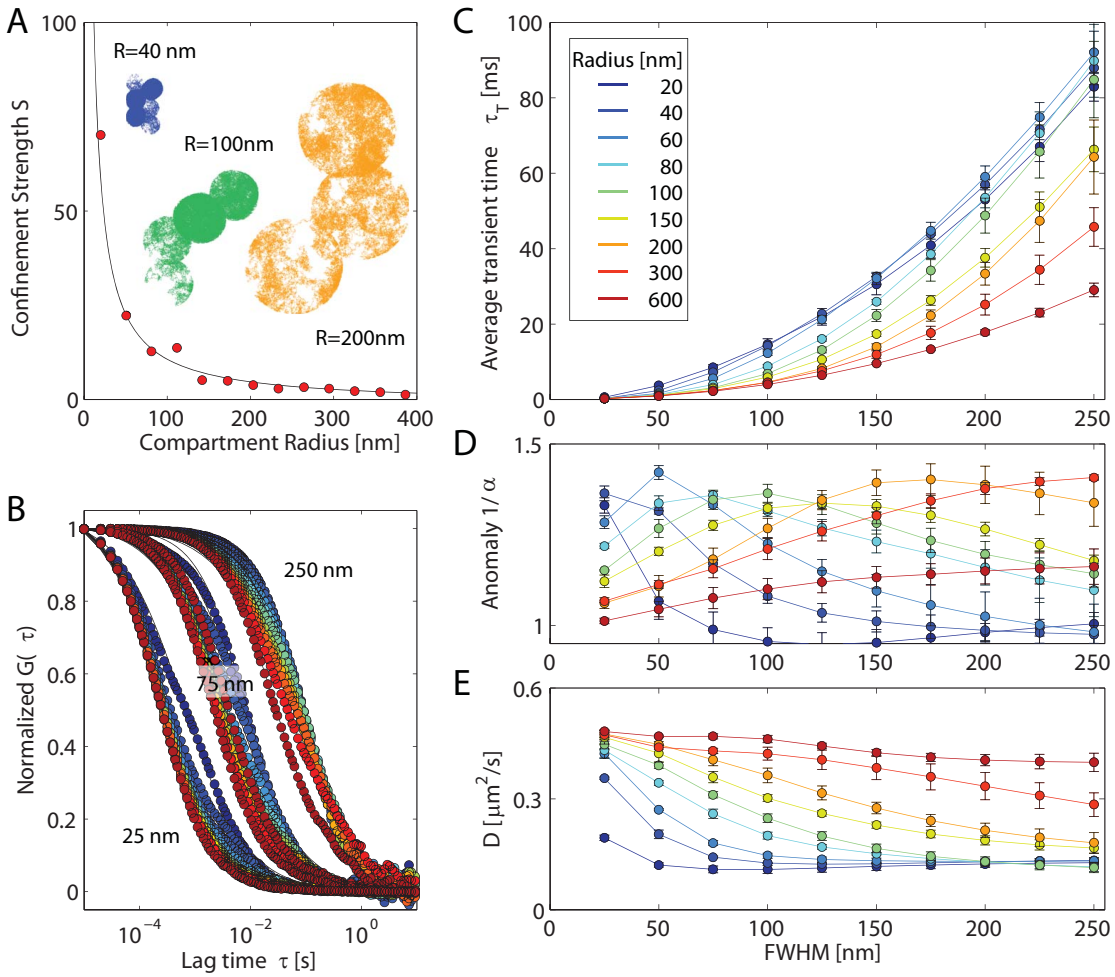

Figure 5.8.: Hop diffusion for varying compartment radii and $P_{\text{hop}} = 0.01$: (A) Confinement strength as a function of the compartment size (red dots) and fit to theoretical model (black solid line). (B) Simulated correlation curves for increasing compartment radii at three different sizes of the observation area (open circle: average of 3 individual simulation runs). The fit of the correlation curves (solid black line) yields the average transient time (C), the anomaly $1/\alpha$ (D) and allows us to calculate the apparent diffusion coefficient D (E). Simulation parameters: $T = 100$s, $N = 100$, $D = 0.7\mu\text{m}^2/\text{s}$, $R_c = 40\mu$m, $R_{\text{sim}} = 2\mu$m.

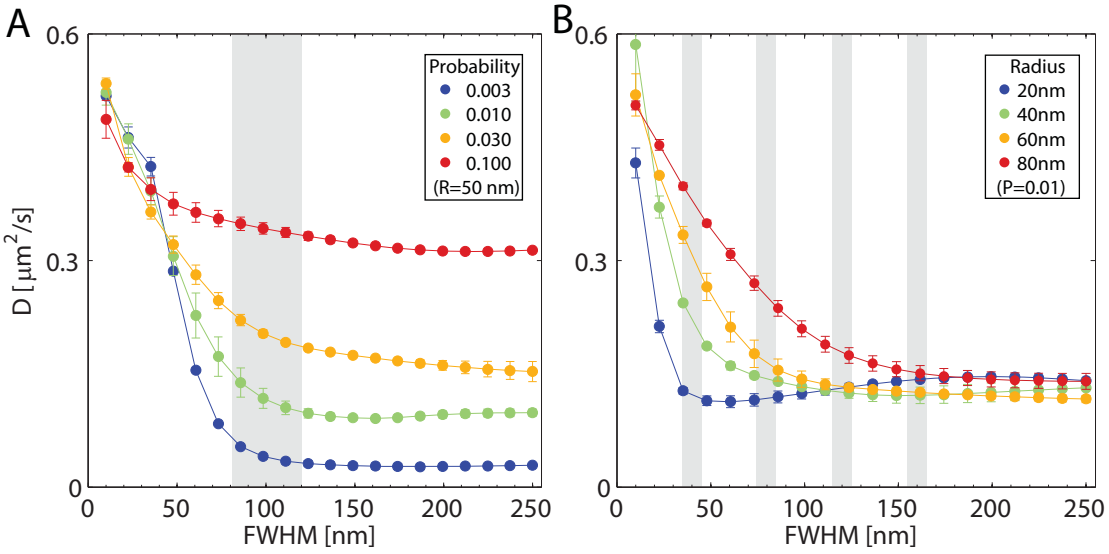

Figure 5.9.: Apparent diffusion coefficient as a function of the observation area for different hop-probabilities (A) and compartment radii (B). Note, that in (B) the confinement strength $S \propto A/R_c + B$ is kept constant for changing compartment radii.

time, anomaly and apparent diffusion coefficient of the diffusion. The introduction of additional constraints in the diffusion process allows us to estimate the effects of either a transient binding or meshwork-based confinement on the diffusion characteristics.

Comparing the simulations to the experimentally obtained results, we note that the case of free diffusion precisely recovers the experimental observations for a freely diffusing lipid. In the case of a trap- or hop-like constrain as experimentally observed for sphingolipids or transmembrane protein, we however note that our present simulation schemes fail to consistently describe the experimental results. In the case of a trap-like confinement, we retrieve the general decrease observed for the apparent diffusion coefficient but the attributed constrains are much stronger than experimentally observed. Accordingly, in the case of a hop-like confinement, the simulations confirm the observed characteristic increase of the apparent diffusion coefficient as well as the final approach towards the free diffusion characteristics as observed for the transferrin receptor. In order to coincide with the experimental results, the underlying dimension of the simulated compartment size are however of the order of more than 250nm and hence significantly larger than the average meshwork size of the cytoskeleton ($\approx$ 60nm).

We therefore conclude that the present simulation scheme provides us a valuable guideline towards a consistent interpretation and understanding of the previous STED-FCS experiments. The observed discrepancy to the experimental results, however, advise

us to improve and adapt our current simulation scheme. A dynamic regulation of the trap parameter and dimensions might for instance allow us to observe a significant molecular confinement for reasonable average trap times and confinement strength. Extending the current simulation algorithm by the implementation of a transient association to distinct membrane domains with reduced diffusion coefficient might further allow us to retrieve the observed diffusion characteristics of head group induced confinement as observed for the GPI-anchored protein. Moreover, the combination of trap- and hop-like diffusion is certainly needed in order to accuratly describe the observed diffusion of raft-associated transmembrane proteins.

6. Conclusion and outlook

STED-FCS has proven to be a sensitive and unique tool to visualize the heterogeneous organization of lipids and proteins within the plasma membrane of the living cell. The observed molecular interactions are shown to occur on a nanoscopic length scale and cannot be resolved with diffraction-limited microscopy [62]. In the past, the observation of membrane dynamics using conventional experimental techniques therefore relied on an extrapolation of diffraction-limited recordings and only provided an estimate of the diffusion characteristics beyond the diffraction barrier [72, 108]. Combining the high spatial resolution of STED nanoscopy with the high temporal resolution of FCS, in contrast, enables us to directly access the diffusion dynamics on the nanoscale.

Tuning the spatial resolution continuously, down to $d = 30$ nm, STED-FCS reveals distinct differences between the diffusion of fluorescent lipid analogs as well as fluorescently-tagged proteins. Following our observations, we identify four types of transient molecular interactions between lipids and proteins. First, a weak interaction on timescales of ≈ 1 ms is observed to characterize the diffusion of phosphoglycerolipids without hydroxyl-containing head groups such as PE and PC. Secondly, the diffusion of lipids and lipid-anchored proteins carrying large hydroxyl-containing head groups is determined by cholesterol- and cytoskeleton-independent interactions due to head group-assisted binding as observed for gangliosides, GalCer, phosphoinositol and the lipid GPI-anchor. The third type of interactions dominates the diffusion of sphingolipids such as SM. These lipids are observed to strongly interact via the formation of hydrogen bonds within their characteristic ceramide structure. The observed transient binding events can be ascribed to the formation of short-lived (≈ 10 ms) lipid complexes with other membrane constituents such as proteins and exhibit a strong cytoskeleton dependence. Finally, the diffusion of transmembrane proteins is confined within the barriers of the cytoskeleton. In contrast to a non-raft marker, the transferrin receptor, the raft associated proteins MAL and LAT experience an additional confinement due to transient molecular interactions. Both interactions are weakened upon cholesterol and cytoskeleton depletion, and further reversed by a genetic mutation of a palmitoylation site within the transmembrane domain, as shown for a palmitoylation deficient genetic mutation of the LAT protein (LAT-C26A). Varying the mutation site, we found that the confined diffusion characteristics of LAT are not

effected by a truncation of the cytosolic protein domain or genetic mutation of the cytosolic palmitoylation site. Even though these observation suggest the meshwork-based confinement to be mediated within the hydrophobic part of the plasma membrane, a consistent interpretation of the results is impeded due to an insufficient fluorescent labeling of the membrane associated proteins.

The implementation of specific Monte Carlo simulations allows us to model the effects of molecular trapping and meshwork-based confinement on the diffusion characteristics observed in a STED-FCS experiment. In comparison to the experimental results, the performed simulations retrieve the general dependences of the observables. We note, however, that the simplified diffusion models only provide an insufficient description of the experimental data. An accurate reflection of the diffusion dynamics within the membrane certainly requires the implementation of more complex simulation algorithms, such as for instance Monte-Carlo simulations based on a two-dimensional random field Ising model [109, 110]. Nevertheless, the present simulation scheme fosters our understanding of the experimental STED-FCS results and guides us in the interpretation of future experiments.

Apart from theoretical simulations, an important key to the fundamental principles of nanoscale dynamics certainly lies in the design and investigation of suitable model systems. In the future, a detailed study of diffusion dynamics in the liquid-ordered and disordered phase of a supported lipid bilayer might advise us how to relate the observed phase partitioning of the model system to the nanoscale interactions within the plasma membrane [56]. Moreover, recently developed extraction protocols allow us to seperate giant plasma membrane vesicles (GPMV's) from the native plasma membrane [111]. Measuring the diffusion dynamics in these vesicles directly allows us to examine nanoscale diffusion within the native membrane composition, but free of additional influences of the underlying cytoskeleton .

While STED-FCS in its present realization allows us to differentiate the complex diffusion behavior of lipids and proteins, it still conceals any insights about the spatial distribution of the underlying confinement or the identification of respective interaction partners. Future advances will therefore focus on the technical improvement of the current experimental concept. The introduction of a second color, for instance, may reveal putative binding partners for lipids and proteins using fluorescence cross correlation spectroscopy [65]. Furthermore, the spatial visualization of diffusion heterogeneities may be addressed by the implementation of a of scanning STED-FCS approach [112]. As discussed in the following part of the thesis, the realization of scanning STED-FCS not only allows us to spatially distinguish distinct regions of diffusion, but may also link the characteristic nanoscale confinement to specific regions within the membrane. Studying the variations of molecular dynamics in different spatial regimes may guide us to elucidate the functionality of nanoscale lipid and protein dynamics in various cellular processes.

Part II.

Scanning STED-FCS explores spatial heterogeneities in diffusion

7. Introduction

As demonstrated in the first part of this thesis, STED-FCS has proven to be a unique tool to directly investigate the diffusion of lipids and proteins within the plasma membrane. Confining the size of the observation area beyond the diffraction barrier enables us to quantitatively distinguish distinct modes of diffusion and allows us to gain valuable insights into the molecular dynamics and interactions of lipids and proteins. In these experiments, we observe that the diffusion for specific lipids and membrane proteins is confined on small length scales and highly dependent on the cholesterol and cytoskeleton contents of the cell.

Since both the cholesterol and cytoskeleton density exhibit a heterogeneous spatial distribution, the diffusion dynamics are expected to follow a similar spatial variations across the membrane [43]. Currently, these dynamic heterogeneities can not be observed with a conventional STED-FCS experiment, which only probes the diffusion within a single point. For the reconstruction of the diffusion characteristics in terms of the FCS diffusion law, the observation area is continuously repositioned after each confocal or STED recording in order to avoid phototoxic or -thermal damage of the plasma membrane. The obtained FCS diffusion laws for varying STED intensities thus only represent an average diffusion characteristic collected at different membrane position, but conceal any information about spatial heterogeneities.

A conventional STED-FCS experiment not only fails to resolve the spatial distribution of diffusion dynamics, but also requires a careful consideration of the experimental situation before and during the experiment. First, STED-FCS relies on an accurate calibration of the observation area in order to translate the relative diffusion times into an absolute value of the apparent diffusion coefficient. Although we have developed reliable calibration routines to ensure an accurate calibration of nanoscale observation area (see section 2.1), these routines are not only time consuming, but are also repeated throughout the experiment in order to account for possible variations in the resolution due to for instance mechanical drift of the setup alignment.

Secondly, we note that the execution and analysis of a STED FCS experiment is prone to a variety of artifacts. During the experiment, the membrane, for instance, needs to be accurately positioned within the observation area. Especially for unsupported model membranes or slowly diffusing particles with acquisition times of several hundreds seconds, the precise and stable positioning of the nanoscale observation area is

essential for an accurate determination of the correlation curves and has proven to be experimentally challenging in the past. Furthermore, we note that slowly diffusing particles are prone to experience photobleaching on their slow passage through the excitation spot. Although these bleaching artifacts may be reduced by decreasing the excitation power, low excitation powers impair the brightness of the fluorescent molecules and thus significantly reduce the signal-to-noise ratio of the experiment. Considering that in a nanoscale observation areas, the fluorescence is only recorded from a few particles at a time, the quality of the experiment heavily relies on a sufficient signal-to-noise ratio in order to ensure the sensitive detection of rarely occurring transients. A conventional STED-FCS experiment thus not only suffers a lack of additional spatial information but also fails to record the diffusion dynamics of slowly diffusion particles or mobile model membranes.

In the following part of the thesis, we therefore extend our conventional STED-FCS setup in order to address these experimental issues. Especially for slowly diffusing membrane constituents, we can employ the comparably long transient times to rapidly scan the observation area across the membrane during the measurement. Every time the observation area returns to its initial position, it then records the diffusion of each particle within the focal spot. As soon as the scan frequency is sufficiently high to observe each particle multiple times in subsequent scans, the obtained fluorescence intensity trace can be used to reconstruct the correlation functions at each position of the scan trajectory. While the scan trajectory may follow any arbitrary path, first implementations of this scanning FCS approach were performed using a circular scan movement [113, 114, 112]. In contrast to the later introduced linear line scans [115, 116], the circular movement not only allows to most rapidly drive a two-dimensional scanning unit, but also performs a continuous scan movement without a disruptive de- and acceleration at the reversal points.

While scanning FCS allows to directly visualizes the spatial distribution of diffusion dynamics along the scan trajectory, the simultaneous recording of multiple correlation curves is also advantageous for the observation of homogeneous samples. Averaging the recorded correlation curves, for instance, significantly improves the statistical accuracy of the measurement and thereby is reported to reduce the required acquisition times of the experiment [117, 68, 118]. Moreover, the introduction of an additional spatial correlation along the scan trajectory, enables us to infer the spatial extend of the observation area and render a calibration-free FCS measurement possible [115]. Especially for STED-FCS, such a calibration-free determination of the diffusion characteristics would essentially facilitate the alignment and calibration procedures previous and during the experiment.

In the past, scanning FCS has been successfully applied to a variety of biological systems [119, 120, 90, 67]. In these experiments, the short dwell times within the experiment have proven to efficiently prevent photothermal and toxic damage during

the observation of slowly diffusing particles [116, 121]. Furthermore, scanning FCS techniques were reported to enable the observation of diffusion in unsupported membrane system [69, 112, 116]. Scanning the observation area perpendicular across the membrane not only reduced the observed motion due to thermally induced drift but also allowed to account for any lateral movement using a drift correction for each line scan [122].

Altogether the implementation of a scanning STED-FCS experiment not only provides us with valuable spatial information of nanoscale interactions along the scan trajectory, but also improves the accuracy and calibration of a conventional STED-FCS experiment and offers a broad scope of novel biological applications.

8. Experimental materials and methods

In this section, we introduce the experimental setup used throughout the scanning STED-FCS experiments and discuss the essential steps of the data acquisition and processing. We further discuss various approaches of the theoretical data analysis as it is performed in the following experiments.

8.1. Experimental setup

The experimental setup discussed in section 2.2 is extended by the integration of a fast scanning unit which enables us to scan the excitation and STED beam rapidly across the sample plane.

In a series of preliminary experiments, a compact mirror tilting piezo was used to perform a one-dimensional line scan with a total scan angle of 35 mrad and maximal scan frequencies of up to 2.5 kHz (PSH-4/1, piezosystemjena, Jena, Germany). The scanning range was extended to two dimensions by replacing the mirror tilting system with a digital scanning unit (Yanus digital scan head, TILL Photonics, Gräfelfing, Germany). In this unit the beam is scanned by two galvanometric scanning mirrors with a total area of 5 mm x 6 mm, each. A spherical mirror within the scan cavity images the first scanning mirror precisely onto the second mirror and therefore prevents the peripheral clipping of the beam for large scan angles. In combination with achromatic scan and tube lenses in a 4f-configuration (f= 50mm and f=240 mm, Leica, Wetzlar, Germany), a stationary beam position in the back aperture of the objective is achieved preventing peripherical darkening within the focal plane at large scan ranges (e.g. vignetting). The maximal frequency of the Yanus scanner depends on the scan amplitude and varies between $2 - 6$ kHz for scan amplitudes between $150 - 4\mu m$, respectively.

Next to the integration of the fast scanning unit, the addition of a second blue excitation beam with a wavelength of $\lambda = 488nm$ complements the red excitation at

$\lambda = 635$nm. A confocal detection unit with a detection window around 535 ± 20nm allows the diffraction limited observation of green fluorescence emitted by for instance organic dyes such as Alexa-488 and Bodipy-FL or the green fluorescent protein (GFP).

8.2. Data acquisition and analysis

In a scanning STED-FCS experiment, the observation area is continuously scanned across the focal plane. In order to correlate the detected fluorescence at each position, it is thus crucial to accurately determine the spatial origin of each detected photon.

In the above described experimental setup, the precise synchronization of the scanning position and data acquisition is either achieved externally using a hardware controller which drives the scanning mirrors and simultaneously provides a trigger signal to the independent data acquisition. Alternatively, the data acquisition is controlled internally by the image acquisition software ImSpector which initializes and generates the voltage waveforms for the scan movement and synchronizes the data acquisition. While the ImSpector software directly adjusts the acquisition range of the scan movement to the linear range of the driving waveform, the external hardware control requires an accurate calibration of the scan range and velocity in relation to the generated waveform and trigger signal. This calibration then allows to deduce the linear scan range within each line scan. Assuming the scan velocity v to be constant the resulting line scans are subsequently binned into pixels of variable pixel size $\Delta s = v * \Delta t$, where Δt denotes the time window used to bin the detected photons.

Figure 8.1 depicts a typical photon trace recorded in a scanning FCS experiment. Here, the observation area was continuously scanned along a circular scan trajectory of radius $R = 1\mu$m and scan frequency $f = 4$ kHz. Plotting each circular scan into a two-dimensional array, we obtain a pseudo-image $F(x, t_i)$ as proposed in [123]. In this presentation, the horizontal axis represents the spatial scan position x while the vertical axis displays the temporal evolution of the photon signal at each scan position. For a given scan period $T = 1/f$, the time at the beginning of the ith line is therefore given as $t_i = iT$ and the time at the nth pixel of the scan correspondence to $t_i n = t_i + n\Delta s$.

8.2.1. Temporal correlation

Assuming that the diffusion of the particles is independent of the incident laser light, we first evaluate the temporal fluctuations for each column of the pseudo-image. Using a multiple τ- algorithm [124], we correlate each column of the recorded pseudo-image yielding a temporal correlation curve $G(\tau_i)$ for each pixel as shown in figure 8.1.

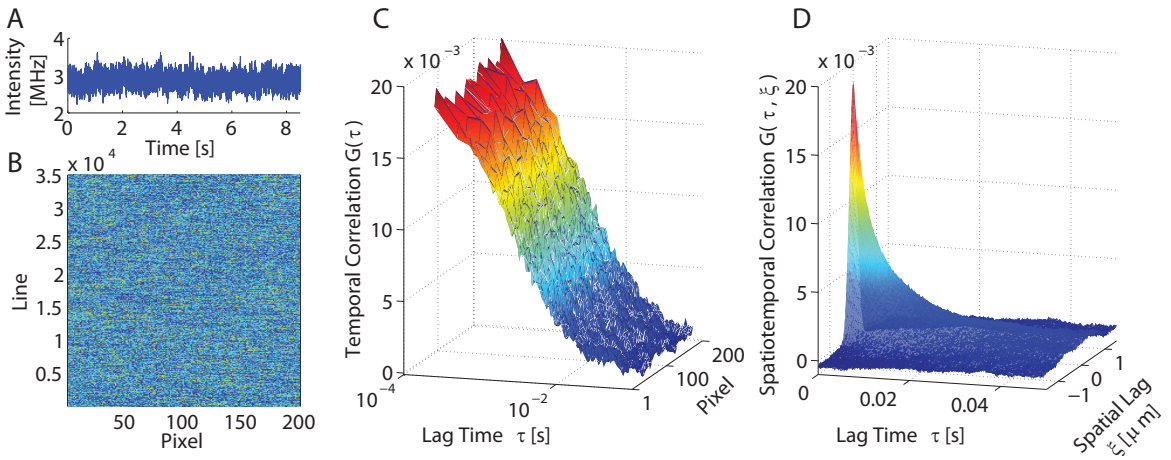

Figure 8.1.: Scanning STED-FCS data analysis: (A) A typical fluorescence intensity trace is recorded over time and plotted as pseudo-image in (B). In this representation the ith row depicts the ith scan, while each column describes the temporal evolution of the fluorescence intensity at each pixel. (C) Correlating each row of the pseudo-image, we obtain the temporal correlation $G(\tau)$ at each pixel. (D) A two-dimensional correlation of the pseudo-image yields the spatiotemporal correlation $G(\tau, \xi)$. (Sample: SLB (DOPC:PE-KK114 (1:0.01)))

If the observation area is moved gradually from pixel to pixel during the scan, the obtained correlation curves are accurately described using the theoretical model for two dimensional diffusion of a single-spot FCS measurement. If the focus area is however scanned continuously along the scan trajectory, we have to carefully consider the shape of the observation area in order to chose the appropriate theoretical description of the temporal correlation curves. For pixel sizes Δs much smaller than the waist of the observation area w_0, the observation area is still sufficiently approximated by a Gaussian illumination profile and the theoretical model of a single-spot FCS measurement may be applied. For $\Delta s >> \omega_0$, in contrast, the shape of the observation volume resembles an elongated tube along the scan trajectory and the exact illumination profile is given by a convolution of the Gaussian illumination profile with a step function of length Δs.

$$I = I_0 \int_0^{\Delta s} dx' \exp \frac{(x - x')^2 + y^2}{\omega_0^2} \tag{8.1}$$

Using the definition of the Gauss error function $\mathrm{erf(x)} = 2/\pi \int_0^{\mathrm{x}} \mathrm{dt}\, \exp(-\mathrm{t}^2)$, the theoretical model describing the two dimensional diffusion of a particle within a finite

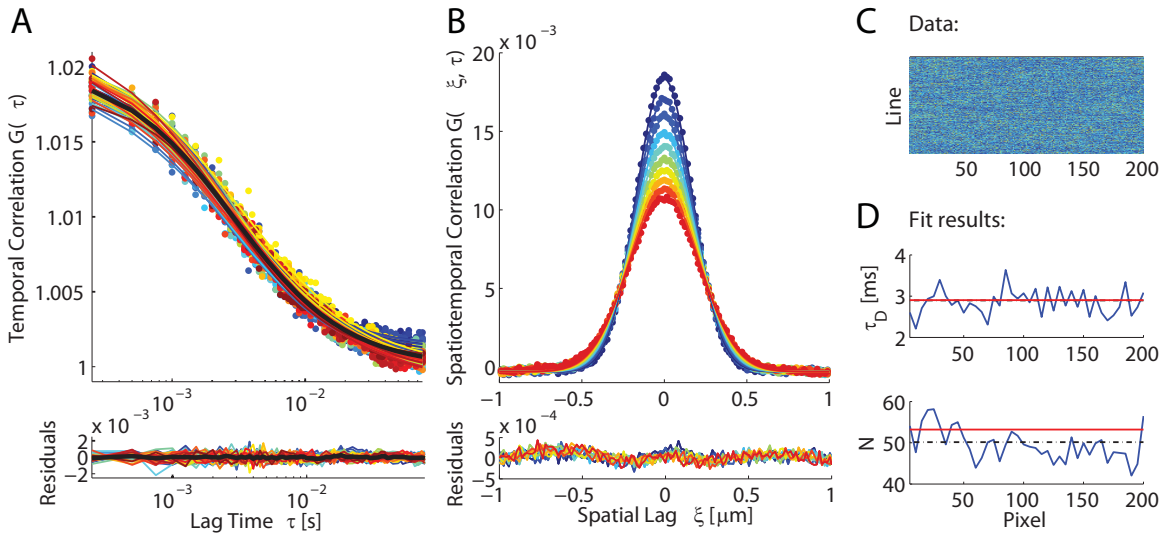

Figure 8.2.: Scanning STED-FCS fit results: (A) The temporal correlation for each pixel (dots) are fit for each pixel independently (solid line) or simultaneously in a global fit (black solid line). (B) The spatiotemporal correlation (dots) and the corresponding fit (solid line) is shown for the first temporal lag times t_i (from blue for $i = 1$ to red for $i = 10$). (D) The fit results of the spatiotemporal correlation (red line) coincides with the fit results obtained for the pixel wise and global temporal correlation (blue and black line). (Sample: SLB (DOPC:PE-KK114 (1:0.01)))

pixel size Δs is given by [68]

$$G(\tau_i) = \frac{\omega_0^2}{\Delta s^2 N}\left(\sqrt{\pi}\mu_i \mathrm{erf}\left(\mu_\mathrm{i}\right) + \exp(-\mu_\mathrm{i}^2) - 1\right) \tag{8.2}$$

$$\text{with} \quad \mu_\mathrm{i} = \frac{\Delta \mathrm{s}}{\sqrt{\omega_0 + 4\mathrm{D}\tau_\mathrm{i}}}. \tag{8.3}$$

Applying this theoretical model to the experimental data recorded for a SLB (DOPC: PE-KK114 (1:0.01)), we retrieve the average number of N particles within the observation area as well as their diffusion coefficient $D = \omega_0^2/4\tau_D$ as shown in figure 8.2. Here, the temporal correlation is fitted either for each pixel independently or globally by fitting all correlation functions in a single fit. Comparing the obtained fit results, we observe that the fit results for each pixel oscillate around the fit result of the global fit ($\tau_D(\text{median}) = 2.9$ ms, $\tau_D(\text{global}) = 2.8$ ms and $\alpha = 1.06 - 0.98$). Both fit results also coincide with the fit results obtained for a single spot measurement ($\tau_D = 2.85$ ms with $\alpha = 0.97$). We note that for small dwell times the quality of the fit can be further improved by averaging the obtained correlation functions of adjacent pixels.

8.2.2. Spatiotemporal correlation

Next, we include the spatial correlation in our data analysis by calculating the two-dimensional spatiotemporal correlation function of the pseudo image $F(x, t_i)$ according to

$$G(\xi, \tau_i) = \frac{\langle \delta F(x, t_i) \times \delta F(x + \xi, t_i + \tau_i) \rangle}{\langle F(x, t_i) \rangle^2}. \tag{8.4}$$

Here ξ and τ_i denote the spatial and temporal lag time, respectively and $\langle\rangle$ indicates the average over all spatial and temporal recordings. A typical spatiotemporal correlation function for a circular scan is shown in figure 8.1. We note, that the spatiotemporal correlation can be calculated independent from the scan modalities as long as the spatial and temporal separation between adjacent pixels and subsequent scans are constant within the pseudo image.

For pixel sizes Δs much smaller than the waist of the observation area ω_0 of the Gaussian illumination profile, the theoretical model of the spatiotemporal correlation function can be calculated according to [115]

$$G(\xi, \tau_i) = \frac{1}{N} \left(1 + \frac{4D}{\omega_0^2} \left(\tau_i + \frac{\xi}{v} \right) \right)^{-1} \times \exp \left(- \frac{2\xi^2}{\omega_0^2 + 4D(\tau_i + \xi/v)} \right). \tag{8.5}$$

In this equation the correlation curve is effectively split into two terms. The first term expresses the correlation due to the diffusional movement of the particles as it is known from a single spot FCS measurement. We note that the diffusion coefficient is coupled to the waist of the observation area ω_0^2 via the diffusion time $\tau_D = \omega_0^2/4D$ rendering an independent determination of both parameter infeasible. The second exponential term in contrast reflects the correlation due to the scanning movement of the observation area. For a known constant scan velocity v, this expression decouples D from ω_0 and thus allows to simultaneously fit both quantities in a single measurement which does not require a previous characterization of the observation area.

In figure 8.2, we present the obtained fit and residuals of a spatiotemporal correlation curve. Since the observed diffusion in this sample is fast compared to the period of the circular scan ($\tau_D \approx 2.8$ ms and $T_{\text{scan}} = 0.25ms$), the spatiotemporal correlation drops rapidly. We therefore restrict the range of the spatiotemporal correlation curve considered in the fit analysis to spatial lags between $\xi = \pm 1\mu$m and small lag times $t_{i=1-10}$. The obtained fit results for the diffusion time $\tau_D = 2.9$ ms and the average number of particles within the observation volume $N = 53$ coincides well with the values obtained for the temporal correlation and the single-spot FCS experiment. Furthermore a fit of the spatiotemporal correlation provides us with the size of the observation area $\omega_0 = 240$ nm which corresponds well to the expected size of the diffraction limited focus spot for the excitation beam with a wavelength of $\lambda = 640$nm.

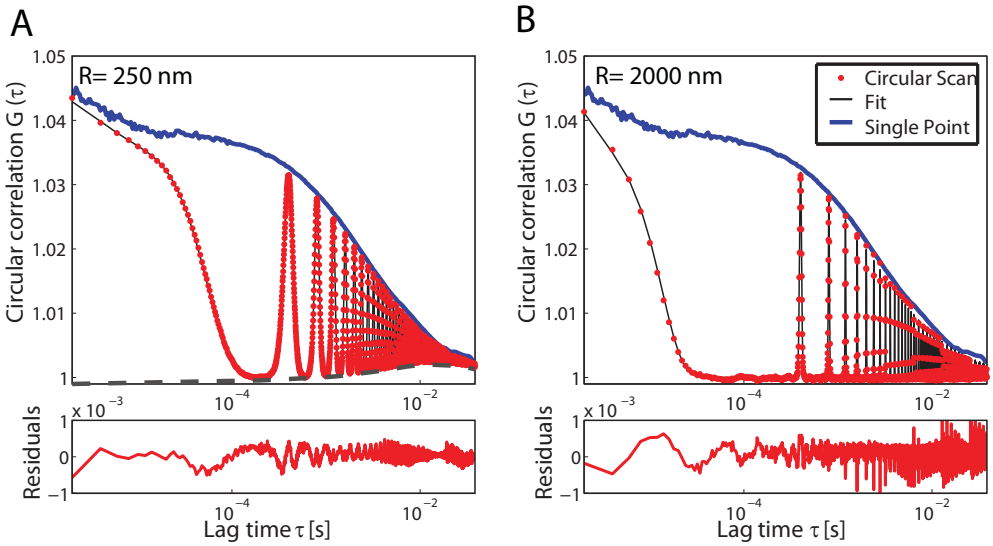

Figure 8.3.: Circular correlation: The temporal correlation of the intensity trace along a circular scan features a characteristic oscillation whose frequency corresponds to the scan frequency ($f = 4$ kHz). The amplitude is modulated by the correlation of a single spot experiment (blue line) and the expected cross-correlation between two opposite positions on the scan radius (grey line). Note the decrease in cross correlation for a increased scan radius (R=250 nm in (A) and R=2000nm in (B)).

8.2.3. Circular correlation

In our data analysis, we can further exploit the fact that for a periodic circular scan the observation volume is moved continuously across the sample plane. Assuming the scan velocity to be constant on the circular orbit, the collected photons can be correlated directly over time from the continuously recorded signal.

The obtained so-called circular correlation as shown in figure 8.3 (red dots) exhibits a characteristic oscillatory modulation of the correlation curve. The frequency of the oscillation corresponds to the scan frequency of the periodic scan movement while the amplitude is modulated by an upper and lower envelope. The upper envelope follows the correlation expected for a single spot FCS measurement (blue line) and is thus determined by the diffusional properties of the molecules. The lower envelope in contrast reflects the cross correlation of the signal collected at two opposite points on the circular scan (gray dotted line) and therefore directly depends on the scan radius and the size of the observation area. Increasing the size of the scan radius, for instance, decreases the contribution of the cross-correlation and for radii much larger than the observation area no cross-correlation is observed (see figure 8.3).

Similarly to the spatiotemporal correlation, the circular correlation can exploit the

spatial information of the known scan trajectory in order to extract both the diffusion coefficient D and the beam diameter ω_0 from the fit to the experimental data. For a circular movement of frequency f and radius R the theoretical correlation function is given by [117]

$$G(\tau) = \frac{1}{N}\left(1 + \frac{4D}{\omega_0^2}\tau\right)^{-1} \times \exp\left(-\frac{4R^2 \sin^2(\pi f \tau)}{\omega_0^2 + 4D\tau}\right). \tag{8.6}$$

Fitting the data in figure 8.3 (A) to the theoretical model, we retrieve the diffusion time $\tau_D = 2.5$ ms and $\omega_0 = 240$ nm. All results are in well agreement to the fit results of the previously discussed correlations and the single spot experiment. In contrast to the pixel based correlation analysis whose time resolution is limited by the scanning frequency, the circular correlation correlates the complete intensity trace. The beginning of the correlation thus allows us to assess processes whose kinetics are of the order of a few μs such as triplet state formation. In our example, we find the triplet fraction $A = 0.22$ and the triplet time $\tau_T = 3.4\mu$s to coincide with the triplet kinetics observed in the corresponding single spot measurement ($A = 0.20$, $\tau_T = 4.7\mu$s).

8.2.4. Bleaching correction

During a scanning STED-FCS experiment the beam is repetitively scanned along the same trajectory. Due to the high scan frequency of the order of 5kHz, more than 10^4 scans are typically acquired during a single experiments of only a few seconds. It is therefore not surprising, that the average number of particles in the observation volume slowly decreased because of photo-bleaching. Especially in a two dimensional system of slowly diffusing particles, the bleached fraction is insufficiently recovered causing an overall decrease of the recorded intensity trace. As shown in figure 8.4 a strict application of the temporal correlation to such an intensity trace leads to a strongly distortion of the correlation curve.

We therefore account for the observed photobleaching by correcting the recorded intensity traces. As proposed by Ries at al., the decay of the intensity trace is described by an analytic function, which is in dependence of the replenishment rate approximated by a mono- or multi-exponential function of the form $f(t) = f_0 \exp(-t/t_b)$ [68]. Here t_b denotes the average bleaching time for which the initial observed fluorescence intensity has dropped by a factor of $1/e$ and is retrieved directly from the experimental trace. Upon determination of $f(t)$ the intensity trace is corrected according to

$$F^c(t) = \frac{F(t)}{\sqrt{f(t)/f(0)}} + f(0)\left(1 - \sqrt{f(t)/f(0)}\right). \tag{8.7}$$

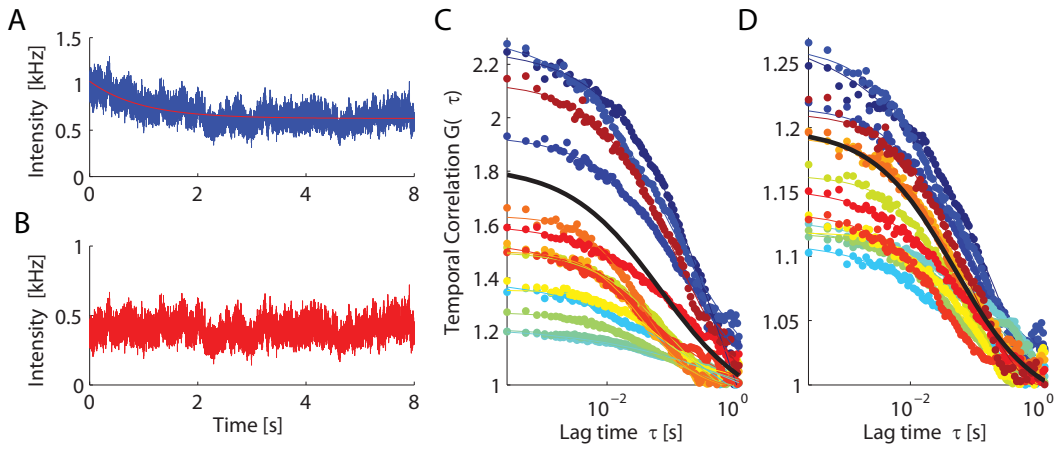

Figure 8.4.: Bleaching correction: (A) The intensity trace (blue) is fit to determine the bleaching kinetics and corrected according to the theoretical model (B). (C+D) Correlation curves for the uncorrected (left) and corrected intensity trace (right). Note, that the correction shift of the correlation curves to smaller lag times.

Although this correction allows to reconcile the correlation curves in the presence of photobleaching, we note that strong photobleaching inevitably also leads to an overall reduction in the observed transient times, which can not be corrected for by any correction scheme.

8.3. Computational realisation

All data analysis procedures are implemented in Matlab. A graphical interface allows the user to read the recoded data either directly from the file formate of the data acquisition software ImSpector or as a raw data file of a FIFO trace. In the latter case the trigger of the scan line needs to be provided in an additional data channel and is used to cut the recorded data at the beginning of consecutive scans.

The reconstructed pseudo-images of the intensity trace can be optionally corrected for photobleaching, before the temporal and spatiotemporal or circular correlations are calculated. The obtained correlation are fit to the theoretical models using non-linear least squares fit routines. The retrieved fit results are directly plotted and can be saved or exported to an Excel spreadsheet.

9. Experimental results

In this section, we explore the potential of scanning STED-FCS to extend the conventional single spot STED-FCS experiments towards a calibration free mapping of spatially inhomogeneous nanoscale dynamics.

9.1. Characterization of the experimental setup

In order to characterize the diffusion of a particle in a scanning STED-FCS experiment, an accurate calibration of the scan trajectory is inevitable. Furthermore, we carefully evaluate the optimal range of the applied scan parameters to avoid artifacts in the determination of the diffusion times due to for instance an insufficient time resolution of the experiment.

9.1.1. Calibration of the effective scan trajectory

First, we calibrate the scan amplitude using a test sample which features a regular array of points. The well defined distance between adjacent points of 2μm allows us to determine the scan amplitude in correspondence to the applied voltage. This provides us with an adequate calibration of the scan movement for moderate scan velocities and amplitudes. At high scan velocity however, the galvanometric scan mirrors are unable to follow the applied driving voltage rendering the effective scan trajectory highly dependent on the scan parameters. We therefore need to carefully derive the effective scan trajectory in dependence of the applied scan parameters.

In order to measure the effective scan trajectory, we use an external scanning stage to move a sample of immobilized gold beads across the sample plane. As shown in figure 9.1, the resulting image of a single gold bead allows us to directly visualize the circular scan trajectory. A line profile across the largest diameter of the circular orbit is used to derive the effective scan radius R_{eff}. Plotting the effective scan radius as a function of the scan frequency or scan velocity for various applied driving radii, we observe a significant dependence on both the scan frequency as well as applied driving radius (i.e scan amplitudes). For small frequencies, the effective scan radius is independent

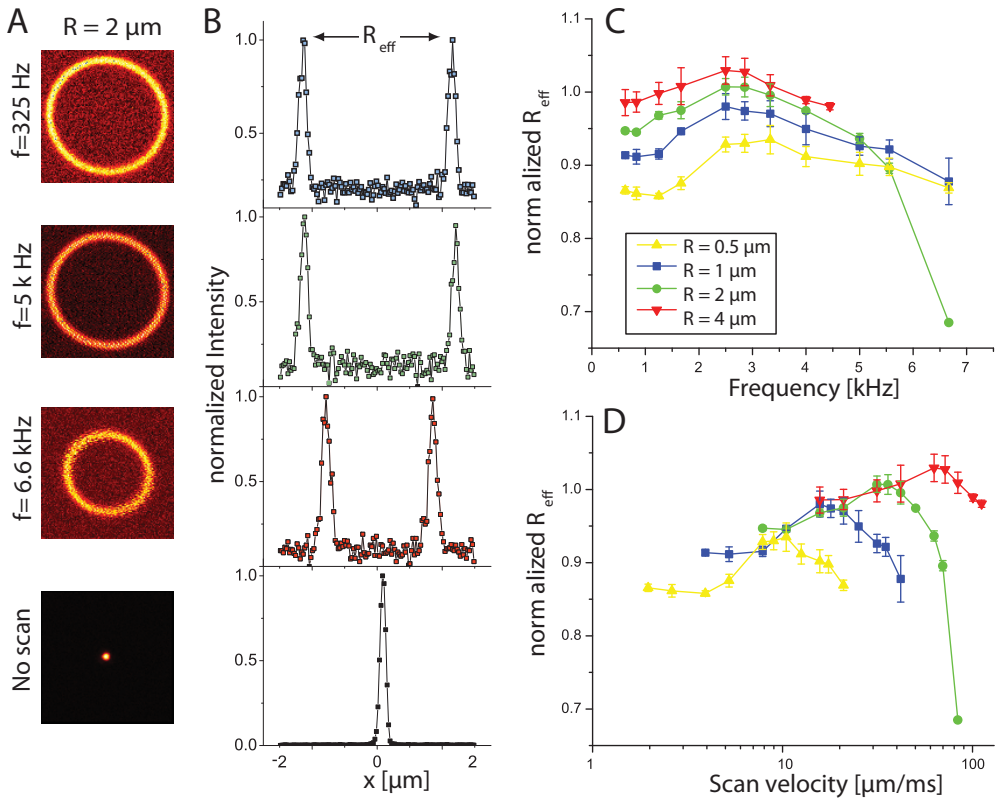

Figure 9.1.: Calibration of the effective scan trajectory: (A) Image of individual immobilized gold beads scanned across the excitation laser scanned along an circular orbit for different scan frequencies (Image: 2x2μm). (B) Measuring the line profiles across the radius of the circular trajectory allows us to determine the effective scan radius R_{eff}. (C+D) The effective radius is normalized to the applied scan radius R and plotted for different scan radii R as a function of the scan frequency and velocity.

from the applied scan frequency but does increase for increasing driving radii. At intermediate scan frequencies between 2 and 3 kHz, the effective scan radius increases with increasing scan frequency due to an intrinsic resonance of the galvanometric scan mirrors. This effect is reversed for high scan frequencies above 3kHz, at which the scan mirrors fail to follow the applied scan frequency and the effective scan radius rapidly decreases.

Apart from the spatial calibration of the scan trajectory, a scanning STED-FCS experiment requires the excitation laser to reproducibly return to its initial position along the circular trajectory. In order to quantitatively characterize the accuracy and stability of the scan movement, we repetitively scan an individual gold bead along a line perpendicular to the circular trajectory of the scanned excitation beam. Since

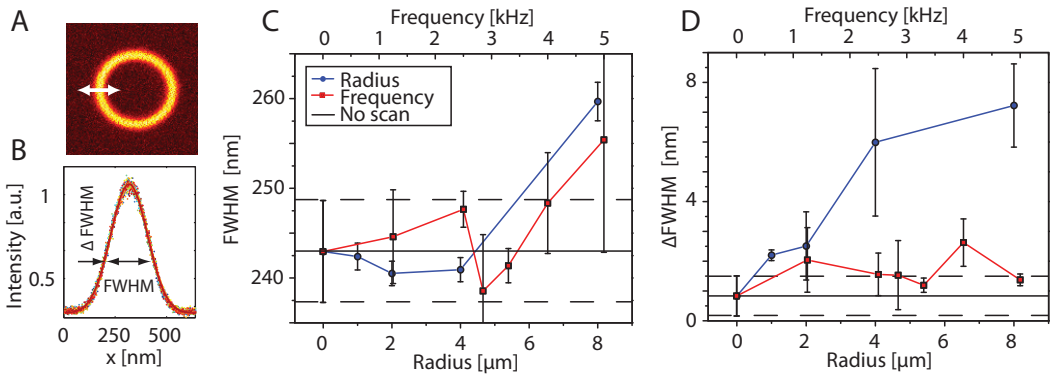

Figure 9.2.: Scan Accuracy: (A) An individual immobilized gold bead is scanned repeatedly perpendicular across the circular scan orbit. (B) The obtained line profiles are fitted to retrieve the FWHM as well as the variation $\Delta FWHM$ across 16 subsequent bead scans. (C+D) Both are plotted as a function of the applied scan radius and frequency and compared to the results for a stationary beam (mean: solid lines, $\pm$ stdev: dashed line).

the gold bead is moved slowly with dwell times which are at least four times larger than the scan period the obtained line profiles depict an average of the scan positions for multiple subsequent scans. Fitting the obtained line profiles to a Gaussian, allows us to extract the full width at half maximum (FWHM). If the beam position jitters between subsequent circular scans within a single line scan, the FWHM increases in comparison to the FWHM measured for a stationary bead. A jitter on larger time scales is detected as an increased variation of the FWHM across different line scans. As shown in figure 9.2, no significant spatial jitter is observed for frequencies below 4 kHz recorded at a scan radius of 1 μm (red line). Increasing the scan radius for a scan frequency of 3.3 kHz, the spatial accuracy however decreases at scan radii above 2 μm (blue line) with a maximal spatial jitter of the order of 5 nm.

As a result of this calibration and characterization of the experimental setup, we restrict our scan parameters to frequencies well below 5 kHz and scan amplitudes up to 2μm. We further use the calibration of the normalized effective radii determined in figure 9.1 as a correction factor for a set of given scan parameters throughout following scanning STED FCS experiments.

9.1.2. Evaluation of optimal scan parameters

In a scanning FCS experiment, the accessible temporal resolution is limited by the scan frequency and typically found to be in the range of $\Delta\tau = 1/f = [0.2 - 1ms]$. Since the diffusion times of a freely diffusing lipid through an observation area of 50

nm are expected to be of the same order, we need to carefully evaluate the minimal requirements for the range of scan parameters which still provide us with a sufficient temporal resolution.

To model the expected transient times in a STED-FCS experiment, we measure the diffusion of a supported lipid bilayer (SLB, DOPC/ PE-KK114, 1:0.01) with a confocal diffusion time of τ_D(Confocal) $\approx$ 2.8ms. Fitting the obtained temporal and spatiotemporal correlations, we determine the diffusion time τ_D, the average number of particles within the focal area N as well as the focal size $w0$ as a function of the scan frequency (see figure 9.3). Comparing the fit results to the results of a single-spot FCS experiment (dashed lines), we observe that an insufficient temporal resolution at low scan frequencies results in an apparent increase of all fit variables. Thus we need to apply scan frequencies which are at least five times higher than the respective transient rate $f > 5/\tau_D$, in order to ensure an accurate determination of the fit parameters,.

Next to a sufficient temporal resolution, the spatiotemporal correlation further requires an adequate spatial sampling frequency of the circular scan movement (i.e. pixel size). As shown in figure 9.3, we observe an artificial increase of the fit results for larger pixel sizes than the FWHM of the observation area. This effect is especially pronounced for the spatiotemporal correlation for which the optimal pixel size is required to be at least three times smaller than the FWHM.

The following scanning STED-FCS experiments were therefore performed with scan frequencies $f > 5/\tau_D$ and pixel sizes $\Delta s < 3\omega_0$ in order to ensure a sufficiently high temporal as well as spatial resolution.

9.2. Calibration-free determination of diffusion

In a conventional single spot STED-FCS experiment, it is crucial to accurately determine the size of the observation volume in order to express the measured transient times in terms of absolute diffusion coefficients. As discussed in section 7, the additional spatial dimension introduced by the scan movement of the excitation beam allows us to directly determine both the diffusion characteristics as well as the diameter of the observation area.

Labeling a GM1 containing SLB with the B subunit of cholera toxin (SLB: DOPC/ GM1, 1:0.01-0.1 + CTxB-KK114, 2mg/ml for 10 min at 37°C), we observe the diffusion of the bound CTxB. Since CtxB binds upto five GM1 molecules, its diffusion is significantly reduced compared to the lipid diffusion within an SLB. Depending on the GM1 concentration, we record confocal diffusion times in the range of $50 - 100ms$. Scanning the sample with a radius of $R = 1\mu$m and a scan frequency of $f = 4$kHz, we determine the temporal and spatiotemporal correlation as shown in figure 9.4

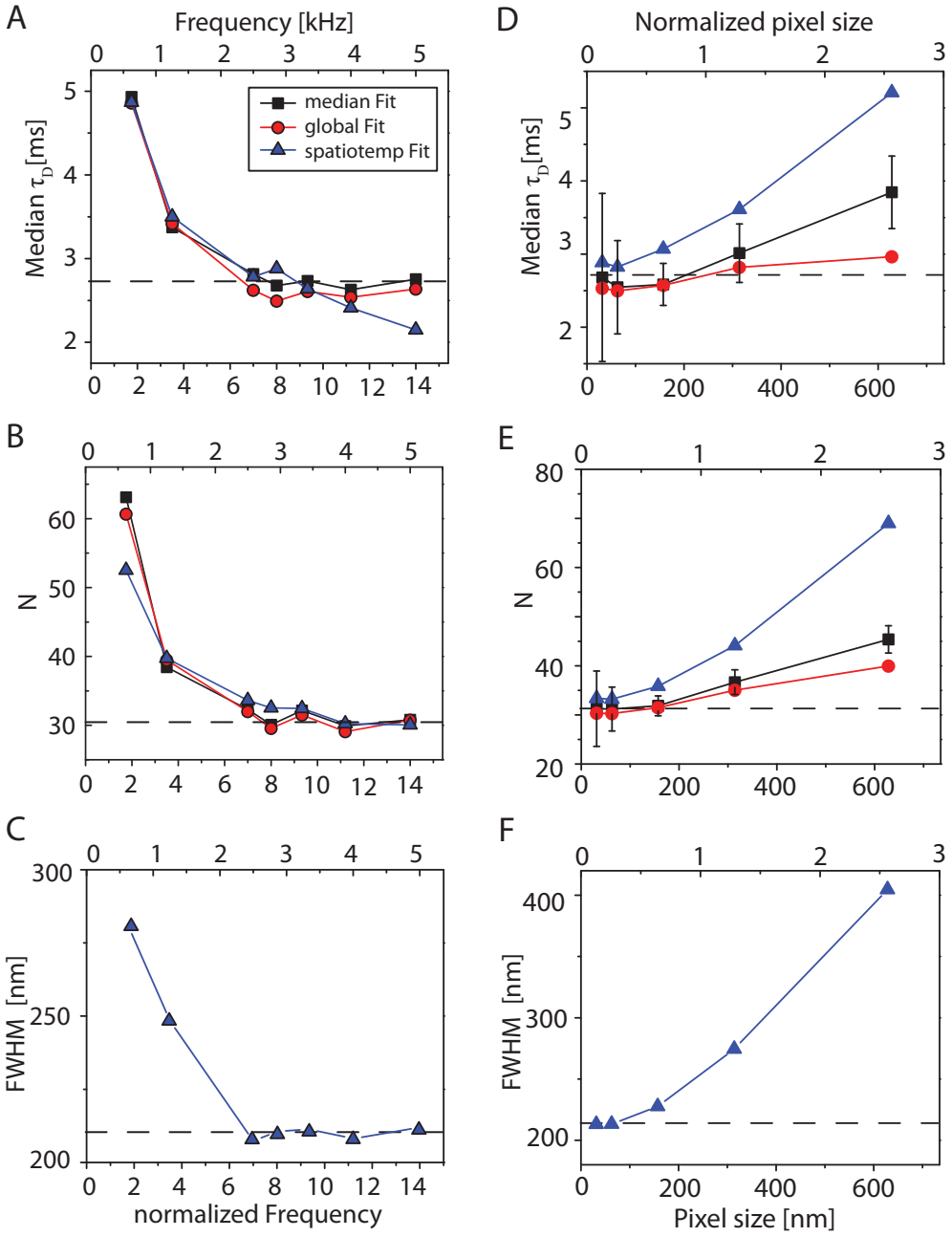

Figure 9.3.: Evaluation of optimal scan parameters: Dependence of diffusion time (A+D), average number of particles (B+E) and FWHM (C+F) as a function of the applied scan frequency (A-C) and pixel size (D-F) in comparison to the fit results obtained for a single point FCS measurement (dashed line). (Sample: SLB, DOPC/PE-KK114, 1:0.01; Scan parameter: $R = 2\mu$m, $\Delta s = 50$nm (A-C), $f = 3.3$kHz (D-F)).

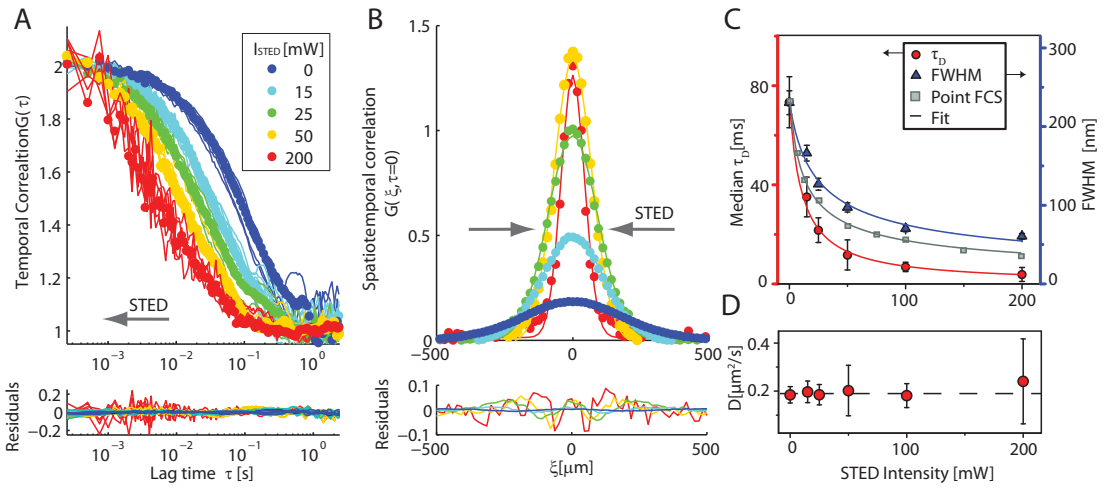

Figure 9.4.: Calibration-free STED-FCS measuremenr: (A) Increasing the STED intensity, the normalized temporal correlation is shifted to shorter diffusion times (circles: average correlation of all pixel, solid lines: correlation for individual pixel $\Delta s = 20$nm). (B) At the same time, the width of the spatiotemporal correlation for $\tau = 0$ is decreased. (C) The retrieved diffusion times (red dots) and FWHM (blue triangle) scale with the theoretical resolution for STED (Fit: solid line). The results are compared to a point STED-FCS experiment (grey squares) representing the expected resolution derived from relative decrease of τ_D.(D) The apparent diffusion coefficient is constant for STED intensities $I_{\mathrm{STED}} < 100mW$.

(blue lines). Increasing the STED intensity, we observe that the temporal correlation is shifted towards smaller diffusion times. At the same time, the amplitude of the spatiotemporal correlation rises while its width is decreased. Plotting the obtained diffusion time τ_D and the FWHM of the observation area as a function of the applied STED intensity, we find that both scale according to the theoretically expected resolution at the corresponding STED intensities I_{STED} given by

$$d(I_{\mathrm{STED}}) = \frac{d(\mathrm{Conf})}{\sqrt{(1 + I_{\mathrm{STED}}/I_s)}} \propto FWHM(I_{\mathrm{STED}}) \propto \sqrt{\tau_D(I_{\mathrm{STED}})} \tag{9.1}$$

where I_s denotes the effective saturation intensity previously introduced in section 1. Fitting I_s to the experimental data ($I_{\mathrm{STED}} = 200$mW excluded from fit), we obtain $I_s = 10.4$ and $I_s = 10.7$ for τ_D and FWHM, respectively. In comparison to a point STED-FCS measurement (gray squares), the achieved resolution is slightly decreased as reflected in a decreased $I_s = 6.0$ for the point measurement. We note however, that the point measurement was performed imaging a fast diffusing lipid in a standard SLB, because the CtxB subunit diffuses to slow to be recorded in a point measurement. The differences in the observed resolution thus might be explained by different STED efficiencies of the fluorescent dye upon coupling to the CtxB subunit due to for instance

fluorescence quenching.

Calculating the apparent diffusion coefficient D, we observe that D is constant for $I_{\mathrm{STED}} < 100mW$. We therefore conclude that for resolutions down to FWHM=60nm, a single scanning-FCS measurement can determine both the diffusion time as well as the diameter of the observation area independently. The increase of the diffusion coefficient for high STED intensities indicates that the FWHM is overestimated for resolutions below FWHM=60nm.

9.3. Reducing photobleaching artifacts

Next, we study in how far scanning STED-FCS allows for the observation of slowly diffusing particle such as large protein complexes. As previously discussed, a conventional STED-FCS recording is effectively limited by bleaching artifacts due to the increased light exposure of the slowly diffusing fluorophores on their passage through the excitation spot. In the following we thus compare if photobleaching is efficiently reduced in a scanning STED-FCS experiment.

As shown in figure 9.5, we record the correlation curves for increasing excitation intensities in a CTxB labeled SLB. In order to avoid distortion in the correlation curve due to initial photobleaching, we start each experiment with a short bleaching run. The average number of particles N within the observation area is thus observed to decrease in both the point as well as the scanning STED-FCS measurement for excitation intensities above 15 μW. In the scanning FCS recordings, we however observe, that the artificial decrease of the transient time in a point FCS experiment is effectively reversed over the entire range of applied excitation intensities and all probed observation areas.

The short dwell times in a scanning STED-FCS experiment therefore effectively prevent bleaching artifacts and allow for the direct investigation of slowly diffusing particles.

9.4. Scanning STED-FCS in unsupported model membranes

In the past, giant plasma membrane vesicles (GPMVs) have gained special attention in the field of membrane research [69]. GPMVs are directly extracted from the cell membrane by swelling procedures, and are thought to provide a unique model system featuring the native lipid and protein composition of the plasma membrane. Studying

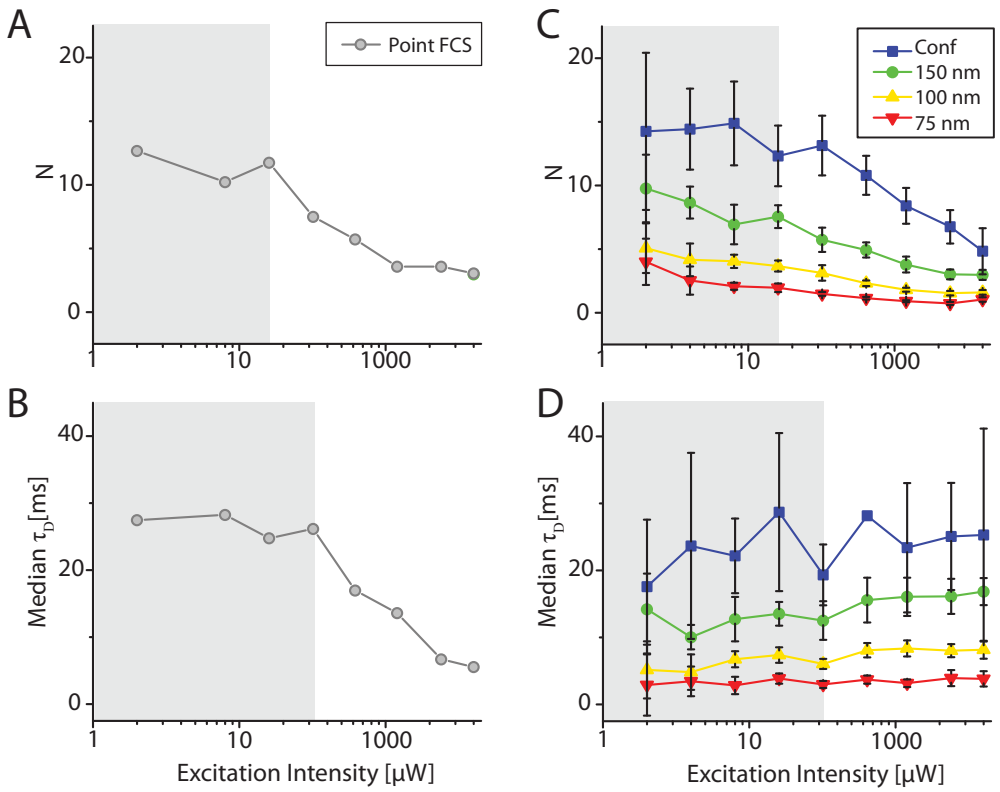

Figure 9.5.: Reducing artifacts due to bleaching: The diffusion time and average number of particles are plotted as a function of the excitation power. In comparison to the single point FCS experiment (grey dots), the diffusion time remains constant for increasing excitation power indicating a significant decrease of artifacts due to photobleaching. (Sample: SLB, DOPC/GM1, 1:0.01 + CTxB-KK114).

diffusion within a GPMV therefore allows us to evaluate nanoscale confinement without the superimposed influences of for instance the cytoskeleton of the cell. Since the first single-point STED-FCS experiments were hampered due to lateral drift of the unsupported membrane within the observation area, we evaluate in the following, if the short dwell times in a scanning STED-FCS experiment allow for a stable STED-FCS measurement within mobile GMPVs.

As shown in figure 9.6, we fluorescently label an GPI-anchor within the plasma membrane and induce cell swelling following a conventional GPMV preparation protocol described in detail in [69]. Scanning the excitation beam slowly across a selected membrane sphere, the obtained fluorescence image indicates a significant movement of the membrane due to thermally induced drift within the long imaging dwell times ($t_d = 50\mu$s). If the laser spot is, however, rapidly scanned across the membrane, we may measure the fluorescence along a circular trajectory with dwell times of the order of $t_d = 2\mu$s. The fluorescence signal is then used to reconstruct the recorded inten-

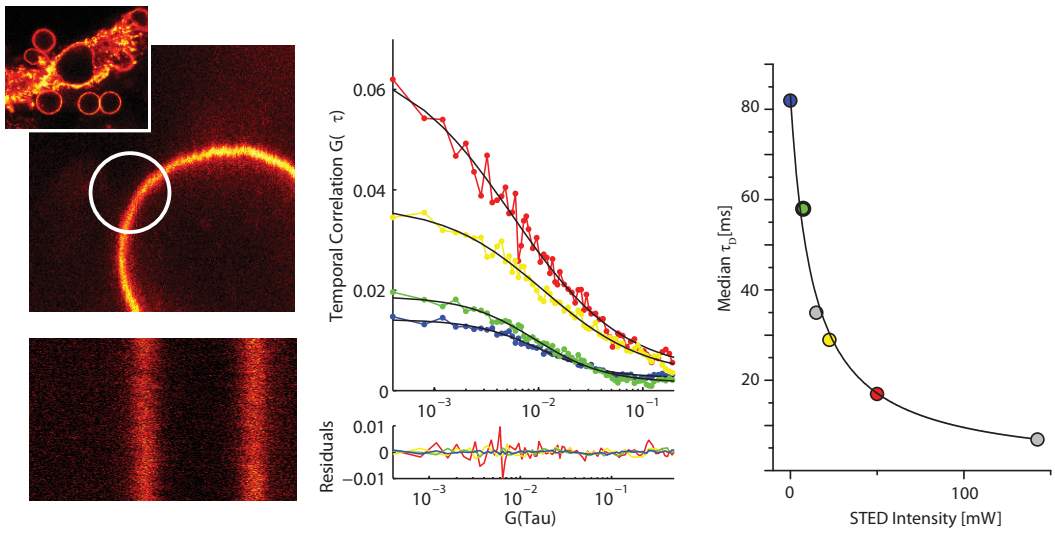

Figure 9.6.: Measuring the diffusion of the lipid GPI-anchor in a GPMV: (A) Scanning across the membrane vesicle, we average the fluorescence intensity from the membrane and calculate the correlation curves for various observation areas (B, see color coding for corresponding I_{STED}). The obtained transient times scale with the expected resolution of the STED experiment (Scan parameter: $R = 1\mu$m, $f = 3.3$kHz, $\Delta s = 15$nm, $T = 10$s).

sity as a function of position and time. In the pseudo-image, both passages of the membrane are clearly observed and the position of the membrane in each line can be corrected for motion or drift. Since the membrane position is, however, stable over the course of the experiment, we directly infer the fluorescence intensity trace without additional drift corrections. For each membrane passage, the fluorescence signal is calculated as the average fluorescence signal per line and all pixel comprising the membrane passage. Correlating the obtained intensity traces for decreasing observation areas, we determine the transient time as a function of the applied STED intensity. Interestingly we observe, that the diffusion times scale with the expected spatial resolution (fit, black line) and the GPI-anchor appears to diffuse rather unconstrained within a GPMVs.

We note, however, that the experiment is challenged by several constraints. First, the limited number of fluorophores within a GPMV, slowly depletes the pool of fluorophores throughout the experiment. All observed intensity traces thus need to be corrected for photobleaching as discussed in section 8.2.4. Secondly, the GPMVs are measured not directly at the surface of the cover glass but within the sample at a distance of a few μm. The increased distance from the oil objective introduces severe deviations of the observation volume as reflected in the significantly increased diffusion times of $\tau_D = 80ms$ for a confocal recording (GPI-anchor in native cell membrane:

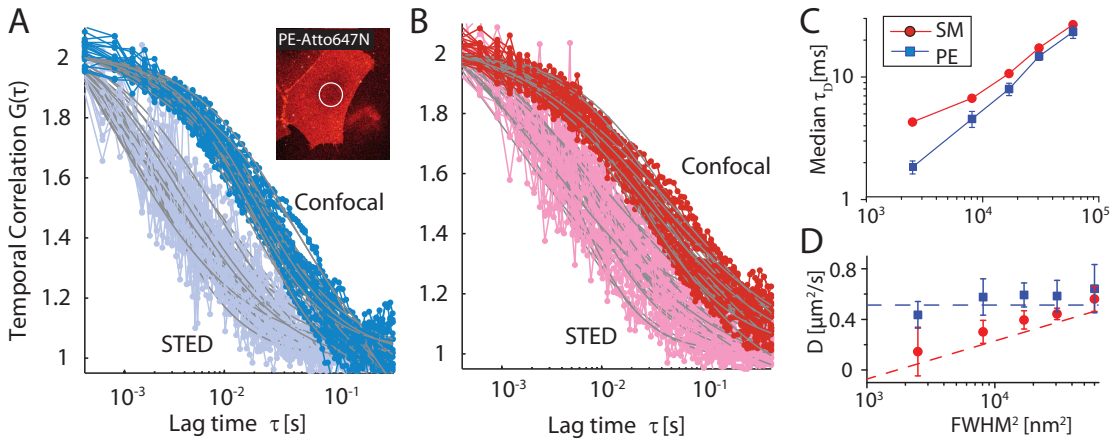

Figure 9.7.: Scanning STED-FCS diffusion law for PE and SM in the living cell: (A) The normalized correlation curves per pixel for a confocal and STED (dark and light color, respectively, FWHM(STED)= 70nm) measurement indicate a wide spatial variation of the recorded diffusion for both PE (blue) and SM (red). (B) The average transient times follow the characteristic FCS diffusion law for FWHM above 70 nm. Note, that the temporal resolution of the recording (0.3ms) is insufficient to resolve diffusion times below 2 ms. (Scan parameter: $R = 1\mu$m, $f = 3.3$kHz, $\Delta s = 15$nm , $T = 10$s).

$\tau_D = 25$ms).

9.5. Scanning STED-FCS in living cells

The heterogeneous organization of lipids within the membrane is assumed to evoke a variety of different cellular processes, such as for instance the formation of signaling platform. Therefore, it is especially interesting to determine if the observed nanoscale confinements are distributed evenly across the membrane.

Scanning the observation area across the membrane of a living cell stained with either PE- or SM-Atto647N, we record the diffusion dynamics simultaneously at various points across the scan trajectory. Correlating the fluorescence intensity for each pixel, we determine the average transient time and retrieve the apparent diffusion coefficients as plotted as a function of the observation area in figure 9.7. In line with the previously described point FCS experiments, confining the observation area reveals a constrained diffusion for SM due to transient molecular interactions, whereas the rather constant diffusion coefficient for PE is an indication for free diffusion. Despite of the high scan frequency of $f = 3.3$kHz, we note, however, that the temporal resolution is to low to accurately resolve the diffusion times below 2 ms. The measurements for PE

in observation areas below FWHM=70nm thus fail to resolve the expected diffusion times around 2 ms leading to an artificial drop of the apparent diffusion coefficient.

Next to the determination of the average diffusion, we are, however, in particular interested in the spatial distribution of the observed dynamics. Inspecting the normalized correlation curves for PE and SM, we directly note a broad variation of the correlation curves for both lipids. In order to visualize the spatial distribution of the variations in the correlations, we plot the recorded fluorescence intensity as well as the normalized correlation curves in a contour plot. Figure 9.8 compares the results for a STED recording (FWHM=70nm) of SM to the correlations recorded in a homogeneous SLB (FWHM=65nm). For both samples, the fluorescent intensity recordings do not reveal any spatial inhomogeneities along the scan trajectory. The normalized correlations however detect inhomogeneities in the diffusion which is especially pronounced for SM. In comparison to the rather homogeneous correlations in the SLB recording, the heterogeneous diffusion dynamics of SM suggest that the dynamics within the plasma membrane obey a complex spatial organization which are clearly resolved in a scanning STED-FCS experiment.

9.6. Discussion

In this section, we introduced the technical development of a scanning STED-FCS experiment. Scanning the observation area across the sample, we are able to retrieve the diffusion dynamics at various points along the scan trajectory.

An additional consideration of the spatiotemporal correlation further provides us with an accurate determination of the observation area and renders the complex calibration in a single spot STED-FCS experiment unnecessary. We note, however, that a reliable calibration-free experiment relies on an accurate determination of the effective scan trajectory and velocity beforehand. Especially for fast scan frequencies, we therefore need to account for the effective scan trajectory which is found to vary significantly in dependence on the applied scan parameters. Furthermore, the amplitude of the spatiotemporal correlation is observed to decrease rapidly within inhomogeneous samples if the particle number or diffusion dynamics vary along the scan trajectory. Therefore, the simultaneous determination of both the diffusion time as well as the size of the observation area can only be reliably retrieved for homogeneous samples as found for instance in model membranes.

The initial scanning STED-FCS experiments in unsupported model membranes revealed a significant reduction of the membrane mobility due to thermal drift and allow us to retrieve the diffusion dynamics within the mobile membrane part. The accurate determination of the diffusion times is however experimentally challenged

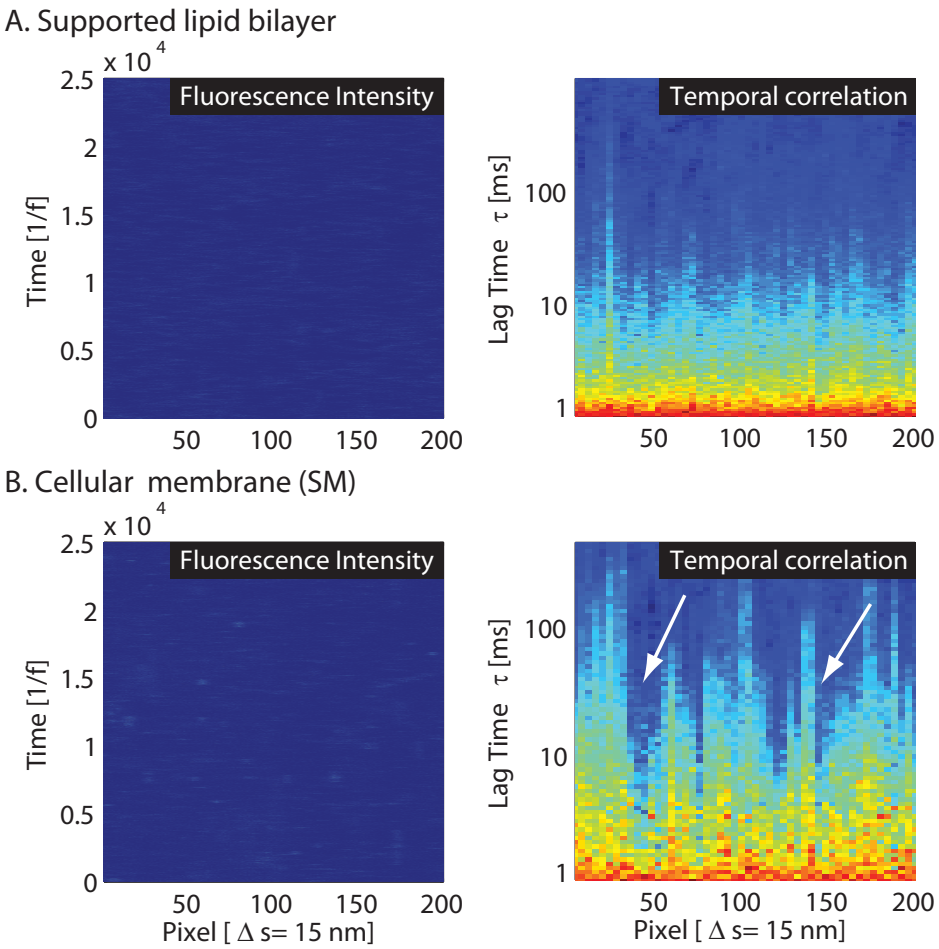

Figure 9.8.: Spatial distribution of diffusion dynamics: Scanning STED-FCS experiment measuring the diffusion of SM in the plasma membrane of a living cell cell membrane (B) in comparison to a SLB recording (A). While the intensity signal is homogeneously distributed along the scan trajectory, the normalized correlation curves reveal spatial variations in the diffusion time. These heterogeneities are especially pronounced in cellular membrane as indicated by the white arrow. (Scan parameter: $R = 1\mu$m, $f = 3.3$kHz, $\Delta s = 15$nm ,$T = 10$s, SLB, DOPC/GM1, 1:0.01 + CTxB-KK114).

due to the short working distance of the oil objective. The use of a glycerin objective would certainly be better suited for the observation of diffusion dynamics in GPMVs. Furthermore the experiment was impeded by a slow depletion of the limited pool of fluorophores within the GPMV which could only be partially corrected for with the implemented correction scheme. Despite these experimental challenges, the preliminary experiments indicate the unique potential of scanning STED-FCS to record diffusion dynamics within unsupported membrane systems.

First scanning STED-FCS experiments in living cells successfully retrieve the diffusion dynamics of lipids within the heterogeneous plasma membrane. The additional spatial information along the scan trajectory reveals a remarkable heterogeneity of the diffusion for a sphingolipid in comparison to a homogeneous model membrane. In combination with a suitable counterstain in a second fluorescence channel, these heterogeneities need to be addressed in more detail in future experiments. Since the observed lipid dynamic is however too fast to be reliably resolved in a scanning STED-FCS experiment, future advances need to focus on the observation of slowly diffusing particles. Especially for multimeric protein complexes, the recording in a scanning STED-FCS approach is well suited as it not only provides us valuable spatial information but is also found to significantly reduce bleaching artifacts which currently impede conventional single-spot STED-FCS experiments.

10. Conclusion and outlook

Scanning STED-FCS is a valuable extension to a conventional STED-FCS experiment and greatly broadens the range of applications in model systems as well as living cells.

While the information in a conventional STED-FCS experiment is only detected from a single observation area, the rapid scanning of the observation area across the sample plane allows us to simultaneously retrieve the diffusion characteristics from multiple points at a time. For a homogeneous sample, the simultaneous recording significantly increases the statistical accuracy and thus effectively shortens the required acquisition time. Especially for slowly diffusing particles, which typically require measurement times in the range of several hundreds of seconds, a decrease of the acquisition times, prevents measurement artifacts due to an unstable positioning of the sample within the observation area. For a heterogeneous sample, the additional information along the scan trajectory further allows us to resolve distinct regimes of diffusion and to visualize nanoscale heterogeneities in the dynamics.

Apart from the gain in statistical accuracy and spatial information, the continuous scan movement across the sample shortens the dwell times of the experiment. In comparison to a stationary STED-FCS measurement with acquisition times of 10-60 seconds, the sample in a scanning FCS experiment is only exposed to the excitation light for a few μs per scan. The decreased dwell times reduce artifacts due to photobleaching and prevent photothermal or -toxic damage of the living system. In particular, the reduced bleaching artifacts facilitate the observation of slowly diffusing particles which are prone to bleach during their long transients through the observation area. Furthermore, scanning STED-FCS could be successfully applied to measure the diffusion in unsupported model membranes such as giant plasma membrane vesicles. While conventional STED-FCS experiments in these mobile model membranes is impeded due to extensive drift of the membrane within the stationary observation spot, scanning the observation area not only reduces the thermally induced motion of the membrane but also allows for a drift correction within within subsequent scans.

Furthermore, the introduction of a spatiotemporal correlation in a scanning STED-FCS approach enables us to perform a calibration-free STED-FCS measurement. In contrast to a standard STED-FCS experiment, a calibration-free measurement does not rely on a previous characterization of the observation area in order to express the

obtained diffusion times in terms of the diffusion coefficients and further allows us to directly infer the diffusion dynamics in the form of the FCS diffusion law.

In the future, the unique potential of scanning STED-FCS to spatially map and distinguish different regimes of nanoscale diffusion offers a wide scope of novel applications. Future experiments in particularly aim for an elucidation of the complex interplay between membrane lipids and membrane-anchored proteins. A promising experimental approach to quantitatively assess the degree of lipid-protein interactions involves the use of micro-patterned cover glasses which allow us to artificially control the lateral distribution of specific membrane lipids and proteins in specific regions of the plasma membrane [125]. These well defined regions may, for instance, be enriched in GM1 and allow us to study if the artificially induced GM1 clusters significantly alter the diffusion dynamics of the surrounding lipids.

Further advances in scanning STED-FCS will include the study of slowly diffusing multimeric membrane receptors as, for instance, the epidermal growth factor receptor (EGF-R). The EGF-R is known to plays a crucial role in cellular signaling and is found to be activated upon ligand binding by dimerization of two inactive monomeric subunits. Since recent studies suggest that the activation process is regulated by lipids and especially gangliosides [97], a direct quantification of the activation kinetics by scanning STED-FCS would be as interesting as a spatial mapping of lipid dynamics in close proximity to the receptors. Both experiments might provide us with valuable insights towards a consistent understanding of the functionality and role of lipid-lipid and lipid-protein interaction in cellular processes.

Appendix

Derivation of FCS theory

In order to derive the theoretical description for the autocorrelation function of the intensity trace recorded in a FCS experiment, we follow the classical derivation line by Elson and Magde [61].

The autocorrelation function $G(\tau)$ describes the similarity of the fluorescence fluctuations $\delta F(t)$ at time t to the signal at times $t+\tau$. It is defined as the temporal average of the product of the fluorescence fluctuations at time t and the delayed time $t+\tau$ normalized by the squared average of the fluorescence signal $F(t)$:

$$G(\tau) = \frac{\langle \delta F(t) \delta F(t+\tau) \rangle}{\langle F(t) \rangle^2} \tag{.1}$$

In order to derive a theoretical model of $G(\tau)$, we need to express the fluorescence fluctuations $\delta F(t)$ in terms of physical parameters of the system. Neglecting fluctuations of the optical system's properties, we can consider the fluorescence fluctuations to be merely caused by local concentration fluctuations in the probe volume. For an ideal solution of m components, we therefore find that the fluorescence fluctuations are directly proportional to the concentration fluctuations $\delta C_i(\vec{r},t) = C_i(\vec{r},t) - \bar{C}_i$ around the average concentration $\bar{C}_i = \langle C_i(\vec{r},t) \rangle$ of each component i:

$$\delta F(t) = \int \sum_{i=1}^{m} \phi_i(\vec{r}) \delta C_i(\vec{r},t) \tag{.2}$$

The proportionality constant $\phi_i(\vec{r})$ is called the "detectivity" of the system and it depends on sample properties, such as the absorption cross section σ_i and the quantum yield q of the component as well as on optical properties such as the usually inhomogeneous illumination profile I_{ex}, the optical transfer function of the detection system $\mathrm{OFT}(\tilde{\mathrm{r}})$ and the detection efficiency η.

We simplify equation .2 by combining the spatial variables to a single description of the optical systems' geometrical properties, called the point spread function $\mathrm{PSF}(\tilde{\mathrm{r}}) = \mathrm{I}_{\mathrm{ex}}(\tilde{\mathrm{r}})/\mathrm{I}_0 \cdot \mathrm{OFT}(\tilde{\mathrm{r}})$, where I_0 denotes the illumination intensity at the center of the focal spot. We are now able to separate the detectivity ϕ_i into a spatial contribution that

is time independent and equal for all components and a component dependent contribution $\tilde{\epsilon}_i = I_0 \eta \sigma_i q_i$, that denotes the photon count rate per molecule per second:

$$\delta F(t) = \int \mathrm{PSF}(\tilde{\mathrm{r}}) \sum_{\mathrm{i}=1}^{\mathrm{m}} \tilde{\epsilon}_{\mathrm{i}} \delta \mathrm{C}_{\mathrm{i}}(\tilde{\mathrm{r}}, \mathrm{t}). \tag{.3}$$

Inserting this relation into the correlation function from equation .1 yields

$$G(\tau) = \frac{\int\int PSF(\vec{r}) PSF(\vec{r}') \sum_{i,j} \epsilon_i \epsilon_j \left\langle \delta C_i(\vec{r}, t) \delta C_j(\vec{r'}, t+\tau) \right\rangle d^3 r d^3 r'}{\left[\sum_i \tilde{\epsilon}_i \bar{C}_i \int PSF(\vec{r}) d^3 r\right]^2} \tag{.4}$$

In order to determine the samples physical properties from this equation we need to consider the concentration fluctuations δC_i in more detail. In an open system with m components at thermodynamic equilibrium, the concentration of each component continually fluctuates around the average concentration. These thermal fluctuations are mainly caused by either diffusion of particles in and out of the probe volume or in situ chemical reactions. Neglecting chemical reactions of the particles, the temporal evolution of these local concentration fluctuation are solely governed by the diffusion kinetics of the particle:

$$\frac{\partial C_i(\vec{r}, t)}{\partial t} = D_i \nabla^2 \delta C_i(\vec{r}, t) \tag{.5}$$

where D denotes the diffusion coefficient of the particle.

This differential equation is used to express $\delta C_i(\vec{r'}, t+\tau)$ as a function of $(\vec{r''}, t)$ for the special case $t = 0$ by deriving the solutions as a function of the initial conditions $\delta C_i(\vec{r''}, 0)$. Applying a Fourier transform to the differential equations allows us to solve .5 and we obtain

$$\widetilde{\delta C}_i(\vec{q}, t) = \widetilde{\delta C}_i(\vec{q}, 0) \exp(-D_i q^2 t) \tag{.6}$$

given as the fourier transform $\widetilde{\delta C}_i(\vec{q}, t) = (2\pi)^{-2/3} \int exp(i\vec{q}\vec{r}) \delta C_i(\vec{r}, t) d^3 r$.

In .4, we now express $\delta C_j(\vec{r'}, \tau)$ as the inverse Fourier transform $\widetilde{\delta C}_j(\vec{q}, \tau)$. The latter one is then written as function of the initial condition $\widetilde{\delta C}_i(\vec{q}, 0)$ expressed by the Fourier transform of $\delta C_j(\vec{r''}, 0)$.

Finally, we apply the fact that the Fourier transform and the temporal average are interchangeable which allows us to simplify the temporal average $\left\langle \delta C_i(\vec{r}, 0) \delta C_j(\vec{r''}, 0) \right\rangle = \bar{C}_i \delta_{ij} \delta(r - r''))$ which reduces .4 to

$$G(\tau) = (2\pi)^{-3} \frac{\int |\widetilde{\mathrm{PSF}}(\vec{q})|^2 \sum_{i,j} \tilde{\epsilon}_i \tilde{\epsilon}_j \bar{C}_i \exp(-D_j q^2 \tau) d^3 q}{\left[\sum_i \tilde{\epsilon}_i \bar{C}_i \int PSF(\vec{r}) d^3 r\right]^2} \tag{.7}$$

Assuming a 3D Gaussian point spread function the Fourier transform of the PSF calculates as

$$\widetilde{\mathrm{PSF}}(\vec{q}) = \frac{w_r^2 w_z}{8} \exp\left(-\frac{w_r^2}{8}(q_x^2+q_y^2) - \frac{(2\pi)^{-3} w_z^2}{8} q_z^2\right) \tag{.8}$$

where w_r and w_z denote the axial and lateral radius of the observation volume at which the intensity has dropped to I_0/e^2.

For a single species, we can solve the autocorrelation function by inserting .8 in .7

$$\begin{aligned} G(\tau) &= \frac{\tilde{\epsilon}^2 \bar{C} w_r^2 w_z}{16\pi^3 \tilde{\epsilon}^2 \bar{C}^2 \left[(\pi/2)^{3/2} w_r^2 w_z\right]^2} && (.9)\\ &\quad \cdot \int \exp\left(-\frac{w_r^2}{4}(q_x^2+q_y^2) - \frac{w_z^2}{4} q_z^2 - D\tau((q_x^2+q_y^2+q_z^2)\right) d^3q && (.10)\\ &= \frac{1}{\bar{C}\left[8\pi^6 w_r^2 w_z\right]} \left[\int \exp\left(-\left(\frac{w_r^2}{4}+D\tau\right) q_x^2\right) dq_x\right]^2 && (.11)\\ &\quad \cdot \int \exp\left(-\left(\frac{w_z^2}{4}+D\tau\right) q_z^2\right) dq_z && (.12)\\ &= \frac{\pi^{3/2}}{\bar{C}\left[\pi^{3/2} w_r^2 w_z\right]} \left(\frac{w_r^2}{4}+D\tau\right)^{-1} \left(\frac{w_z^2}{4}+D\tau\right)^{-1/2} && (.13) \end{aligned}$$

Using the definition for the diffusion time $\tau_D = w_r^2/4D$ and the structure parameter $s = w_z/w_r$, we finally obtain the mathematical expression for the autocorrelation function

$$G(\tau) = \frac{1}{\bar{N}} \left(1+\frac{\tau}{\tau_D}\right)^{-1} \left(1+\frac{\tau}{s^2\tau_D}\right)^{-1/2} \tag{.14}$$

where $\bar{N} = \bar{C} V_{obs}$ denotes the average number of particles inside the observation volume $V_{\mathrm{obs}} = \pi^{3/2} w_r^2 w_z$.

Scientific contributions

Parts of this thesis have been published as follows:

1. Mueller, V., C. Ringemann, A. Honigmann, G. Schwarzmann, R. Medda, M. Leutenegger, S. Polyakova, V.N. Belov, S.W. Hell and C. Eggeling: "STED Nanoscopy Reveals Molecular Details of Cholesterol- and Cytoskeleton-Modulated Lipid Interactions in Living Cells" *Biophys. J.* 101, 1651-1660, (2011)

2. Sezgin, E., Levental, I., Grzybek, M., Schwarzmann, G., Mueller, V., Honigmann, A., Belov, VN., Eggeling, C., Coskun, U., Simons, K., Schwille, P. "Partitioning, diffusion, and ligand binding of raft lipid analogs in model and cellular plasma membranes" *Biochim Biophys Acta* 1818,7, 1777-84, (2012)

Talks and posters presented at international conferences:

1. V.Mueller, A. Honigmann, S.W. Hell and C. Eggeling; "STED nanoscopy reveals molecular details of lipid interactions in living cells", *EuroMEMBRANE Workshop, Turku, Finland* (Talk and poster presentation, March 2012).

2. V.Mueller, R. Medda, M. Leutenegger, C. Eggeling, S.W. Hell; "Molecular interactions in the plasma membrane studied by STED Fluorescence Microscopy", *55th Annual Meeting of the Biophysical Society, Baltimore, USA* (Poster presentation, March 2011).

3. V.Mueller, C. Ringemann, R. Medda, S.W. Hell and C. Eggeling; " Nanoscale membrane diffusion revealed by STED-FCS", *Annual Meeting of the German Biophysical Society 2010, Bochum, Germany* (Poster presentation, October 2010).

4. V.Mueller, R. Medda, M. Leutenegger, S.W. Hell and C. Eggeling; "STED-FCS reveals membrane interactions in living cells", *16th International Workshop on Single Molecule Spectroscopy and Ultrasensitive Analysis in the Life Sciences, Berlin Adlershof, Germany* (Poster presentation, September 2010).

5. V.Mueller, C. Ringemann, R. Medda, S.W. Hell and C. Eggeling; "Influences on the diffusion dynamics of lipid rafts revealed by STED-FCS", *Annual Meeting of the German Physical Society 2010, Regensburg, Germany* (Talk, March 2010)

6. V.Mueller, C. Ringemann, R. Medda, S.W. Hell and C. Eggeling; "Exploring the nanoscale: dynamics of lipid rafts revealed by STED-FCS", *15th International Workshop on Single Molecule Spectroscopy and Ultrasensitive Analysis in the Life Sciences, Berlin Adlershof, Germany* (Talk, September 2009)

Acknowledgments

I would like to thank all the various people who have contributed to the success of this dissertation and supported me during my work.

First and foremost, I thank Prof. Dr. Dr. h.c. Stefan W. Hell who gave me the opportunity to work on this fascinating, yet challenging project. His continuous support and fruitful ideas were a valuable guidance and motivation throughout my work. I am deeply thankful for the unique scientific research environment that he provides, and highly appreciate his trust which allowed me to follow my own ideas and paths.

I would like to thank Prof. Dr. Rainer Fink from the *Institut für Physiologie und Pathophysiologie* at the University of Heidelberg for his interest in my work and for offering to referee my thesis.

I am very thankful to Dr. Christian Eggeling for the supervision of this work. He not only proposed the project, but also constantly encouraged me over the time. His creative ideas and his advice were of great value and helped me whenever help was needed. I really enjoyed all the stimulating discussions about the never-ending list of possible projects, neatly scribbled on little yellow post-it notes.

I would also like to thank

- Dr. Christian Ringemann for introducing me to the challenges of STED-FCS and teaching me his pragmatic and unconventional ways of building an experimental setup.
- Dr. Alf Honigmann for his valuable support and insights into the preparation of artificial membrane systems as well as his constant criticism which pushed me to my limits in the lab as well as the climbing gym.
- Dr. Rebecca Medda, Tanja Gilat and Dr. Ellen Rothermel for their patience in answering me any biological question and their substantial help with cell culture and sample preparation.
- Dr. Birka Lalkens and Dr. Katrin Willig for sharing their experience in fluorescent labeling and introducing me into the art of OPO alignment.
- Dr. Vladimir Belov and his team for the synthesis of the fluorescent lipid analogs and all their help concerning chemical questions.

- Dr. Ilya Levental from the Max Planck Institute for Cell Biology and Genetics for the fruitful cooperation and providing us his LAT constructs.
- Dr. Andreas Schönle, Dr. Sebastian Berning and Dr. Marcel Leutenegger for their support in the realization of the scanning STED-FCS data acquisition as well as simulation algorithms.
- Jaydev Jethwa and Harald Meyer for their technical assistance and helpful advice.
- Dr. Mark Bates, Dr. Chaitanya Ullal, Jaydev Jethwa, Nicolai Urban, Dr. Peter Orth and Volker Mueller for critical proof-reading of parts of this thesis.
- Dr. Ilaria Testa and Dr. Giuseppe Vicidomini per condividere le loro capsule di caffe con me.
- All former and current members of the department of NanoBiophotonics for their constant support and all the numerous scientific and non-scientific discussions.
- My family, especially my grandmother and Peter for their constant support, the thoughtful supply with care packages and everything else.

Bibliography

[1] E. Abbe, "Beiträge zur Theorie des Mikroskops und der mikroskopischen Wahrnehmung," *Archiv für Mikroskopische Anatomie* **9**, 413 (1873).

[2] S. W. Hell and J. Wichmann, "Breaking the diffraction resolution limit by stimulated emission: stimulated-emission-depletion fluorescence microscopy," *Optics Letters* **19**, 780 (1994).

[3] S. W. Hell, "Far-Field Optical Nanoscopy," *Science* **316**, 1153 (2007).

[4] M. Dyba and S. W. Hell, "Focal Spots of Size $\lambda/23$ Open Up Far-Field Florescence Microscopy at 33 nm Axial Resolution," *Physical Review Letters* **88**, 163901 (2002).

[5] M. Hofmann, C. Eggeling, S. Jakobs, and S. W. Hell, "Breaking the Diffraction Barrier in Fluorescence Microscopy at Low Light Intensities by Using Reversibly Photoswitchable Proteins," *Proceedings of the National Academy of Sciences of the United States of America* **102**, 17565 (2005).

[6] M. G. L. Gustafsson, "Nonlinear Structured-Illumination Microscopy: Wide-Field Fluorescence Imaging with Theoretically Unlimited Resolution," *Proceedings of the National Academy of Sciences of the United States of America* **102**, 13081 (2005).

[7] E. Betzig, G. H. Patterson, R. Sougrat, O. W. Lindwasser, S. Olenych, J. S. Bonifacino, M. W. Davidson, J. Lippincott-Schwartz, and H. F. Hess, "Imaging Intracellular Fluorescent Proteins at Nanometer Resolution," *Science* **313**, 1642 (2006).

[8] S. T. Hess, T. P. Girirajan, and M. D. Mason, "Ultra-High Resolution Imaging by Fluorescence Photoactivation Localization Microscopy," *Biophysical Journal* **91**, 4258 (2006).

[9] M. J. Rust, M. Bates, and X. Zhuang, "Sub-diffraction-limit imaging by stochastic optical reconstruction microscopy (STORM)," *Nature Methods* **3**, 793 (2006).

[10] K. I. Willig, S. O. Rizzoli, V. Westphal, R. Jahn, and S. W. Hell, "STED microscopy reveals that synaptotagmin remains clustered after synaptic vesicle exocytosis," *Nature* **440**, 935 (2006).

[11] V. Westphal, S. O. Rizzoli, M. A. Lauterbach, D. Kamin, R. Jahn, and S. W. Hell, "Video-Rate Far-Field Optical Nanoscopy Dissects Synaptic Vesicle Movement," *Science* **320**, 246 (2008).

[12] P. Kanchanawong, G. Shtengel, A. M. Pasapera, E. B. Ramko, M. W. Davidson, H. F. Hess, and C. M. Waterman, "Nanoscale architecture of integrin-based cell adhesions," *Nature* **468**, 580 (2010).

[13] A. Dani, B. Huang, J. Bergan, C. Dulac, and X. Zhuang, "Superresolution Imaging of Chemical Synapses in the Brain," *Neuron* **68**, 843 (2010).

[14] S. A. Jones, S. Shim, J. He, and X. Zhuang, "Fast, three-dimensional super-resolution imaging of live cells," *Nature Methods* **8**, 499 (2011).

[15] M. A. Lauterbach, C. K. Ullal, V. Westphal, and S. W. Hell, "Dynamic Imaging of Colloidal-Crystal Nanostructures at 200 Frames per Second," *Langmuir* **26**, 14400 (2010).

[16] C. Eggeling, C. Ringemann, R. Medda, G. Schwarzmann, K. Sandhoff, S. Polyakova, V. N. Belov, B. Hein, C. von Middendorff, A. Schönle, and S. W. Hell, "Direct observation of the nanoscale dynamics of membrane lipids in a living cell," *Nature* **457**, 1159 (2009).

[17] M. Leslie, "Do Lipid Rafts Exist?," *Science* **334**, 1046 (2011).

[18] P. Yeagle, *The Membranes of Cells*, 2nd revised edition ed. (Academic Press Inc, 1994).

[19] L. Stryer, J. M. Berg, and J. L. Tymoczko, *Biochemistry*, 5th revised edition ed. (W.H.Freeman & Co Ltd, 2002).

[20] D. L. Nelson and M. Cox, *Lehninger Principles of Biochemistry, 3rd Ed.*, 3rd revised edition ed. (Worth Publishers Inc.,U.S., 2000).

[21] J. C. M. Holthuis and T. P. Levine, "Lipid traffic: floppy drives and a superhighway," *Nature Reviews Molecular Cell Biology* **6**, 209 (2005).

[22] J. Holthuis, T. Pomorski, R. Raggers, H. Sprong, and G. Van Meer, "The organizing potential of sphingolipids in intracellular membrane transport," *Physiological Reviews* **81**, 1689 (2001).

[23] S. Singer, "The proteins of membranes," *Journal of Colloid And Interface Science* **58**, 452 (1977).

[24] S. Munro, "Lipid Rafts: Elusive or Illusive?," *Cell* **115**, 377 (2003).

[25] K. Jacobson, O. G. Mouritsen, and R. G. W. Anderson, "Lipid rafts: at a crossroad between cell biology and physics," *Nature Cell Biology* **9**, 7 (2007).

[26] S. Singer and G. Nicolson, "The fluid mosaic model of the structure of cell membranes," *Science* **175**, 720 (1972).

[27] K. Simons and G. Van Meer, "Lipid sorting in epithelial cells," *Biochemistry* **27**, 6197 (1988).

[28] D. Brown and J. Rose, "Sorting of GPI-anchored proteins to glycolipid-enriched membrane subdomains during transport to the apical cell surface," *Cell* **68**, 533 (1992).

[29] R. Schroeder, S. Ahmed, Y. Zhu, E. London, and D. Brown, "Cholesterol and sphingolipid enhance the Triton X-100 insolubility of glycosylphosphatidylinositol-anchored proteins by promoting the formation of detergent-insoluble ordered membrane domains," *Journal of Biological Chemistry* **273**, 1150 (1998).

[30] K. Simons and E. Ikonen, "Functional rafts in cell membranes," *Nature* **387**, 569 (1997).

[31] K. Simons and D. Toomre, "Lipid rafts and signal transduction," *Nature Reviews Molecular Cell Biology* **1**, 31 (2000).

[32] M. F. Hanzal-Bayer and J. F. Hancock, "Lipid rafts and membrane traffic," *FEBS Letters* **581**, 2098 (2007).

[33] L. J. Pike, "Rafts Defined: A Report on the Keystone Symposium on Lipid Rafts and Cell Function," *Journal of Lipid Research* **47**, 1597 (2006).

[34] J. A. Allen, R. A. Halverson-Tamboli, and M. M. Rasenick, "Lipid raft microdomains and neurotransmitter signalling," *Nature Reviews Neuroscience* **8**, 128 (2006).

[35] A. S. Shaw, "Lipid rafts: now you see them, now you don't," *Nature Immunology* **7**, 1139 (2006).

[36] L. J. Pike, "The challenge of lipid rafts," *The Journal of Lipid Research* **50**, S323 (2008).

[37] A. Kusumi, Y. Sako, and M. Yamamoto, "Confined lateral diffusion of membrane receptors as studied by single particle tracking (nanovid microscopy). Effects of calcium-induced differentiation in cultured epithelial cells," *Biophysical Journal* **65**, 2021 (1993).

[38] T. Fujiwara, K. Ritchie, H. Murakoshi, K. Jacobson, and A. Kusumi, "Phospholipids Undergo Hop Diffusion in Compartmentalized Cell Membrane," *The Journal of Cell Biology* **157**, 1071 (2002).

[39] K. Ritchie, R. Iino, T. Fujiwara, K. Murase, and A. Kusumi, "The fence and picket structure of the plasma membrane of live cells as revealed by single molecule techniques (Review)," *Molecular Membrane Biology* **20**, 13 (2003), PMID: 12745919.

[40] S. Bussell, D. Koch, and D. Hammer, "Effect of hydrodynamic interactions on the diffusion of integral membrane proteins: Diffusion in plasma membranes," *Biophysical Journal* **68**, 1836 (1995).

[41] A. Kusumi, K. G. Suzuki, R. S. Kasai, K. Ritchie, and T. K. Fujiwara, "Hierarchical mesoscale domain organization of the plasma membrane," *Trends in Biochemical Sciences* **36**, 604 (2011).

[42] D. A. Brown and E. London, "Functions of Lipid Rafts in Biological Membranes," *Annual Review of Cell and Developmental Biology* **14**, 111 (1998).

[43] K. Simons and M. J. Gerl, "Revitalizing membrane rafts: new tools and insights," *Nature Reviews Molecular Cell Biology* **11**, 688 (2010).

[44] D. Lingwood and K. Simons, "Lipid Rafts As a Membrane-Organizing Principle," *Science* **327**, 46 (2010).

[45] J. Yu, D. Fischman, and T. Steck, "Selective solubilization of proteins and phospholipids from red blood cell membranes by nonionic detergents," *Journal of Supramolecular and Cellular Biochemistry* **1**, 233 (1973).

[46] D. Lingwood and K. Simons, "Detergent resistance as a tool in membrane research," *Nature Protocols* **2**, 2159 (2007).

[47] M. le Maire, P. Champeil, and J. V. Møller, "Interaction of membrane proteins and lipids with solubilizing detergents," *Biochimica et Biophysica Acta (BBA) - Biomembranes* **1508**, 86 (2000).

[48] D. A. Brown, "Lipid Rafts, Detergent-Resistant Membranes, and Raft Targeting Signals," *Physiology* **21**, 430 (2006).

[49] C. Chen, O. Martin, and R. Pagano, "Changes in the spectral properties of a plasma membrane lipid analog during the first seconds of endocytosis in living cells," *Biophysical Journal* **72**, 37 (1997).

[50] S. Mayor, K. Rothberg, and F. Maxfield, "Sequestration of GPI-anchored proteins in caveolae triggered by cross- linking," *Science* **264**, 1948 (1994).

[51] A. K. Kenworthy, B. J. Nichols, C. L. Remmert, G. M. Hendrix, M. Kumar, J. Zimmerberg, and J. Lippincott-Schwartz, "Dynamics of Putative Raft-Associated Proteins at the Cell Surface," *The Journal of Cell Biology* **165**, 735 (2004).

[52] O. O. Glebov and B. J. Nichols, "Lipid raft proteins have a random distribution during localized activation of the T-cell receptor," *Nature Cell Biology* **6**, 238 (2004).

[53] P. Sharma, R. Varma, R. Sarasij, Ira, K. Gousset, G. Krishnamoorthy, M. Rao, and S. Mayor, "Nanoscale Organization of Multiple GPI-Anchored Proteins in Living Cell Membranes," *Cell* **116**, 577 (2004).

[54] F. Pinaud, X. Michalet, G. Iyer, E. Margeat, H. Moore, S. Weiss, F. Pinaud, X. Michalet, G. Iyer, E. Margeat, H. Moore, and S. Weiss, "Dynamic Partitioning of a Glycosyl-Phosphatidylinositol-Anchored Protein in Glycosphingolipid-Rich Microdomains Imaged by Single-Quantum Dot Tracking, Dynamic Partitioning of a Glycosyl-Phosphatidylinositol-Anchored Protein in Glycosphingolipid-Rich Microdomains Imaged by Single-Quantum Dot Tracking," *Traffic, Traffic* **10, 10**, 691, 691 (2009).

[55] P. Schwille, J. Korlach, and W. W. Webb, "Fluorescence correlation spectroscopy with single-molecule sensitivity on cell and model membranes," *Cytometry* **36**, 176 (1999).

[56] K. Bacia, D. Scherfeld, N. Kahya, and P. Schwille, "Fluorescence Correlation Spectroscopy Relates Rafts in Model and Native Membranes," *Biophysical Journal* **87**, 1034 (2004).

[57] S. Chiantia, J. Ries, and P. Schwille, "Fluorescence correlation spectroscopy in membrane structure elucidation," *Biochimica et Biophysica Acta (BBA) - Biomembranes* **1788**, 225 (2009).

[58] L. Onsager, "Reciprocal Relations in Irreversible Processes. I.," *Physical Review* **37**, 405 (1931).

[59] D. Magde, E. Elson, and W. W. Webb, "Thermodynamic Fluctuations in a Reacting System—Measurement by Fluorescence Correlation Spectroscopy," *Physical Review Letters* **29**, 705 (1972).

[60] D. Magde, E. L. Elson, W. W. Webb, D. Magde, E. L. Elson, and W. W. Webb, "Fluorescence correlation spectroscopy. II. An experimental realization, Fluorescence correlation spectroscopy. II. An experimental realization," *Biopolymers, Biopolymers* **13, 13**, 29, 29 (1974).

[61] E. L. Elson, D. Magde, E. L. Elson, and D. Magde, "Fluorescence correlation spectroscopy. I. Conceptual basis and theory, Fluorescence correlation spectroscopy. I. Conceptual basis and theory," *Biopolymers, Biopolymers* **13, 13**, 1, 1 (1974).

[62] H. He and D. Marguet, "Detecting Nanodomains in Living Cell Membrane by Fluorescence Correlation Spectroscopy," *Annual Review of Physical Chemistry* **62**, 417 (2011).

[63] E. Haustein and P. Schwille, "Ultrasensitive investigations of biological systems by fluorescence correlation spectroscopy," *Methods* **29**, 153 (2003).

[64] A. J. García-Sáez and P. Schwille, "Fluorescence correlation spectroscopy for the study of membrane dynamics and protein/lipid interactions," *Methods* **46**, 116 (2008).

[65] K. Bacia, S. A. Kim, and P. Schwille, "Fluorescence cross-correlation spectroscopy in living cells," *Nature Methods* **3**, 83 (2006).

[66] T. Dertinger, V. Pacheco, I. von der Hocht, R. Hartmann, I. Gregor, and J. Enderlein, "Two-Focus Fluorescence Correlation Spectroscopy: A New Tool for Accurate and Absolute Diffusion Measurements, Two-Focus Fluorescence Correlation Spectroscopy: A New Tool for Accurate and Absolute Diffusion Measurements," *ChemPhysChem, ChemPhysChem* **8, 8**, 433, 433 (2007).

[67] S. Chiantia, J. Ries, N. Kahya, P. Schwille, S. Chiantia, J. Ries, N. Kahya, and P. Schwille, "Combined AFM and Two-Focus SFCS Study of Raft-Exhibiting Model Membranes, Combined AFM and Two-Focus SFCS Study of Raft-Exhibiting Model Membranes," *ChemPhysChem, ChemPhysChem* **7, 7**, 2409, 2409 (2006).

[68] J. Ries, S. Chiantia, and P. Schwille, "Accurate Determination of Membrane Dynamics with Line-Scan FCS," *Biophysical Journal* **96**, 1999 (2009).

[69] D. Lingwood, J. Ries, P. Schwille, and K. Simons, "Plasma Membranes Are Poised for Activation of Raft Phase Coalescence at Physiological Temperature," *Proceedings of the National Academy of Sciences* **105**, 10005 (2008).

[70] E. Gielen, N. Smisdom, M. vandeVen, B. De Clercq, E. Gratton, M. Digman, J. Rigo, J. Hofkens, Y. Engelborghs, and M. Ameloot, "Measuring Diffusion of Lipid-like Probes in Artificial and Natural Membranes by Raster Image Correlation Spectroscopy (RICS): Use of a Commercial Laser-Scanning Microscope with Analog Detection," *Langmuir* **25**, 5209 (2009).

[71] L. Wawrezinieck, H. Rigneault, D. Marguet, and P. Lenne, "Fluorescence Correlation Spectroscopy Diffusion Laws to Probe the Submicron Cell Membrane Organization," *Biophysical Journal* **89**, 4029 (2005).

[72] P. Lenne, L. Wawrezinieck, F. Conchonaud, O. Wurtz, A. Boned, X. Guo, H. Rigneault, H. He, and D. Marguet, "Dynamic molecular confinement in the plasma membrane by microdomains and the cytoskeleton meshwork," *The EMBO Journal* **25**, 3245 (2006).

[73] A. Einstein, "Strahlungs-emission und -absorption nach der Quantentheorie," *Verhandlungen der Deutschen Physikalischen Gesellschaft* **1**, 318 (1916).

[74] B. Harke, J. Keller, C. K. Ullal, V. Westphal, A. Schonle, and S. W. Hell, "Resolution scaling in STED microscopy," *Optics Express* **16**, 4154 (2008).

[75] L. Kastrup, H. Blom, C. Eggeling, and S. W. Hell, "Fluorescence Fluctuation Spectroscopy in Subdiffraction Focal Volumes," *Physical Review Letters* **94**, 178104 (2005).

[76] C. Ringemann, B. Harke, C. von Middendorff, R. Medda, A. Honigmann, R. Wagner, M. Leutenegger, A. Schönle, S. W Hell, and C. Eggeling, "Exploring single-molecule dynamics with fluorescence nanoscopy," *New Journal of Physics* **11**, 103054 (2009).

[77] S. Chiantia, N. Kahya, and P. Schwille, "Dehydration Damage of Domain-Exhibiting Supported Bilayers: An AFM Study on the Protective Effects of Disaccharides and Other Stabilizing Substances," *Langmuir* **21**, 6317 (2005).

[78] C. Eggeling, C. Ringemann, R. Medda, G. Schwarzmann, K. Sandhoff, S. Polyakova, V. N. Belov, B. Hein, C. v. Middendorff, A. Sch|[ouml]|nle, and S. W. Hell, "Direct observation of the nanoscale dynamics of membrane lipids in a living cell," *Nature* **457**, 1159 (2008).

[79] S. M. Polyakova, V. N. Belov, S. F. Yan, C. Eggeling, C. Ringemann, G. Schwarzmann, A. de Meijere, and S. W. Hell, "New GM1 Ganglioside Derivatives for Selective Single and Double Labelling of the Natural Glycosphingolipid Skeleton," *European Journal of Organic Chemistry* **2009**, 5162 (2009).

[80] B. Hein, K. I. Willig, and S. W. Hell, "Stimulated Emission Depletion (STED) Nanoscopy of a Fluorescent Protein-Labeled Organelle Inside a Living Cell," *Proceedings of the National Academy of Sciences* **105**, 14271 (2008).

[81] M. R. Bubb, I. Spector, B. B. Beyer, and K. M. Fosen, "Effects of Jasplakinolide on the Kinetics of Actin Polymerization AN EXPLANATION FOR CERTAIN IN VIVO OBSERVATIONS," *Journal of Biological Chemistry* **275**, 5163 (2000).

[82] N. L. Thompson, A. M. Lieto, and N. W. Allen, "Recent advances in fluorescence correlation spectroscopy," *Current Opinion in Structural Biology* **12**, 634 (2002).

[83] P. Kask, K. Palo, D. Ullmann, and K. Gall, "Fluorescence-Intensity Distribution Analysis and Its Application in Biomolecular Detection Technology," *Proceedings of the National Academy of Sciences* **96**, 13756 (1999).

[84] Y. Chen, J. D. Müller, P. T. So, and E. Gratton, "The Photon Counting Histogram in Fluorescence Fluctuation Spectroscopy," *Biophysical Journal* **77**, 553 (1999).

[85] J. D. Müller, "Cumulant Analysis in Fluorescence Fluctuation Spectroscopy," *Biophysical Journal* **86**, 3981 (2004).

[86] R. Rigler and E. Elson, editors, *Fluorescence Correlation Spectroscopy*, 1 ed. (Springer, 2001).

[87] J. Widengren, U. Mets, and R. Rigler, "Fluorescence correlation spectroscopy of triplet states in solution: a theoretical and experimental study," *J. Phys. Chem.* **99**, 13368 (1995).

[88] J. Enderlein, I. Gregor, D. Patra, and J. Fitter, "Art and Artefacts of Fluorescence Correlation Spectroscopy," *Current Pharmaceutical Biotechnology* **5**, 155 (2004).

[89] J. Keller, A. Schönle, and S. W. Hell, "Efficient fluorescence inhibition patterns for RESOLFT microscopy," *Optics Express* **15**, 3361 (2007).

[90] J. Ries and P. Schwille, "New concepts for fluorescence correlation spectroscopy on membranes," *Physical Chemistry Chemical Physics* **10**, 3487 (2008).

[91] A. Michelman-Ribeiro, D. Mazza, T. Rosales, T. J. Stasevich, H. Boukari, V. Rishi, C. Vinson, J. R. Knutson, and J. G. McNally, "Direct Measurement of Association and Dissociation Rates of DNA Binding in Live Cells by Fluorescence Correlation Spectroscopy," *Biophysical Journal* **97**, 337 (2009).

[92] A. Björkbom, T. Róg, K. Kaszuba, M. Kurita, S. Yamaguchi, M. Lönnfors, T. K. Nyholm, I. Vattulainen, S. Katsumura, and J. P. Slotte, "Effect of Sphingomyelin Headgroup Size on Molecular Properties and Interactions with Cholesterol," *Biophysical Journal* **99**, 3300 (2010).

[93] S. Chiantia, N. Kahya, J. Ries, and P. Schwille, "Effects of Ceramide on Liquid-Ordered Domains Investigated by Simultaneous AFM and FCS," *Biophysical Journal* **90**, 4500 (2006).

[94] M. London, "Ceramide Selectively Displaces Cholesterol from Ordered Lipid Domains (Rafts): IMPLICATIONS FOR LIPID RAFT STRUCTURE AND FUNCTION," *Journal of Biological Chemistry* **279**, 9997 (2003).

[95] E. G. Bremer, J. Schlessinger, and S. Hakomori, "Ganglioside-Mediated Modulation of Cell Growth. Specific Effects of GM3 on Tyrosine Phosphorylation of the Epidermal Growth Factor Receptor.," *Journal of Biological Chemistry* **261**, 2434 (1986).

[96] N. Kawashima, S. Yoon, K. Itoh, and K. Nakayama, "Tyrosine Kinase Activity of Epidermal Growth Factor Receptor Is Regulated by GM3 Binding Through Carbohydrate to Carbohydrate Interactions," *Journal of Biological Chemistry* **284**, 6147 (2009).

[97] U. Coskun, M. Grzybek, D. Drechsel, and K. Simons, "Regulation of Human EGF Receptor by Lipids," *Proceedings of the National Academy of Sciences* **108**, 9044 (2011).

[98] A. Kusumi, C. Nakada, K. Ritchie, K. Murase, K. Suzuki, H. Murakoshi, R. S. Kasai, J. Kondo, and T. Fujiwara, "PARADIGM SHIFT OF THE PLASMA MEMBRANE CONCEPT FROM THE TWO-DIMENSIONAL CONTINUUM FLUID TO THE PARTITIONED FLUID: High-Speed Single-Molecule Tracking of Membrane Molecules," *Annual Review of Biophysics and Biomolecular Structure* **34**, 351 (2005).

[99] U. Coskun and K. Simons, "Cell Membranes: The Lipid Perspective," *Structure* **19**, 1543 (2011).

[100] B. Hein, K. I. Willig, C. A. Wurm, V. Westphal, S. Jakobs, and S. W. Hell, "Stimulated Emission Depletion Nanoscopy of Living Cells Using SNAP-Tag Fusion Proteins," *Biophysical Journal* **98**, 158 (2010), PMID: 20074516 PMCID: PMC2800968.

[101] S. Chatterjee and S. Mayor, "The GPI-anchor and protein sorting," *Cellular and Molecular Life Sciences* **58**, 1969 (2001).

[102] M. D. Resh, "Palmitoylation of Ligands, Receptors, and Intracellular Signaling Molecules," *Sci. STKE* **2006**, re14 (2006).

[103] I. Levental, D. Lingwood, M. Grzybek, U. Coskun, and K. Simons, "Palmitoylation Regulates Raft Affinity for the Majority of Integral Raft Proteins," *Proceedings of the National Academy of Sciences* **107**, 22050 (2010).

[104] O. Rocks, A. Peyker, M. Kahms, P. J. Verveer, C. Koerner, M. Lumbierres, J. Kuhlmann, H. Waldmann, A. Wittinghofer, and P. I. H. Bastiaens, "An Acylation Cycle Regulates Localization and Activity of Palmitoylated Ras Isoforms," *Science* **307**, 1746 (2005).

[105] I. Levental, M. Grzybek, and K. Simons, "Greasing Their Way: Lipid Modifications Determine Protein Association with Membrane Rafts," *Biochemistry* **49**, 6305 (2010).

[106] K. Simons and W. L. Vaz, "Model Systems, Lipid Rafts, and Cell Membranes1," *Annual Review of Biophysics and Biomolecular Structure* **33**, 269 (2004).

[107] M. J. Saxton, "Single-particle tracking: effects of corrals.," *Biophysical Journal* **69**, 389 (1995), PMID: 8527652 PMCID: PMC1236263.

[108] J. Humpolíčková, E. Gielen, A. Benda, V. Fagulova, J. Vercammen, M. vandeVen, M. Hof, M. Ameloot, and Y. Engelborghs, "Probing Diffusion Laws within Cellular Membranes by Z-Scan Fluorescence Correlation Spectroscopy," *Biophysical Journal* **91**, L23 (2006).

[109] T. Fischer and R. L. C. Vink, "Domain formation in membranes with quenched protein obstacles: Lateral heterogeneity and the connection to universality classes," *The Journal of Chemical Physics* **134**, 055106 (2011).

[110] J. Ehrig, E. P. Petrov, and P. Schwille, "Near-Critical Fluctuations and Cytoskeleton-Assisted Phase Separation Lead to Subdiffusion in Cell Membranes," *Biophysical Journal* **100**, 80 (2011), PMID: 21190659 PMCID: PMC3010007.

[111] T. Baumgart, A. T. Hammond, P. Sengupta, S. T. Hess, D. A. Holowka, B. A. Baird, and W. W. Webb, "Large-Scale Fluid/Fluid Phase Separation of Proteins and Lipids in Giant Plasma Membrane Vesicles," *Proceedings of the National Academy of Sciences* **104**, 3165 (2007).

[112] Q. Ruan, M. A. Cheng, M. Levi, E. Gratton, and W. W. Mantulin, "Spatial-Temporal Studies of Membrane Dynamics: Scanning Fluorescence Correlation Spectroscopy (SFCS)," *Biophysical Journal* **87**, 1260 (2004).

[113] T. Meyer and H. Schindler, "Particle counting by fluorescence correlation spectroscopy. Simultaneous measurement of aggregation and diffusion of molecules in solutions and in membranes," *Biophysical Journal* **54**, 983 (1988).

[114] N. Petersen, "Scanning fluorescence correlation spectroscopy. I. Theory and simulation of aggregation measurements," *Biophysical Journal* **49**, 809 (1986).

[115] M. A. Digman, C. M. Brown, P. Sengupta, P. W. Wiseman, A. R. Horwitz, and E. Gratton, "Measuring Fast Dynamics in Solutions and Cells with a Laser Scanning Microscope," *Biophysical Journal* **89**, 1317 (2005).

[116] J. Ries and P. Schwille, "Studying Slow Membrane Dynamics with Continuous Wave Scanning Fluorescence Correlation Spectroscopy," *Biophysical Journal* **91**, 1915 (2006).

[117] Z. Petrášek and P. Schwille, "Precise Measurement of Diffusion Coefficients using Scanning Fluorescence Correlation Spectroscopy," *Biophysical Journal* **94**, 1437 (2008), PMID: 17933881 PMCID: PMC2212689.

[118] V. Levi, Q. Ruan, K. Kis-Petikova, and E. Gratton, "Scanning FCS, a novel method for three-dimensional particle tracking," *Biochemical Society Transactions* **31**, 997 (2003), PMID: 14505467.

[119] Z. Petrášek, C. Hoege, A. Mashaghi, T. Ohrt, A. A. Hyman, and P. Schwille, "Characterization of Protein Dynamics in Asymmetric Cell Division by Scanning Fluorescence Correlation Spectroscopy," *Biophysical Journal* **95**, 5476 (2008).

[120] M. A. Digman and E. Gratton, "Imaging Barriers to Diffusion by Pair Correlation Functions," *Biophysical Journal* **97**, 665 (2009).

[121] Z. Petrášek and P. Schwille, "Photobleaching in Two-Photon Scanning Fluorescence Correlation Spectroscopy," *ChemPhysChem* **9**, 147 (2007).

[122] J. Ries, S. R. Yu, M. Burkhardt, M. Brand, and P. Schwille, "Modular scanning FCS quantifies receptor-ligand interactions in living multicellular organisms," *Nature Methods* **6**, 643 (2009).

[123] M. A. Digman, P. Sengupta, P. W. Wiseman, C. M. Brown, A. R. Horwitz, and E. Gratton, "Fluctuation Correlation Spectroscopy with a Laser-Scanning Microscope: Exploiting the Hidden Time Structure," *Biophysical Journal* **88**, L33 (2005).

[124] T. Wohland, R. Rigler, and H. Vogel, "The standard deviation in fluorescence correlation spectroscopy.," *Biophysical Journal* **80**, 2987 (2001), PMID: 11371471 PMCID: PMC1301482.

[125] M. Schwarzenbacher, M. Kaltenbrunner, M. Brameshuber, C. Hesch, W. Paster, J. Weghuber, B. Heise, A. Sonnleitner, H. Stockinger, and G. J. Schütz, "Micropatterning for quantitative analysis of protein-protein interactions in living cells," *Nature Methods* **5**, 1053 (2008).